Spin Orbit Torque in Ferromagnetic Semiconductors

Dissertation by

Hang Li

In Partial Fulfillment of the Requirements

For the Degree of

Doctor of Philosophy

King Abdullah University of Science and Technology, Thuwal,

Kingdom of Saudi Arabia

The dissertation of Hang Li is approved by the examination committee.

Committee Chairperson: Aurelien Manchon

Committee Member: Udo Schwingenschlogl

Committee Member: Xiaohang Li

Committee Member: Rembert A. Duine

ABSTRACT

Spin Orbit Torque in Ferromagnetic Semiconductors

Hang Li

Electrons not only have charges but also have spin. By utilizing the electron spin, the energy consumption of electronic devices can be reduced, their size can be scaled down and the efficiency of 'read' and 'write' in memory devices can be significantly improved. Hence, the manipulation of electron spin in electronic devices becomes more and more appealing for the advancement of microelectronics. In spin-based devices, the manipulation of ferromagnetic order parameter using electrical currents is a very useful means for current-driven operation. Nowadays, most of magnetic memory devices are based on the so-called spin transfer torque, which stems from the spin angular momentum transfer between a spin-polarized current and the magnetic order parameter. Recently, a novel spin torque effect, exploiting spin-orbit coupling in non-centrosymmetric magnets, has attracted a massive amount of attention. This thesis addresses the nature of spin-orbit coupled transport and torques in non-centrosymmetric magnetic semiconductors.

We start with the theoretical study of spin orbit torque in three dimensional ferromagnetic GaMnAs. Using the Kubo formula, we calculate both the current-driven field-like torque and anti-damping-like torque. We compare the numerical results with the analytical expressions in the model case of a magnetic Rashba two-

dimensional electron gas. Parametric dependencies of the different torque components and similarities to the analytical results of the Rashba two-dimensional electron gas in the weak disorder limit are described.

Subsequently we study spin-orbit torques in two dimensional hexagonal crystals such as graphene, silicene, germanene and stanene. In the presence of staggered potential and exchange field, the valley degeneracy can be lifted and we obtain a valley-dependent Berry curvature, leading to a tunable antidamping torque by controlling the valley degree of freedom.

This thesis then addresses the influence of the quantum spin Hall effect on spin orbit torque in nanoribbons with a hexagonal lattice. We find a dramatic modification of the nature of the torque (field-like and damping-like component) when crossing the topological phase transition. The relative magnitude of the two torque components can be significantly modifies by changing the magnetization direction.

Finally, motivated by recent experimental results, we conclude by investigating the features of spin-orbit torque in magnetic transition metal dichalcogenides. We find the torque is associated with the valley polarization. By changing the magnetization direction, the torque can be changed from a finite value to zero when the valley polarization decreases from a finite value to zero.

ACKNOWLEDGEMENTS

First of all, I would like to thank to my Ph.D supervisor, Prof. Aurelien Manchon, who has provided me an opportunity to work with him in the physics field. He has sharp intuition, insightful thinking and encyclopedic knowledges. He will usually be a role model to me: a great supervisor and true physicist. Thanks for inspiring me, guiding me, sharing his experience with me and caring for me throughout all these years at KAUST. Without his enthusiastic support and encouragement, my knowledges and interest in physics can be not broadened. I also would like to thank Dr. Xuhui Wang, for his invaluable collaborations and suggestions. Without his help, most of papers can not be accepted smoothly. I am grateful to Dr. Fatih Dogan for his help and support at the beginning of my scientific research. I would also like to thank Prof. Tomas Jungwirth, Prof. Jario Sinova, Dr. Karel Vyborny and Dr. Huawei Gao, for their invaluable collaborations and helpful suggestions. Special thanks should be given to my current and former group members: Hamed Ben Mohamed Saidaoui, PapaBirame Ndiaye, Collins Akosa,Christian OrtizPauyac and Yahua Yuan. I would like to take this chance to thank the support from King Abdullah. Finally, I would like to thank my parents for their love and support.

TABLE OF CONTENTS

Copyright **1**

Abstract **3**

Acknowledgements **5**

1 Introduction **9**

1.1 Spintronics 9

1.1.1 Overview 9

1.1.2 Diluted magnetic semiconductor for spintronics 10

1.1.3 Spin injection in semiconductors 12

1.1.4 Graphene for spintronics 14

1.1.5 Spin-based devices 17

1.2 Spin transfer torque 19

1.2.1 Principle of spin transfer torque 19

1.2.2 Spin transfer torque in diluted magnetic semiconductor 20

1.2.3 Spin transfer torque in graphene 22

1.3 Spin orbit torques 25

1.3.1 Spin orbit coupling 25

1.3.2 Principle of spin orbit torque 27

1.3.3 Spin orbit torque in diluted magnetic semiconductor 28

1.3.4 Search for Spin orbit torque in graphene 29

1.4 Objectives and Contributions 30

2 Theoretical Background **32**

2.1 k · p theory for bulk GaAs 32

2.2 The tight-binding Hamiltonian for 2D graphene in the momentum space 35

2.3 Tight-binding model for graphene nanoribbons in a super-unit cell . . 39

2.3.1 Armchair nanoribbons 40

2.3.2 zigzag nanoribbons 43

2.4 Kubo formula 46
2.5 Lattice Green's function method in graphene nanoribbons 49
2.5.1 Spin denstiy in graphene nanoribbons 53

3 Microscopic Description of Spin Orbit Torque in Diluted Magnetic Semiconductors 55
3.1 Extrinsic spin orbit torque 56
3.2 Interband versus intraband transitions 65
3.2.1 Intraband and Interband Contributions in Kubo formula . . . 67
3.2.2 Two-dimensional Rashba ferromagnet 71
3.2.3 Dilute Magnetic Semiconductors 74
3.2.4 Numerical Results 77

4 Valley-Dependent Spin-Orbit Torques in Two Dimensional Graphene-Like Materials 85
4.1 Introduction 85
4.2 Model and Method 87
4.3 Inverse spin Galvanic effect 91
4.3.1 Non-magnetic honeycomb lattice 91
4.3.2 Magnetic honeycomb lattice 94
4.4 Valley-Dependent Spin-Orbit Torque 95
4.4.1 Staggered Potential 96
4.4.2 Angular dependence 96
4.5 Connection Between Spin-Orbit Torque and Berry curvature 98
4.6 Discussion 101
4.7 Conclusion 103

5 Spin Orbit Torque in One-Dimensional Graphene Nanoribbons 104
5.1 Introduction 104
5.2 Spin-orbit torque and charge pumping 106
5.3 Model and method 108

5.4 Spin-orbit torques 112
5.5 Charge pumping 115
5.6 Discussion and conclusion 116

6 Spin Orbit Torque in Two-Dimensional MoS_2 118
6.1 introduction 118
6.2 Model and Method 119
6.3 Results 121

7 Concluding Remarks 126

References 129

Chapter 1

Introduction

1.1 Spintronics

1.1.1 Overview

In the past century, the progress of technology has been largely relying on the development of electronic devices. These devices offer the ability to control the charge flows on microscopic scales, thereby enabling functions essential to practical applications in the storage of information [1]. Up till now, most electronic devices rely on the electrical manipulation of the charge of the carriers (electrons or holes). However, apart from their charges, electrons also possess an intrinsic spin angular momentum. Recently, intensive efforts have been devoted to explore the possibility of controlling electrons via their spins. Many achievements have been made along this line and have resulted in the opening of a new field, i.e., spin based electronics or spintronics [2].

A significant achievement in the field of spintronics was the discovery of giant magnetoresistance (GMR) effect by Fert and Grünberg as seen in Fig. 1.1 (a) and (b) [3, 4]. They reported that the electrical resistance of a (Fe/Cr) magnetic multilayer depends on the relative orientation of the magnetizations of the Fe layers. The overall resistance of the stack is low (high) when the magnetizations of the adjacent ferromagnetic layers are parallel (antiparallel) to each other as seen in Fig. 1.1 (c)

and (d). This is referred to as GMR effect. On the basis of GMR effect, commercially available field sensors appeared as early as 1995, and IBM produced a hard-drive read head in 1997 [5, 6]. These applications are estimated to impact a multibillion dollar industry. Due to its practical applications, the manipulation of the electron spin in a system composed of metallic materials has attracted considerable attention.

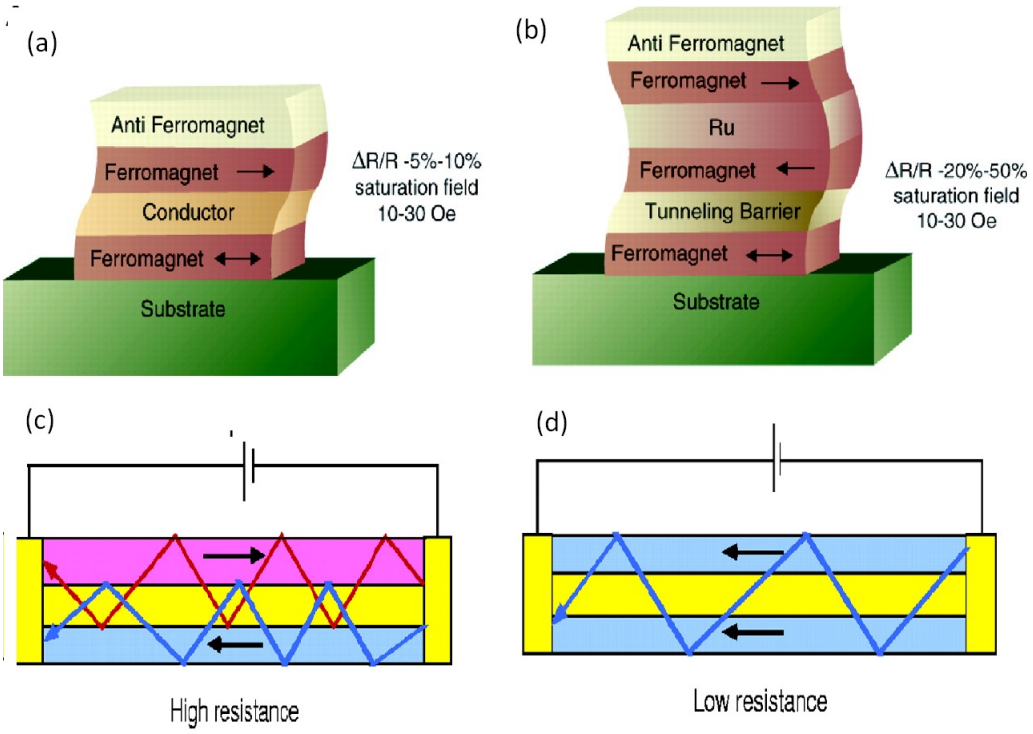

Figure 1.1: GMR-based (a) spin valve and (b) magnetic tunnel junction [6]. Schematic representations of GMR principle for antialigned (high resistance) and aligned (low resistance) [7].

1.1.2 Diluted magnetic semiconductor for spintronics

In the early 90's, study of the manipulation of the electron spin was generalized to the semiconducting materials. Compared with the metallic materials, semiconductors possess a longer spin-coherence time at room-temperature and the ability for optical detection of spin orientation using circularly polarized light, the maturity of the fabrication processes as well as their compatibility with traditional semiconductor mi-

croelectronics [8]. To achieve this goal, the spintronics community has been intended to develop materials displaying both semiconducting and magnetic properties. One approach is to incorporate a few percents of transition metal elements into semiconductors. As a result, some of them display magnetism while preserving their semiconducting nature. These semiconducting systems are referred to as *diluted magnetic semiconductors* (DMS). They include oxide-based (such as (Zn,Mn)O) *II-VI* (such as (Zn, Mn)Se), *IV* (such as (Ge,Mn)) and *III-V* groups (such as (Ga,Mn)As) [9]. We limit our description to the most archetypal and widest used DMS, (Ga,Mn)As. Ferromagnetic (Ga,Mn)As thin films were first prepared successfully at low temperature by using molecular beam epitaxy in 1996 [10]. In the GaAs lattice structure Mn substitutes into a Ga site and acts as an acceptor as shown in Fig. 1.2, while also providing a localized spin of S=5/2. This local spin couples with the itinerant holes, leading to the so-called *hole-mediated* ferromagnetism of (Ga,Mn)As [9]. Due to the ZnSe crystal structure of GaAs, (Ga,Mn)As displays cubic magnetocrystalline anisotropy that depends on the carrier concentration. There are three crystal directions [(100) or equivalent] as the preferred axes of magnetization (easy axes). The easy axis is rotated by tuning the hole concentration, i.e., the equilibrium magnetization direction changes upon hole concentration modulation. Figure 1.3 shows the anisotropic magnetic field H_{cu} /M as a function of hole concentration p for various spin-splitting B_G [11]. The easy axis changes dramatically with hole concentration p. Hence, it is possible to control the magnetization direction in (Ga,Mn)As by an external field [12, 13, 14]. In addition, upon Mn doping, the GaAs lattice is distorted which results in strains when deposited on the substrate. The type of strain (tensile or compressive) depends on the lattice constant of the substrate. The strain leads to enhanced bulk inversion symmetry breaking resulting in odd-in-k spin-orbit coupling [9]. This odd-in-k spin-orbit coupling (of either Dresselhaus or Rashba type) can be used to manipulation the magnetization direction by a current, using spin-orbit

torques (see section 1.1.3).

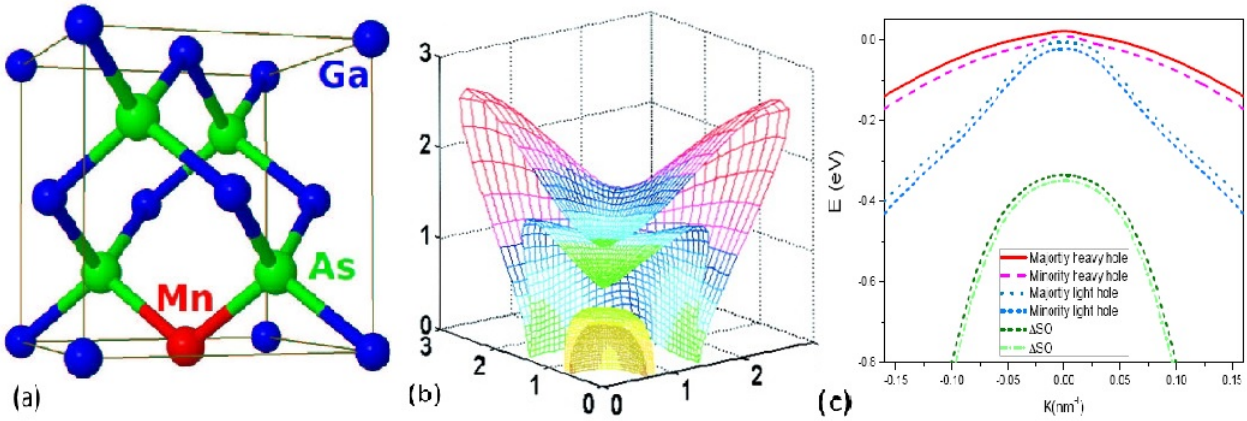

Figure 1.2: (a) Crystal structure (zinc-blende) of GaAs with substitutional Mn impurity [15] and its band structures for 3D [16](b) and 1D (c).

1.1.3 Spin injection in semiconductors

Besides the development of magnetic semiconductors, major efforts have been paid towards the achievement of efficient spin injection from a ferromagnetic metal into a non-magnetic semiconductor [2]. This injection leads to a non-equilibrium population of spin polarized electrons in a nonmagnetic semiconductor. These non-equilibrium spins spread by diffusion and thus can result in a small spin current in the nonmagnetic semiconductor. In the early stage, the measurement of non-equilibrium spin accumulation was focused on systems where both the magnetic and non magnetic layers were metallic. The efficiency of spin injection was estimated to be about 7.5% in $Ni_{0.8}Fe_{0.2}$/Al [17]. Nevertheless, an important limitation of spin transport through metals is their short spin lifetime and related spin diffusion length. The spin lifetime in metal is short (less than 10ps) and spin diffusion length (about 100 nm) is small. In contrast, the spin lifetime and diffusion length in semiconductor such as GaAs is more than 100 ns and 10 μ m at 4.2K due to the weak spin orbit coupling, respectively [18]. Then, spin injection was soon extended to non magnetic semiconductors.

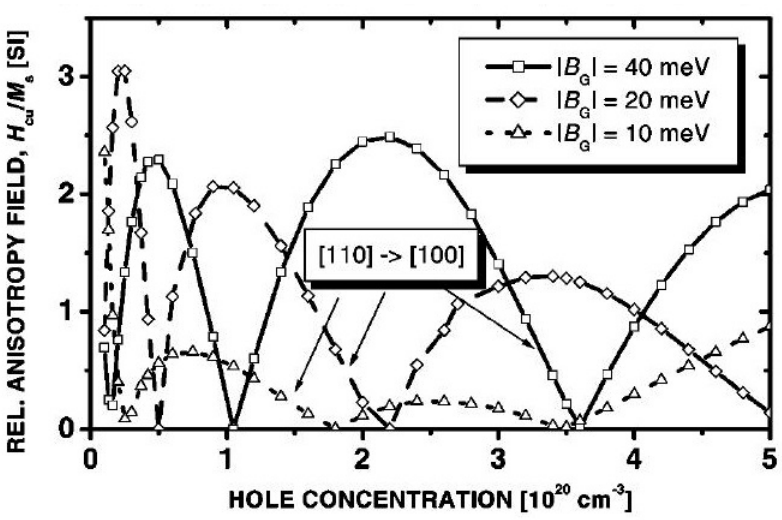

Figure 1.3: Computed minimum magnetic field H_{cu} (divided by M) necessary to align magnetization M along the hard axis for cubic (unstrained) $Ga_{1-x}Mn_xAs$ film. As a function of the hole concentration and the spin-splitting parameter B_G , the easy and hard axes fluctuate alternately between [110] and [100] (or equivalent) directions in the plane of the film. The symbol [110] $\rightarrow$ [100] means that the easy axis is rotated from [110] to [100] with the increasing hole concentration (B_G=-30 meV corresponds to the saturation magnetization of M for $Ga_{0.95}Mn_{0.05}As$) [11].

The efficiency of spin injection in Fe/GaAs ranges from 2% to 8% below room temperature [19]. When using the diluted magnetic semiconductor $Cd_{0.98}Mn_{0.02}Te$ as a spin injector, the efficiency reaches about to 50% [20], while it is estimated as high as 85% in $Be_xMn_yZn_{1-x-y}Se$/GaAs at 10K [21]. Spin injection efficiency of about 25% has been recently reported in graphene at room temperature, using an MgO barrier [22]. Beside the electrical injection, an alternative way to inject spins in non-magnetic materials is photoexcitation. Si is an indirect band-gap semiconductor and expected to have a low efficiency of optical spin injection. Nevertheless, recent work reported a significant progress in achieving robust electrical spin injection into pure Si in a Al/Al_2O_3/CoFe/Si/NiFe/n-Si multilayered structure. The ferromagnetic layer NiFe and CoFe act as a spin filter, leading to the evident enhancement of spin injection efficiency (about 30%) [23].

1.1.4 Graphene for spintronics

Graphene is a promising material for spintronic devices because of its high carrier mobility, weak spin-orbit coupling (SOC), and long spin coherence time [24]. Graphene is a one-atom-thick planar sheet of sp^2 bonded carbon atoms that are densely packed in a honeycomb crystal lattice as shown in Fig. 1.4 (a) [25]. Each unit cell in the graphene lattice contains two carbon atoms and each carbon atom contributes a free electron. Interestingly, in the band structure of graphene the valence and the conduction bands meet at the six corners of the Brillouin zone as shown in Fig. 1.4 (b). In the vicinity of the crossing points (so-called Dirac points), the electron energy presents a linear dependence on the wave vector. Hence, the itinerant electrons behave as a massless chiral (Dirac) fermions. This is in sharp contrast with electrons in metals that are massive particles with parabolic energy dispersion. As a result, compared with the two dimensional electron gas obtained in semiconductor heterostructures, carriers in graphene present spectacular properties, such as a constant carrier velocity, independent of energy, a minimal conductivity, and very low resistive loss due to scattering [26, 27, 28]. The last property makes graphene an excellent candidate for device applications.

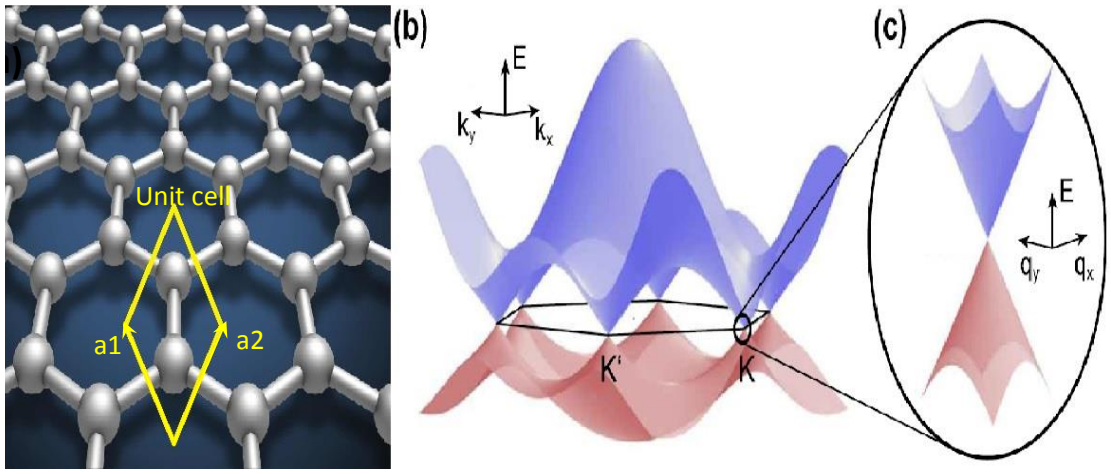

Figure 1.4: (a)Two dimensional graphene and its band structure (b) and (c) from [29] and [30].

By cutting the graphene along a certain direction, graphene nanoribbon (GNR) is obtained. There are two types of graphene nanoribbons according to their terminated edges: armchair and zigzag GNRs as shown in Fig. 1.5. Compared with quantum wires, the electrical properties of the GNRs are more sensitive to the structural geometry and size. For an armchair edged GNR, the band gap depends on the width of the nanowire. When the width N_A satifies $N_A = 3n+2$ (n is the number of carbon atoms), the armchair edged GNR is metallic. Otherwise, it is a semiconductor [31]. As for the zigzag edged GNR, ferromagnetic ground states with the opposite spin directions appear symmetrically at the zigzag edges, leading to its semiconducting behavior [32]. This supplies a new approach to control electron transport by structural design [33].

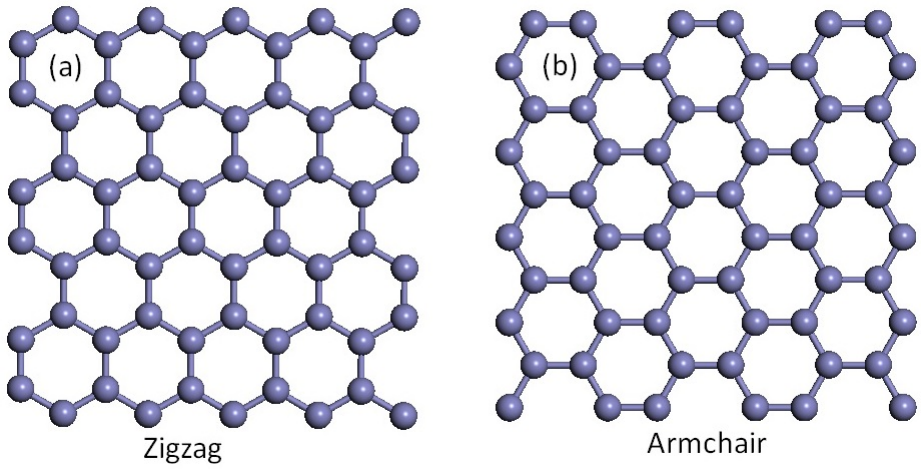

Figure 1.5: Graphene nanoribbons with different edges (a) zigzag and (b) armchair.

The first experiment on spin injection and spin detection in a single-layered graphene was conducted by van Wees *et al.* [34]. They built a nonlocal spin-valve device with four ferromagnetic Co electrodes and injected a current from electrode 3 through the Al_2O_3 barrier into graphene as shown in Fig. 1.6. Figure 1.6 displays a typical measurement of the non-local spin valve device at low temperature 4.2 K. Several resistance values are found which are due to the particular configuration of magnetization directions of four ferromagnetic electrodes demonstrating that carrier

transport between the central electrodes (∼330nm) and the outer electrodes (∼1μm) is spin conserving. Spin coherent transport in a single-layered graphene can be tuned by voltage at the low temperature and can be also found in a spin valve device made of a multilayer graphene [35].

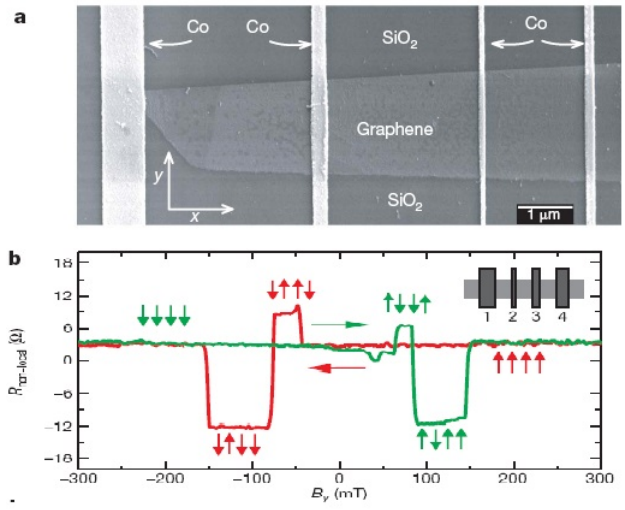

Figure 1.6: Nonlocal spin transport in single layer graphene spin valve done by van Wees *et al.* , from [34]

Recently, a series of new single-layered materials has also been fabricated such as silicene, gemanium and stanene. These materials have a similar hexagonal lattice compared with graphene [36]. Nevertheless, they exhibit more interesting features such as a low buckled structure, which results in a larger intrinsic spin-orbit coupling results in a more evident intrinsic spin orbit coupling. The intrinsic spin orbit coupling may open up a band gap and induce quantum spin Hall effect [37]. In addition, the band gap can be tuned easily by the coupling between substrate and silicene, gemanium or stanene due to a larger intrinsic spin orbit coupling. As a result, it is possible to obtain valley polarization, i.e., currents predominantly carried by one valley. The monolayered silicene sheets have been synthesized on different substrates including Ir(111) and Ag(111). These experiments have triggered many efforts to study the intrinsic properties such as quantum anomalous Hall effect and quantum

valley Hall effect. The study of single-layered materials has also been extended to transition metal dichalcogenides (MoS_2 etc.). For the single-layered MoS_2, the valley polarization is much easier to generate due to the lack of inversion symmetry. Experimental results suggest the MoS_2 is excellent candidate for both valleytronic and optotronic devices [38]. Although several of experiments have been done, the underlying physical mechanisms are still to be explored.

1.1.5 Spin-based devices

With the progress of spintronics, a series of spin-based devices such as spin transistors, magnetic racetrack memory and non-volatile magnetic memories (e.g. MRAM) have been proposed. Compared to the traditional semiconductor devices, the spintronics devices are nonvolatile in nature, and exhibit higher data processing speed, lower electric power consumption and larger integration density. For example, the principle of spin transistor is shown in Fig. 1.7(a), where a normal conducting with strong Rashba spin-orbit coupling is sandwiched by two ferromagnetic layers. A gate voltage is applied on the conducting channel in order to modulate the magnitude of Rashba spin-orbit coupling. When the voltage is absent, the electrons are polarized in the first layer and then pass through the second layer and the drain layer with the same spin directions. While the voltage is present, the electrons precess due to the Rashba spin orbit coupling and pass through the other terminal with the different spin directions. In Fig. 1.7(b), we display a U-shaped spin device, named racetrack memory. In a magnetic nanowire, trains of alternating magnetic domains encode the information. If the spin current is injected to the nanowire, the whole magnetic pattern moves toward the read heads. Then the data can be detected or rewritten. In Fig. 1.7(c), the principle of MRAM is shown. For the binary information '0' the magnetization of the free layer is aligned with the magnetization of the fixed layer and the resistance of the MRAM cell is low. Otherwise, when the magnetization of the free layer is

anti aligned with the magnetization of the fixed layer, the resistance of the MRAM cell is high and record the binary information '1'. By measuring or modifying the resistance of the memory cell, the stored information can be read or written. Finally, the MRAM based on spin orbit torque is shown in Fig. 1.7(d). The readout of the free layer is achieved through a magnetic tunnel junction, but the spin injector is replaced by a non-magnetic heavy metal. When the current is injected into the nonmagnetic heavy metal layer, a large spin torque induced by the spin orbit coupling will exert a force on the free ferromagnetic layer. The magnetic state of this layer is simply detected through a standard magnetic tunnel junction. Compared with the spin transfer torque MRAMs, the energy consumption is lower due to a lower critical current and voltage and write speed is faster. Moreover, the write and read current loops are decoupled and thus separated optimization for read or write is allowed.

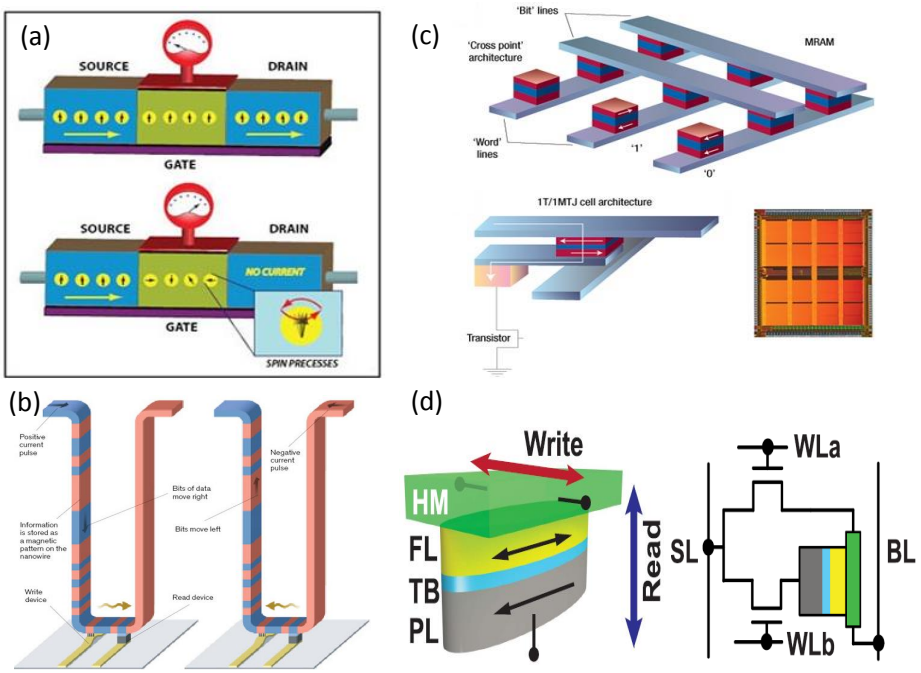

Figure 1.7: (a)Datta-Das spin transistor [39].(b) MRAM [40]. (c) Race track memory [41].(d) Spin orbit torque-MRAMS [42].

1.2 Spin transfer torque

1.2.1 Principle of spin transfer torque

For memory applications, the magnetization of the free layer needs to be manipulated using an external force. It might be switched either by an external magnetic field or by an electrical current flowing through the memory cell [43]. This latter effect, predicted in 1996 and called the *spin transfer torque*, has attracted significant attention for the past two decades and enables the development of electrically controlled magnetic random access memories [44]. A typical magnetic structure, used to study the effect of spin transfer torque, is the *spin valve* (Figure 1.8). In this particular system, the two ferromagnets (Co) possess two different thicknesses so that one is more rigid against magnetic field than the other. The rigid layer is used as a reference (named after the fixed layer) while the other layer, that can be easily manipulated with an external magnetic field, is called the free layer [45]. In general, two ferromagnetic layers are non-collinear and separated by a thin nonmagnetic layer (either a metal with long spin diffusion length such as Cu or Al, or a tunnel barrier, such as MgO or AlO_x). Indeed, when spin-polarized electrons pass through a spin valve, the electrons become spin-polarized in the reference magnetic layer: the reference ferromagnetic layer exerts a torque on the itinerant spin that align these spin on the local magnetization. Inversely, these itinerant electrons exert a torque back on the adjacent ferromagnetic layer due to the transfer of spin angular momentum. This is the principle of spin transfer torque in magnetic spin-valves [46]. With a current exceeding a certain critical value, the magnetization of the free layer can be rotated, leading to a current-induced torque. The torque possesses two components, $\boldsymbol{T} = \boldsymbol{m} \times (\boldsymbol{p} \times \boldsymbol{m}) + \boldsymbol{m} \times \boldsymbol{p}$, the first is antidamping component and the latter is field-like component. The antidamping torque compensates the damping and can induce switching and precession. The critical current is therefore $j_c = H_k/a\alpha$, where a is the torque efficiency, H_k is the

magnetic anisotropy field and α is the damping factor.

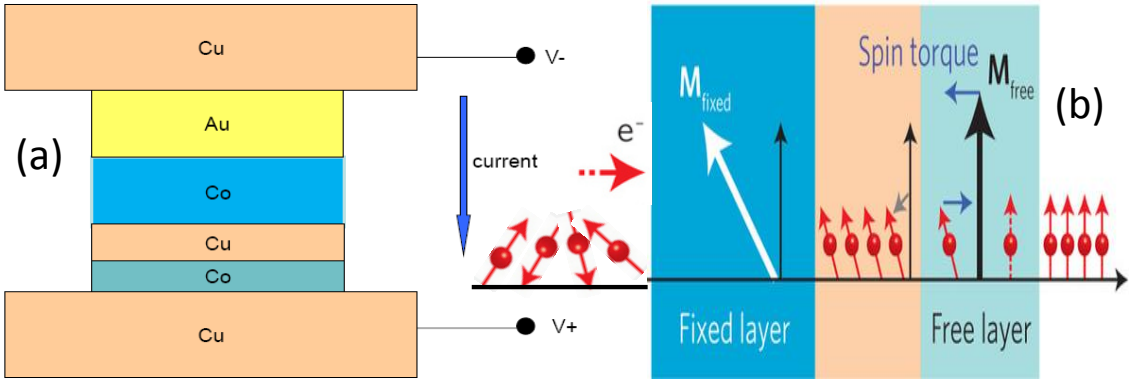

Figure 1.8: (a) Schematic picture of a magnetic multilayered structure in which spin transfer torque is studied experimentally. (b) Principle of spin transfer torque [45].

A typical magnetic multilayered structure used for spin transfer torque studies is shown in Fig. 1.9. The small size of the cross section of the structure (about $60 \times 130nm^2$) is expected to reduce the influence of Oersted field induced by the flowing charge current. The resistance of the structure is plotted as a function of the injected current in Fig. 1.9. As mentioned above, the resistance is high (low) when the magnetizations of the ferromagnetic layers are parallel (anti-parallel) because of the GMR effect. Sudden jumps of the magnetization induced by spin transfer torque can be found in Fig. 1.9, which form a hysteresis loop [47].

1.2.2 Spin transfer torque in diluted magnetic semiconductor

Spin transfer torque can be generated not only in metallic systems (such as transition metals Co, Fe and their compounds) but also in semiconductors. Recently, current-driven magnetization reversal has been studied experimentally in a (Ga,Mn)As/GaAs/(Ga,Mn)As tunneling junction as shown in the upper panel in Fig. 1.10 [48]. In the lower panel, we display the current dependence of the resistance difference between the parallel and the antiparallel magnetization configuration at 30K. The two ferromagnetic layers are parallel in initial configuration, which corresponds to a low resistance

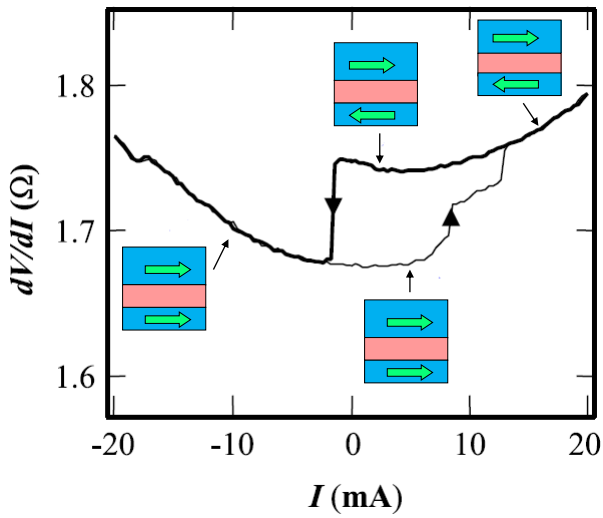

Figure 1.9: The hysteresis curve of differential resistance in a spin valve [47].

(closed circles). The sharp magnetization jump indicates current-driven magnetization switching by the spin transfer torque. However, the critical current density ($10^5 A\ cm^2$) for magnetization switching is two to three orders of magnitude less than in metallic systems due to the weaker saturation magnetization in (Ga,Mn)As. When replacing the nonmagnetic GaAs layer with an InGaAs layer, the minimum resistance of this structure decreases dramatically because the band gap of InGaAs is smaller than that of GaAs [49].

In a (Ga,Mn)As multilayered structure, the intrinsic spin orbit coupling has been emphasized. Due to the presence of spin orbit coupling, the total spin is not conserved and degenerate bands are further split. When the current flows from the first ferromagnetic layer to the other one, the persistent spin transfer torque arises because the spin-orbit field misalign the incoming spin further away from the local magnetization, which provides a bulk contribution to the torque. Furthermore, the spin transfer torque oscillates when increasing the thickness of the polarizing ferromagnetic layer due to the variations of transmission channels related to the total angular momentum and wave vectors caused by the intrinsic spin orbit coupling [50].

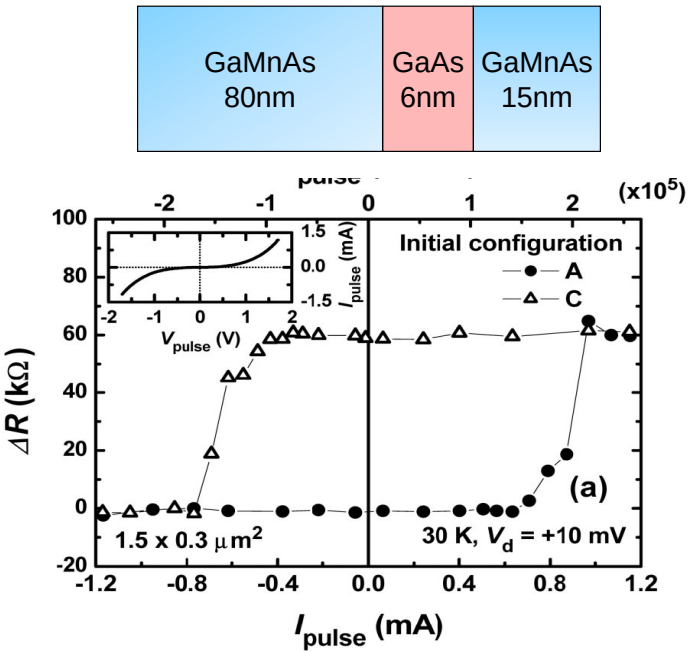

Figure 1.10: The hysteresis curve of differential resistance in a semiconducting tunneling magnetoresistance device [49].

1.2.3 Spin transfer torque in graphene

Recently, spin transfer torque was also reported experimentally in a graphene-based spin valve structure as shown in Fig. 1.11(a) and (b) [51]. The current was injected from Py electrode through the Al_2O_3 barrier into graphene. The effect of magnetization reversal induced by spin transfer torque is shown in Fig. 9(c) in the presence of an external magnetic field along the easy axis. When a current pulse with duration of 5 s is applied to the region between contact 1 and 2, the electrons are spin polarized in the ferromagnetic injector, antiparallel to the magnetization of detector. Then the electrons transfer the angular momentum to the detector and switch its magnetization to the opposite direction as seen in Fig. 1.11(c) and (d) [52].

In addition, a large magnetoresistance effect was observed experimentally in a single graphene layer connected to two Ti electrodes as shown in Fig. 1.12(a) [35]. In Fig. 1.12(b), the current is plotted as a function of voltage near the charge neutrality point at different magnetic fields. The I−V curves possess nonlinear behavior near

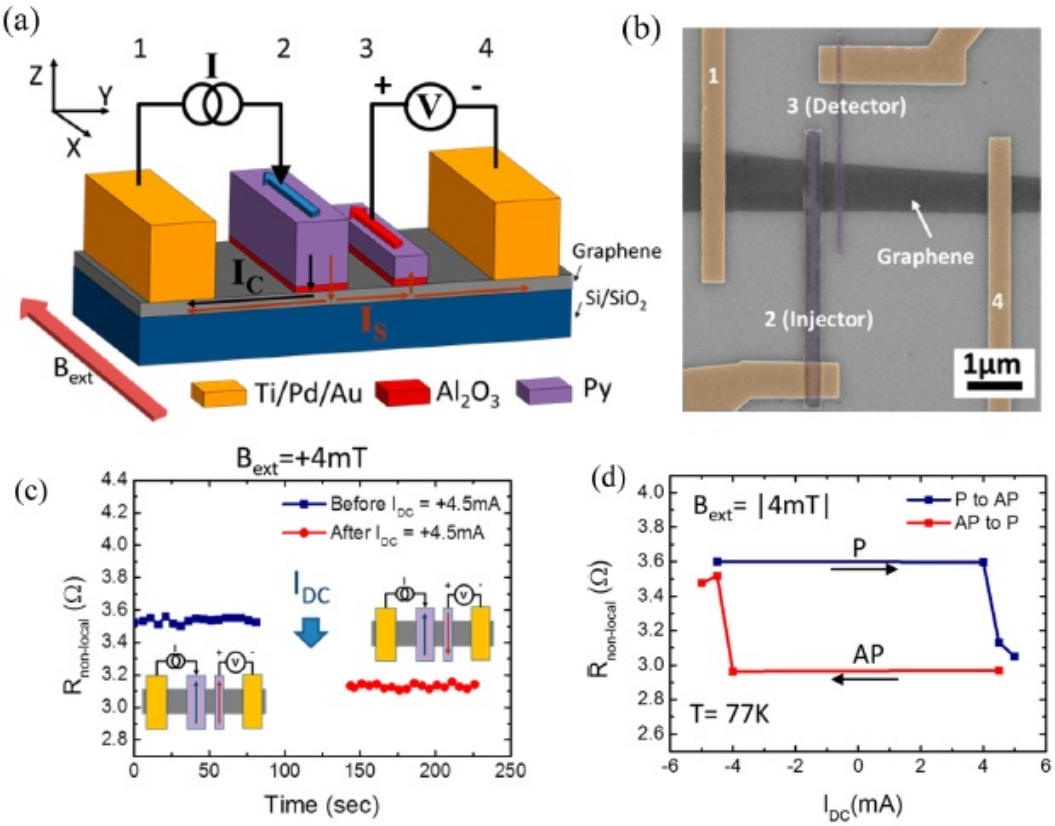

Figure 1.11: (a) Schematic of a lateral nonlocal spin valve structures based on graphene. (b) scanning electron micrograph of a graphene spin valve device (c) the measurement of spin transfer torque in the parallel magnetization configuration (d) Reversible magnetization switching as a function of the injected current [51].

to the zero source−drain bias. There is a semiconductor−like nonlinearly variable gap and the source−drain gap decreases from 25 meV at 0 T to 4.3 meV at 8 T (Fig. 1.12c, inset). Furthermore, the source−drain conduction gap decreases further at a weak gate voltage. A similar magnetoresistance effect has been also studied theoretically in a few graphene layers sandwiched two semi−infinite Ni(111) electrodes [53]. The current−induced spin transfer torque can be generated in a structure with two ferromagnetic leads connected to a normal graphene nanoribbon. The torque dependence on the relative angle between the magnetic moments of the two leads is tuned by a bias voltage [54]. Nevertheless, there is a large conductance mismatch between the ferromagnetic leads and the graphene sheet. The spin transfer torque

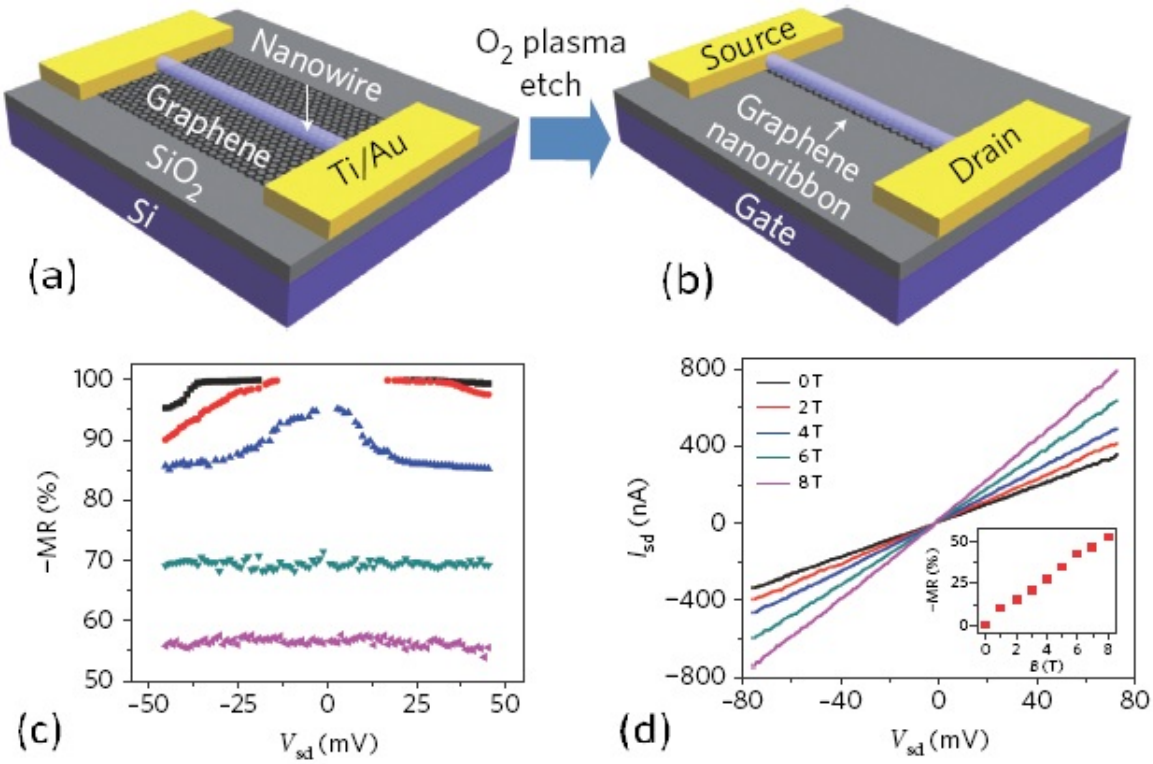

Figure 1.12: (a) Schematic preparation of the graphene nanoribbon-based Field effect transistor. Nanowire is used to as a physical etching mask. Impact of (b) temperature and (c) magnetic field on currentvoltage characteristics when the device is gated at V=3 V [35].

has also been proposed theoretically using a graphene sheet that is connected to two ferromagnetic graphene leads [55]. A ferromagnetic graphene lead can be achieved by depositing a ferromagnetic insulator layer, such as EuO, on the top of graphene. Then the spin-up and spin-down electrons experience different potentials when they travel around the Eu ion, and the difference leads to a spin splitting. The magnitude of tunneling magnetoresistance decreases with the increase of the exchange splitting in graphene. The torque depends on the angle between the magnetic moments of the two leads and can be tuned by the bias voltage.

1.3 Spin orbit torques

In this section, we introduce an alternative mechanism that allows to electrically manipulate the magnetization direction of single ferromagnetic layers without the need for a spin-polarized. This effect, called *spin-orbit torque*, arises in materials possessing strong spin-orbit coupling and either bulk or structural inversion asymmetry.

1.3.1 Spin orbit coupling

Spin orbit coupling is a relativistic effect: When an electron moves in an electric field, this electric field generates a magnetic field in the rest frame of the electron. The magnetic field couples to the spin of the moving electron, resulting in the interplay between electron spin and electric field. The general form of the spin-orbit coupling reads

$$\hat{H}_{so} = \frac{\hbar}{4m_0^2c^2}\hat{\boldsymbol{p}} \cdot (\hat{\boldsymbol{\sigma}} \times \boldsymbol{\nabla} V), \tag{1.1}$$

where m_0 is the mass of electron, c is the light velocity, $\hat{\boldsymbol{\sigma}}$ is the vector of Pauli spin matrices, and V is the electrical potential. The magnitudes and the directions of the effective magnetic field rely on the velocity and travel direction of the electron in a material, i.e., spin orbit coupling gives rise to a **k**-dependent effective magnetic field, where **k** is the wave vector of the electron [36]. In systems lacking inversion symmetry and preserving time-reversal symmetry, the spin-orbit field becomes odd in **k** due to Kramers degeneracy. Two important examples of such odd-in-k spin-orbit coupling are the so-called Rashba and Dresselhaus spin-orbit coupling [56, 57, 58]. The former exists in bulk wurtzite crystals or multilayer structures without interfacial inversion symmetry [56] while the latter arises from strain in Zinc-Blende crystals such as GaAs [59]. This requires that the conduction or valence band edge of the crystals possess an inversion asymmetry. Spin-orbit coupling in low dimensional systems with broken

inversion symmetry was first studied by E.I. Rashba in 1984 and then is named after him as Rashba spin orbit coupling [56]. In a quantum well structure, the quantum average electric field is nonzero in the **z** direction perpendicular to the two dimensional electron gas systems. Therefore, $\boldsymbol{\nabla} V \approx -E\mathbf{z}$ and the spin-orbit coupling reads:

$$\hat{H}_{so} = \frac{\alpha}{\hbar}(\hat{\boldsymbol{p}} \times \hat{\boldsymbol{\sigma}})_z, \tag{1.2}$$

An external bias voltage can tune the band profile and modulate the strength of spin orbit coupling. Rashba spin-orbit coupling acts as a k-dependent field about which flowing spins precess. The signature of this effect has been observed in numerous experiments such as Shubnikov-de Haas oscillations in quantum wells [60].

Another type of spin orbit coupling may occur due to bulk inversion asymmetry. Materials with Zinc-Blende structure lack a center of inversion, the spin polarization is also generated similar to Rashba spin coupling. The problem was first proposed by G. Dresselhaus in 1955 [57, 58]. He found that energy states of electrons with the same wavevectors but with different spins are non-degenerate so that there is a odd−in−k spin orbit coupling stemming from bulk inversion asymmetry. The Hamiltonian for cubic Dresselhaus spin orbit coupling is expressed as:

$$\hat{H}_{\mathrm{DSOC}} = \gamma(\hat{\sigma}_x(k_y^2 - k_z^2)k_x + \hat{\sigma}_y(k_z^2 - k_x^2)k_y + \hat{\sigma}_z(k_x^2 - k_y^2)k_z), \tag{1.3}$$

In addition, if stress is applied to the system, e.g. along the (001) direction, $< k_x^2 >=< k_y^2 > \neq < k_z^2 >$, and the cubic Dresselhaus adopts a simpler form known as the linear Dresselhaus spin-orbit coupling:

$$\hat{H}_{\mathrm{DSOC}} = \beta(\hat{\sigma}_x k_x - \hat{\sigma}_y k_y), \tag{1.4}$$

1.3.2 Principle of spin orbit torque

Since the spin-orbit coupling in inversion asymmetric structures is odd in $\mathbf{k}$, it means that it is possible to generate a nonequilibrium spin-orbit field when current flows through the system (i.e., when $< \mathbf{k} > \neq 0$) [61]. This provides an alternative means to manipulate the magnetization of single ferromagnets without the need for a spin polarizer [62]. Consider a ferromagnet accommodating such a spin-orbit coupling. In the absence of current, the spin-orbit coupling only acts on the magnetization at the second order giving rise to the magneto crystalline anisotropy [63]. When current passes through the system, the inversion asymmetric spin-orbit coupling builds up a spin accumulation in a direction defined by the crystalline structure that may not be aligned with the magnetization direction [64]. In other words, an angular momentum transfer occurs between the orbital angular momentum of the itinerant electrons and their spin angular momentum, resulting in a non-equilibrium spin accumulation. This non-equilibrium spin current competes with the local magnetization, leading to a torque. This is the essence of the spin-orbit torque [61, 65, 66].

In the presence of linear Rashba and Dresselhaus spin orbit coupling, the spin orbit torque in a two dimensional electron gas system has an analytic expression as follows:

$$\boldsymbol{T} = J_{\text{ex}}\boldsymbol{m} \times \hat{\boldsymbol{\Omega}} = 2\sigma E \frac{J_{sd} m}{E_f e\hbar^2}[\alpha \cos(\theta - \theta_0) + \beta \sin(\theta + \theta_0)], \tag{1.5}$$

where σ is the conductivity in the absence of spin orbit coupling, J_{ex} is the exchange coupling constant, E_f is the Fermi energy, θ_0 is the angle between the electrical field and x-axis and θ is the angle between the magnetization and x-axis. Notice that both the magnetization and the electric field remain in the plane in this expression. They are rotated in-plane direction. α is the Rashba coupling constant and β is the Dresselhaus coupling constant. Recent theories on the model Rashba system have

shown that the spin-orbit torque adopts the general form [61]

$$\boldsymbol{T} = T_{\parallel}\boldsymbol{M} \times \boldsymbol{y} + T_{\perp}\boldsymbol{M} \times (\boldsymbol{y} \times \boldsymbol{M}), \tag{1.6}$$

. By using a semiclassical method to treat spin torque, the magnetization in a ferromagnetic system is described phenomenologically through the Landau-Lifshitz-Gilbert equation:

$$\frac{d\boldsymbol{M}}{dt} = -\gamma \boldsymbol{M} \times (\boldsymbol{H_{eff}} + \boldsymbol{H_{cd}}) - \frac{\alpha}{M_s}\boldsymbol{M} \times \frac{d\boldsymbol{M}}{dt} \tag{1.7}$$

where α is the Gilbert damping constant, γ represents the gyromagnetic ratio, $\boldsymbol{M}$ is the magnetization of ferromagnet and the spin torque via $\boldsymbol{T} = -\gamma \boldsymbol{M} \times \boldsymbol{H_{cd}}$. The first term is called the field-like torque and acts like a magnetic field along y (direction transverse to both the plane normal and the flowing current direction) and the second one is called the damping like torque since it directly competes with the magnetic damping.

1.3.3 Spin orbit torque in diluted magnetic semiconductor

This spin orbit torque was observed in a strained ferromagnetic (Ga,Mn)As thin film and interpreted as arising from Dresselhaus [59, 67, 68]. In Fig.1.13, the resistance R_{xy} is plotted as a function of magnetization switching angle ϕ_H near to [010] $\rightarrow$ [100] [59]. It is clearly seen from Fig. 1.13 that there is a hysteresis loop formed by R_{xy}. This implies that there is an interaction between the magnetization and spin polarized current, i.e., there exists a spin torque. Furthermore, the torque only requires a single ferromagnetic layer. The spin torque can be driven by a small current as low as 0.5 mA. Apart from the Dresselhaus spin orbit torque, a weaker Rashba spin orbit torque was also observed in a ferromagnetic (Ga,Mn)As thin film [68]. The spin torque can be further enhanced by doping with phosphorus. Previous experimental results first

observed the field-like spin orbit torques (in-plane components).

Recently, a damping-like ($\boldsymbol{M}\times(z\times\boldsymbol{M})$) spin orbit torque, comparable to field-like torque in magnitudes, has been observed in a single ferromagnetic $(Ga, Mn)As$ film with a broken inversion symmetry due to the strain. The origin of this torque is attributed to interband transitions, as will be discussed further in this thesis. When the system lacks Rashba spin orbit coupling, the nonequilibrium spin density is directed along the magnetization direction. When Rashba spin orbit coupling is present, the system acquires an additional noncollinear nonequilibrium spin density due to the Rashba spin orbit coupling. According to the Bloch equation, the interplay of the in-plane effective magnetic field and magnetization leads to small rotations of all spins toward out-of-plane direction, *i.e.*, produces an out-of-plane spin density. This is because the nonequilibrium spin density modifies the eigenenergies of carriers and results in an interband scattering between the states. In other word, the spin density does not rely upon impurity scattering as mentioned above. In the absence of impurities, the spin density can be estimated by [65]

$$\delta\boldsymbol{S_{int}} = \frac{\hbar}{V}\sum_{\boldsymbol{k},a\neq\boldsymbol{b}}\frac{Im[\langle\psi_{a\boldsymbol{k}}|\hat{\boldsymbol{s}}|\psi_{b\boldsymbol{k}}\rangle\langle\psi_{b\boldsymbol{k}}|e\boldsymbol{E}_x\cdot\hat{\boldsymbol{v}}|\psi_{a\boldsymbol{k}}\rangle]}{(E_{k,a}-E_{k,b})^2}\times(f_{\boldsymbol{k}a}-f_{\boldsymbol{k}b}). \tag{1.8}$$

The integral is over the Fermi sea. This term is associated with the Berry curvature in mixed spin-momentum space. Its contribution to nonequilibrium spin density is still present even without impurity scattering. As a result, it is the intrinsic contribution to the spin density [59, 67, 68].

1.3.4 Search for Spin orbit torque in graphene

Since graphene possesses very large mobility and weak spin relaxation rate, this system - as well as other similar Dirac 2D materials - presents an interesting platform for the realization of spin orbit torque. However, graphene possess weak intrinsic

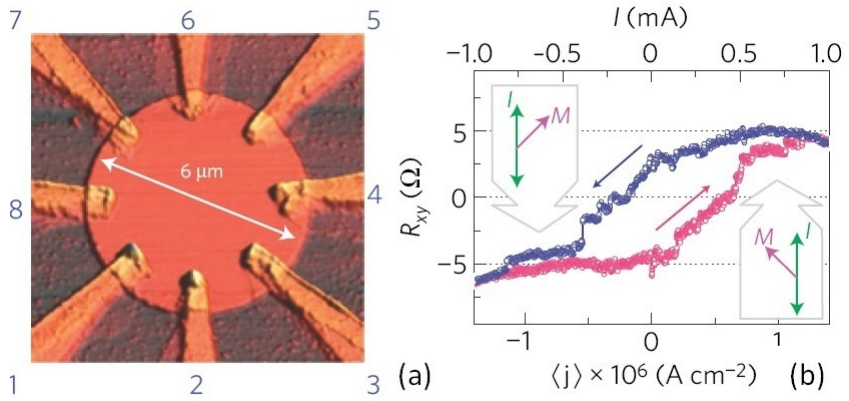

Figure 1.13: (a) Eight leads contact with the island-shaped GaMnAs (b) Resistance of device as a function of magnetization in a (Ga,Mn)As thin film [59].

spin-orbit coupling, as opposed to germanene, silicene and transition metal dichalcogenides. It is therefore important to enhance spin-orbit coupling in graphene to generate spin torque. Recent experiments reported that large Rashba spin splitting in graphene can be induced by Au intercalation at the graphene−Ni interface as shown in Fig. 1.14 [69, 53]. The spin splitting is attributed to the hybridization of Au 5d states. Without the external field, the spin polarization is zero due to the time-reversal symmetry while at a finite electric field a non-equilibrium spin density is generated [32, 70]. As mentioned in section (1.3.3), it is also possible to induce exchange interaction in graphene by depositing a magnetic insulator on the top of it. Therefore, one can foresee that a smart interfacial design of graphene−based devices may render this material suitable for spin-orbit torque experiments. Interestingly, to the best of our knowledge, the impact of DMS and graphene materials on spin-orbit torque has not been addressed in the existing literature.

1.4 Objectives and Contributions

The contributions of this thesis fall in the following streams:

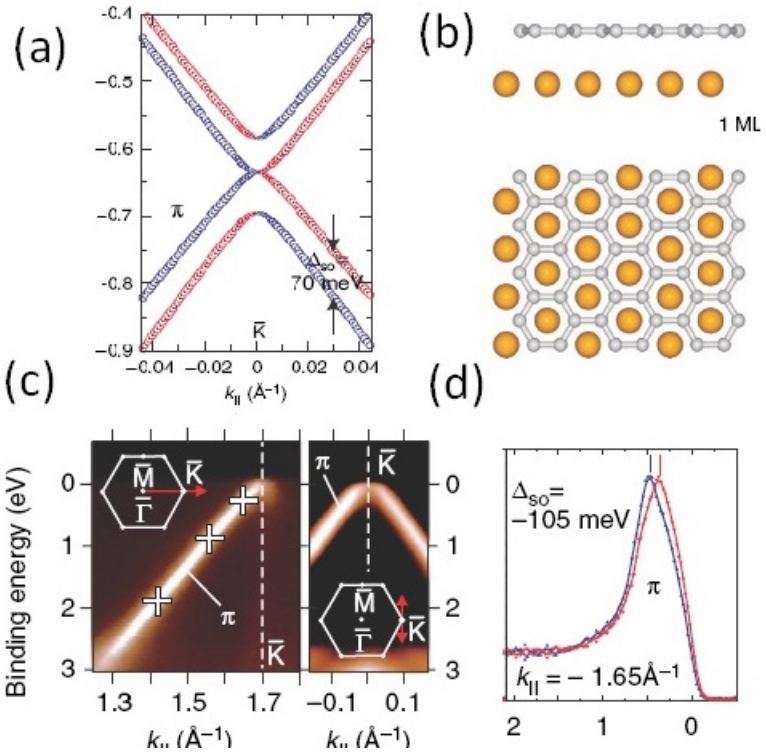

Figure 1.14: The spin orbit splitting (70meV) (a) due to Au atoms moved to the graphene hollow sites (b). (c) Angle−resolved photoemission in the vicinity of the K point of graphene. (d) Rashba spin splitting of graphene in spin and angleresolved photo−emission spectra [69].

• Objective 1: Providing an accurate description of the spin-orbit torque in (Ga,Mn)As, using quantum transport formalism. We are particularly interested in evaluating its connection with the simple Rashba model.

• Objective 2: Exploring the characteristics of spin-orbit torque in graphene−like two dimensional electron gases. The role of intrinsic spin-orbit torque and the impact of valleytronics will be addressed principally.

• Objective 3: Understanding the role of topological chiral edge states on the spin-orbit torque in the quantum spin Hall regime. We will be investigating the electrical efficiency of the torque arising from the bulk and from the edges.

Chapter 2

Theoretical Background

k · p theory is a perturbation theory commonly used in semiconductors to describe the band structure with high precision. It was first proposed by Bardeen and Seitz, and then developed by Kohn and Luttinger. By utilizing the known experimental parameters, such as band gap, split-off energy, carrier effective masses, one can determine extrema of energy at the high symmetry points in the Brillouin zone (for example, Γ point k = 0) and then extrapolate the band structure in the vicinity of k value in terms of perturbation theory. k · p theory can be used to fix the band structure of different types of semiconductors such as diamond, zinc-blende, or wurtzite structures, as well as their nanostructures including quantum wells and nanowires.

2.1 k · p theory for bulk GaAs

We start from the single electron Schrödinger equation in a semiconductor

$$\left(\frac{p^2}{2m_e} + V_0\right)\psi_{nk}(\mathrm{r}) = E_n\psi_{nk}(\mathrm{r}), \tag{2.1}$$

where V_0 denotes the periodic crystal potential because of ions and core electrons or exchange interaction, impurities, etc. Assuming the potential V_0 is periodic, the

wavefunctions are subject to the Bloch theorem,

$$\psi_{\mathrm{nk}}(\mathrm{r}) = e^{i\mathrm{k}\cdot\mathrm{r}} u_{\mathrm{nk}}(\mathrm{r}); u_{\mathrm{nk}}(r) = u_{\mathrm{nk}}(\mathrm{r}+\mathrm{R}).$$

Substituting the Eq.2.2 into the Eq.2.1, we have

$$\left(\frac{p^2}{2m_e} + V_0 + \frac{\hbar^2 k^2}{2m_e} + \frac{\hbar}{m_e} k\cdot p\right) u_{nk}(\mathrm{r}) = E_n u_{nk}(\mathrm{r}). \tag{2.2}$$

This is so-called k · p Hamiltonian. Once E_n and $u_{nk}(\mathrm{r})$ are known, it is easy to treat the k-dependent terms as perturbations in Eq. 2.2.

The Kohn-Luttinger Hamiltonian is an effective Hamiltonian that describes valence bands of the semiconductors with zinc-blende structure such as GaAs. By the degenerate second-order pertubation theory, we can construct the k · p Hamiltonian matrices based on the eigenstates of angular momentum $|X\rangle$, $|Y\rangle$ and $|Z\rangle$ as:

$$\hat{H}_{ij} = \frac{\hbar^2 k^2}{2m_e}\delta_{ij} + \sum_n \frac{\left|\langle i|\ \hat{H}_1\ |j\rangle\right|^2}{E_1 - E_n}, \tag{2.3}$$

where i,j denotes X,Y or Z and $\hat{H}_1$ represents the k · p terms in Eq. 2.2. $|X\rangle$, $|Y\rangle$ and $|Z\rangle$ can be written by the orbital angular momentum eigenstates $|m_l\rangle$ with l=1:

$$\begin{aligned}
|X\rangle =& \frac{1}{\sqrt{2}}(|m_l=-1\rangle - |m_l=1\rangle)\\
|Y\rangle =& \frac{1}{\sqrt{2}}(|m_l=-1\rangle + |m_l=1\rangle)\\
|Z\rangle =& (|m_l=0\rangle).
\end{aligned} \tag{2.4}$$

where we have in the coordinate representation:

$$\begin{aligned}\langle \boldsymbol{r}|m_l=1\rangle =& -\frac{1}{\sqrt{2}}f(r)(x+iy)\\ \langle \boldsymbol{r}|m_l=-1\rangle =& \frac{1}{\sqrt{2}}f(r)(x-iy)\\ \langle \boldsymbol{r}|m_l=-0\rangle =& f(r)z.\end{aligned} \tag{2.5}$$

In the absence of spin orbit coupling, we use the relation:

$$\frac{m_e^2}{\hbar}|\langle X|\ \hat{H}_1\ |m\rangle|^2 = |\langle X|\ \hat{p}_x\ |m\rangle|^2 k_x^2 + |\langle X|\ \hat{p}_y\ |m\rangle|^2 k_y^2 + |\langle X|\ \hat{p}_z\ |m\rangle|^2 k_z^2. \tag{2.6}$$

Finally, the Eq. 2.6 can be rewritten as:

$$\hat{H}_{\rm KL} = \begin{pmatrix} E_1 + Ak_x^2 + B(k_y^2+k_z^2) & Ck_xk_y & Ck_xk_z \\ Ck_xk_y & E_1 + Ak_y^2 + B(k_x^2+k_z^2) & Ck_yk_z \\ Ck_xk_z & Ck_yk_z & E_1 + Ak_z^2 + B(k_x^2+k_y^2) \end{pmatrix}. \tag{2.7}$$

The spin orbit coupling splits the degenerate six states (2(spin) $\times$ 3 (X,Y,Z)) into $|J=3/2>$ and $|J=1/2>$. The *six-band* Kohn-Luttinger Hamiltonian reads,

$$\hat{H}_{\rm KL} = \begin{pmatrix} H_{\rm hh} & -c & -b & 0 & \frac{b}{\sqrt{2}} & c\sqrt{2} \\ -c^* & H_{\rm lh} & 0 & b & -\frac{b^*\sqrt{3}}{\sqrt{2}} & -d \\ -b^* & 0 & H_{\rm lh} & -c & d & -\frac{b\sqrt{3}}{\sqrt{2}} \\ 0 & b^* & -c^* & H_{\rm hh} & -c^*\sqrt{2} & \frac{b^*}{\sqrt{2}} \\ \frac{b^*}{\sqrt{2}} & -\frac{b\sqrt{3}}{\sqrt{2}} & d^* & -c\sqrt{2} & H_{\rm so} & 0 \\ c^*\sqrt{2} & -d^* & -\frac{b^*\sqrt{3}}{\sqrt{2}} & \frac{b}{\sqrt{2}} & 0 & H_{\rm so} \end{pmatrix}. \tag{2.8}$$

The Hamiltonian in Eq. (2.8) comprises subspaces of heavy holes (hh), light holes

(lh), and spin-orbit split bands (so), which are defined as

$$\begin{aligned} H_{\rm hh} =& \frac{\hbar^2}{2m}\left[(\gamma_1+\gamma_2)(k_x^2+k_y^2)+(\gamma_1-2\gamma_2)k_z^2\right], \\ H_{\rm lh} =& \frac{\hbar^2}{2m}\left[(\gamma_1-\gamma_2)(k_x^2+k_y^2)+(\gamma_1+2\gamma_2)k_z^2\right], \\ H_{\rm so} =& \frac{\hbar^2}{2m}\gamma_1(k_x^2+k_y^2+k_z^2)+\Delta_{so}. \end{aligned} \tag{2.9}$$

The other parameters appearing in Eq.(2.8) are defined as

$$\begin{aligned} b =& \frac{\sqrt{3}\hbar^2}{m}\gamma_3 k_z(k_x-ik_y), \\ c =& \frac{\sqrt{3}\hbar^2}{2m}\left[\gamma_2(k_x^2-k_y^2)-2i\gamma_3 k_x k_y\right], \\ d =& -\frac{\sqrt{2}\hbar^2}{2m}\gamma_2\left[2k_z^2-(k_x^2+k_y^2)\right], \end{aligned} \tag{2.10}$$

where the phenomenological Luttinger parameters $\gamma_{1,2,3}$ determine the band structures and the effective masses of valence-band holes. Particularly, γ_3 is associated with the anisotropy of energy band structure around the Γ point at $\gamma_2 \neq \gamma_3$. Setting $\gamma_1 = 1.0$ while $\gamma_2 = \gamma_3 = 0$, the six-band Hamiltonian reduces to a simple free-electron model. If $\gamma_2 = \gamma_3 \neq 0$, the Fermi surfaces of both minority and majority hole bands become spherical.

2.2 The tight-binding Hamiltonian for 2D graphene in the momentum space

We define the unit lattice vectors of the hexagonal Bravais lattice as

$$\mathbf{a}_1 = \frac{a}{2}(1,\sqrt{3}), \mathbf{a}_2 = \frac{a}{2}(1,-\sqrt{3}), \tag{2.11}$$

According to the definition of relation between unit lattice vectors and reciprocal lattice vectors $\mathbf{a}_1\mathbf{b}_1 = \mathbf{a}_2\mathbf{b}_2 = 2\pi$ and $\mathbf{a}_1\mathbf{b}_2 = \mathbf{a}_2\mathbf{b}_1 = 0$, their reciprocal lattice vectors are:

$$\mathbf{b}_1 = \frac{2\pi}{a}(1, \frac{1}{\sqrt{3}}), \mathbf{b}_2 = \frac{2\pi}{a}(1, -\frac{1}{\sqrt{3}}). \tag{2.12}$$

For two-dimensional hexagonal crystals, each unit cell contains two carbon atoms. The Hamiltonian is a 2×2 matrix without the particle spin:

$$\hat{H}_{sys} = \begin{pmatrix} H_{\mathrm{AA}} & H_{\mathrm{AB}} \\ H_{\mathrm{BA}} & H_{\mathrm{BB}} \end{pmatrix}, \tag{2.13}$$

where H_{AA} (H_{BB}) describes the intrinsic effect at the sublattice A (B) site in the unit cell and H_{AB} (H_{BA}) represents the coupling between two sublattices. In the presence of particle spin the Hamiltonian is a 4×4 matrix. We employ the Bloch wave functions to describe the electron/spin transport among the different unit cells. It can be written as :

$$\psi_j(\mathbf{k}, r) = \frac{1}{\sqrt{N}} \sum_{i=1}^{N} e^{i\boldsymbol{k}\cdot\boldsymbol{R_{j,i}}} \phi_j(\boldsymbol{r} - \boldsymbol{R_{j,i}}), \tag{2.14}$$

where the sum is over N different unit cells with the index i=1...N, and $\boldsymbol{R_{j,i}}$ denotes the position of the j-th orbital in the i-th unit cell. Once we have the Bloch wave

function, the matrix element in Eq.2.13 may be found as

$$\begin{aligned} H_{AA} &= \frac{1}{N}\sum_{i=1}^{N}\sum_{j=1}^{N} e^{i\boldsymbol{k}\cdot(\boldsymbol{R_{j,A}}-\boldsymbol{R_{i,A}})}\langle\phi_A(\boldsymbol{r}-\boldsymbol{R_{i,A}})|\ H\ |\phi_A(\boldsymbol{r}-\boldsymbol{R_{j,A}})\rangle \\ &\approx \frac{1}{N}\sum_{i=1}^{N}\langle\phi_A(\boldsymbol{r}-\boldsymbol{R_{i,A}})|\ H\ |\phi_A(\boldsymbol{r}-\boldsymbol{R_{i,A}})\rangle \\ &\approx \frac{1}{N}\sum_{i=1}^{N}\epsilon_{2p} \\ &= \epsilon_{2p}. \end{aligned} \tag{2.15}$$

Note that we assume that the dominant contribution in the first line arises from the same site j=i for each unit cell. Each term in the second line is independent of the site index i. Following a similar way, the B sublattice can be obtained:

$$H_{BB} = H_{AA} = \epsilon_{2p}. \tag{2.16}$$

For the off-diagonal parts, each atom has three nearest-neighbor atoms with the index l (l=1,2,3). We only consider the A atom and then have

$$\begin{aligned} H_{AB} &= \frac{1}{N}\sum_{i=1}^{N}\sum_{r=1}^{3} e^{i\boldsymbol{k}\cdot(\boldsymbol{R_{r,B}}-\boldsymbol{R_{i,A}})}\langle\phi_A(\boldsymbol{r}-\boldsymbol{R_{i,A}})|\ H\ |\phi_B(\boldsymbol{r}-\boldsymbol{R_{r,B}})\rangle \\ &\approx \frac{1}{N}\sum_{i=1}^{N}\sum_{r=1}^{3} e^{i\boldsymbol{k}\cdot(\boldsymbol{R_{r,B}}-\boldsymbol{R_{i,A}})}\gamma \\ &= \frac{\gamma}{N}\sum_{i=1}^{N} e^{i\mathrm{k}\cdot\delta_{\mathrm{l}}} \\ &= \gamma f(\mathrm{k}), \end{aligned} \tag{2.17}$$

where the matrix element between neighboring atoms, $\gamma = \langle\phi_A(\boldsymbol{r}-\boldsymbol{R_{i,A}})|\ H\ |\phi_B(\boldsymbol{r}-\boldsymbol{R_{j,B}})\rangle$ is independent of indices i and l. We assume $f(\mathrm{k}) = \sum_{\mathrm{r=1}}^{3} \mathrm{e}^{\mathrm{ik}\cdot(\mathrm{R}_{\boldsymbol{r,B}}-\mathrm{R}_{\boldsymbol{i,A}})} = \sum_{\mathrm{r=1}}^{3} \mathrm{e}^{\mathrm{ik}\cdot\delta_{\mathrm{l}}}$. For A sublattice, three nearest-neighbor vectors in the coordinate system

are respectively given as:

$$\boldsymbol{\delta}_1 = a(0, 1/\sqrt{3}), \boldsymbol{\delta}_2 = a(1/2, -1/2\sqrt{3}), \boldsymbol{\delta}_3 = (-1/2, -1/2\sqrt{3}). \tag{2.18}$$

Then f(k) can be read as:

$$\begin{aligned} f(\mathrm{k}) &= \sum_{r=1}^{3} e^{i\boldsymbol{k}\cdot\delta_l} \\ &= e^{ik_y a/\sqrt{3}} + e^{ik_x a/2} e^{-ik_y a/2\sqrt{3}} + e^{ik_x a/2} e^{-ik_y a/2\sqrt{3}} \\ &= e^{ik_y a/\sqrt{3}} + 2\cos(k_x a/2) e^{-ik_y a/2\sqrt{3}}. \end{aligned} \tag{2.19}$$

H_{BA} is the complex conjugate of H_{AB}:

$$H_{BA} = H_{AB} = \gamma f^*(\mathrm{k}). \tag{2.20}$$

With the help of reciprocal lattice vectors b_1 and b_2, the coordinates of two conjugate $\boldsymbol{K}$ points in the reciprocal space can be found as:

$$\boldsymbol{K}_{\pm} = \pm(4\pi/3a, 0). \tag{2.21}$$

We introduce a momentum $\boldsymbol{p}$ that is measured from the center of the K point,

$$\boldsymbol{p} = \hbar\boldsymbol{k} - \hbar\boldsymbol{K}. \tag{2.22}$$

Then, the coupling between the A and B subblattice is equal to

$$\begin{aligned} f(\mathrm{k}) &= e^{ik_y a/\sqrt{3}} + 2\cos(\pm 2\pi \boldsymbol{K}/3 + k_x a/2) e^{-ik_y a/2\sqrt{3}} \\ &\approx (1 + ik_x a/\sqrt{3}) + 2(1 - ik_y a/2\sqrt{3})(-1/2 - \frac{\pm\sqrt{3}k_x a}{2}) \\ &\approx \sqrt{3}a/2(\pm k_x - ik_y). \end{aligned} \tag{2.23}$$

Table 2.1: Low-energy Hamiltonian

	h_0	h_R	h_{so}	h_z
C	$\mathrm{v}(\tau k_x\hat{\sigma}_x - k_y\hat{\sigma}_y)\otimes\hat{I}$	$\frac{t_R}{2}(\tau\hat{s}_y\otimes\hat{\sigma}_x - \hat{s}_x\otimes\hat{\sigma}_y)$	0	$M\hat{s}_z\otimes\hat{I}$
Si	$\mathrm{v}(\tau k_x\hat{\sigma}_x - k_y\hat{\sigma}_y)\otimes\hat{I}$	$\frac{t_R}{2}(\tau\hat{s}_y\otimes\hat{\sigma}_x - \hat{s}_x\otimes\hat{\sigma}_y)$	$\tau t_{so}\hat{s}_z\otimes\hat{\sigma}_z$	$M\hat{s}_z\otimes\hat{I}$
Ge	$\mathrm{v}(\tau k_x\hat{\sigma}_x - k_y\hat{\sigma}_y)\otimes\hat{I}$	$\frac{t_R}{2}(\tau\hat{s}_y\otimes\hat{\sigma}_x - \hat{s}_x\otimes\hat{\sigma}_y)$	$\tau t_{so}\hat{s}_z\otimes\hat{\sigma}_z$	$M\hat{s}_z\otimes\hat{I}$

Similarly, we can get the other terms in Table 2.1 within the low energy regime on the basis of $\{\phi_{A,\uparrow}, \phi_{B,\downarrow}, \phi_{B,\uparrow}, \phi_{A,\downarrow}\}$. where σ denotes the pseudospin degree of freedom and s is the real spin of particles. $v = \sqrt{3}t/2$, $\tau = \pm 1$ stands for the valley of freedom, $\hat{I}$ is a $2\times$ 2 unity matrix, $t_{so} = 3\sqrt{3}\lambda_{so}$, $t_R = 3\lambda_R/2$.

The 4×4 spin operators are written as:

$$\hat{\boldsymbol{S}}_{x,y,z} = \hat{\boldsymbol{s}}_{x,y,z}\otimes\hat{I} \tag{2.24}$$

2.3 Tight-binding model for graphene nanoribbons in a super-unit cell

Let us start from the time independent Schrödinger's equation:

$$\hat{H}_{op}\psi(\boldsymbol{k},\boldsymbol{r}) = E(\boldsymbol{k})\psi(\boldsymbol{k},\boldsymbol{r}), \tag{2.25}$$

where $\hat{H}_{op}$ is the Hamiltonian operator, $E(\boldsymbol{k})$ and $\psi(\boldsymbol{k},\boldsymbol{r})$ are eigenvalues and eigen-wave-vectors in graphene lattice. $\boldsymbol{k}$ and $\boldsymbol{r}$ denotes the wave-vector and position, respectively. The j-th eigenvalue $E_j(\boldsymbol{k})$ as a function of $\boldsymbol{k}$ is given by

$$E_j(\boldsymbol{k}) = \frac{\langle\psi_j|\hat{H}_{op}|\psi_j\rangle}{\langle\psi_j|\psi_j\rangle} = \frac{\int\psi_j^*\hat{H}_{op}\psi_j d\boldsymbol{r}}{\int\psi_j^*\psi_j d\boldsymbol{r}}. \tag{2.26}$$

Because of the translational symmetry of the carbon atoms in a graphene lattice, the eigenfunctions, $\psi_j(\boldsymbol{k},\boldsymbol{r})(j=1,..,n)$, where n is the number of Bloch wavefunctions can be written as a linear combination of Bloch orbital basis functions $u_m(\boldsymbol{r})$.

$$\psi_j(\boldsymbol{k},\boldsymbol{r}) = \sum_{j'=1}^{n} \phi_{jj'}(\boldsymbol{k}) u_{j'}(\boldsymbol{k},\boldsymbol{r}), \tag{2.27}$$

where $\phi_{jj'}(\boldsymbol{k})$ are coefficients to be determined, and $u_{j'}(\boldsymbol{k},\boldsymbol{r})$ satisfies

$$u_{j'}(\boldsymbol{k},\boldsymbol{r}+\boldsymbol{a}) = u_{j'}(\boldsymbol{k},\boldsymbol{r})(i=1,2). \tag{2.28}$$

Substituting Eq. (2.27) into Eq. (2.26) and changing subscripts we obtain

$$E_j(\boldsymbol{k}) = \frac{\sum_{j,j'}^{n} \phi_{jj}^{*}\phi_{jj'}\langle u_j|\hat{H}_{op}|u_{j'}\rangle}{\sum_{j,j'}^{n} \phi_{jj}^{*}\phi_{jj'}\langle u_j|u_{j'}\rangle} = \frac{\sum_{j,j'}^{n} H_{jj'}(\boldsymbol{k})\phi_{jj}^{*}\phi_{jj'}}{\sum_{j,j'}^{n} S_{jj'}(\boldsymbol{k})\phi_{jj}^{*}\phi_{jj'}}. \tag{2.29}$$

Here the integrals over the Bloch orbitals, $H_{jj'}(\boldsymbol{k})$ and $S_{jj'}(\boldsymbol{k})$ are called the transfer integral matrix and overlap integral matrix, respectively, which are defined by:

$$H_{jj'}(\boldsymbol{k}) = \langle u_j|\hat{H}_{op}|u_{j'}\rangle; S_{jj'}(\boldsymbol{k}) = \langle u_j|u_{j'}\rangle(j,j'=1,...,n). \tag{2.30}$$

$H_{jj'}(\boldsymbol{k})$ and $S_{jj'}(\boldsymbol{k})$ have fixed values, for given value of $\boldsymbol{k}$, and the coefficient ϕ_{jj}^{*} is optimized so as to the minimize $E_i(\boldsymbol{k})$.

2.3.1 Armchair nanoribbons

Consider an armchair graphene nanoribbon with the width N=11 as shown in Fig. 2.1. The wavefunctions can be written as a linear combinations of 2N π orbital functions contributed by the carbon atoms in the unit cell.

$$\psi_j(\boldsymbol{k}_x,\boldsymbol{r}) = \sum_{j'=1}^{2N} \phi_j(\boldsymbol{k}_x) u_j(\boldsymbol{k}_x,\boldsymbol{r}) \tag{2.31}$$

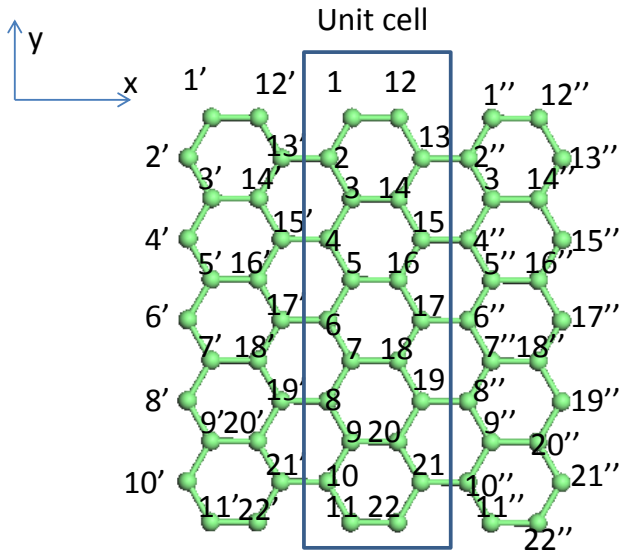

Figure 2.1: Armchair nanoribbon with the width N=11.

$$u_j(\boldsymbol{k}_x, \boldsymbol{r}) = \frac{1}{\sqrt{N}} \sum_{\boldsymbol{r}_j} e^{i\boldsymbol{k}_x \cdot \boldsymbol{r}_j}(\boldsymbol{k}) \upsilon_j(\boldsymbol{r} - \boldsymbol{r}_j)(j = 1, 2, ..., 2N), \tag{2.32}$$

where N is the number of unit cells in the crystal, υ_j is $2p_z$ atomic orbitals and it is assumed to be normalized. Using Eq.(2.30), Eq.(2.31) and Eq.(2.32) the 2N $\times$ 2N elements in the matrix integral H and overlap matrix integral S can be calculated. Here we derive the non-zero elements in the first row $H_{1,1}$, $H_{1,2}$, $H_{1,3}$, $H_{1,6}$, $H_{1,7}$, and $H_{1,8}$, all other non-zero elements can be derived in the same manner.

$$H_{1,1} = \frac{1}{N} \sum_{\boldsymbol{r}_1} \langle \upsilon_1(\boldsymbol{r} - \boldsymbol{r}_1) | H_{op} | \upsilon_1(\boldsymbol{r} - \boldsymbol{r}_1) \rangle = E_{sp}. \tag{2.33}$$

$$\begin{aligned} H_{1,2} &= \frac{1}{N} \sum_{\boldsymbol{r}_1} e^{i\boldsymbol{k}_x \cdot (\boldsymbol{r}_2 - \boldsymbol{r}_1)} \langle \upsilon_1(\boldsymbol{r} - \boldsymbol{r}_1) | H_{op} | \upsilon_1(\boldsymbol{r} - \boldsymbol{r}_2) \rangle \\ &= e^{-ik_x \frac{a_0}{2}} \gamma_0 = a\gamma_0. \end{aligned} \tag{2.34}$$

$$H_{1,3} = \frac{1}{N}\sum_{\boldsymbol{r}_1} e^{i\boldsymbol{k}_x\cdot(\boldsymbol{r}_3-\boldsymbol{r}_1)}\langle \upsilon_1(\boldsymbol{r}-\boldsymbol{r}_1)|H_{op}|\upsilon_1(\boldsymbol{r}-\boldsymbol{r}_3)\rangle = \gamma_1. \tag{2.35}$$

$$\begin{aligned} H_{1,13} &= \frac{1}{N}\sum_{\boldsymbol{r}_1}[e^{i\boldsymbol{k}_x\cdot(\boldsymbol{r}_7-\boldsymbol{r}_1)}\langle \upsilon_1(\boldsymbol{r}-\boldsymbol{r}_1)|H_{op}|\upsilon_1(\boldsymbol{r}-\boldsymbol{r}_7)\rangle + e^{i\boldsymbol{k}_x\cdot(\boldsymbol{r}_{7'}-\boldsymbol{r}_1)}\langle \upsilon_1(\boldsymbol{r}-\boldsymbol{r}_1)|H_{op}|\upsilon_1(\boldsymbol{r}-\boldsymbol{r}_{7'})\rangle] \\ &= (e^{-ik_x\frac{3a_0}{2}} + e^{ik_x\frac{3a_0}{2}})\gamma_1 = 2\cos(\frac{3k_xa_0}{2}) = d\gamma_1. \end{aligned} \tag{2.36}$$

$$\begin{aligned} H_{1,12} &= \frac{1}{N}\sum_{\boldsymbol{r}_1}[e^{i\boldsymbol{k}_x\cdot(\boldsymbol{r}_6-\boldsymbol{r}_1)}\langle \upsilon_1(\boldsymbol{r}-\boldsymbol{r}_1)|H_{op}|\upsilon_1(\boldsymbol{r}-\boldsymbol{r}_6)\rangle + e^{i\boldsymbol{k}_x\cdot(\boldsymbol{r}_{6'}-\boldsymbol{r}_1)}\langle \upsilon_1(\boldsymbol{r}-\boldsymbol{r}_1)|H_{op}|\upsilon_1(\boldsymbol{r}-\boldsymbol{r}_{6'})\rangle] \\ &= e^{ik_xa_0}\gamma_0 + e^{-ik_x2a_0}\gamma_2 = b\gamma_0 + c\gamma_2. \end{aligned} \tag{2.37}$$

We simplify the model and assume that the unit cell contains 10 atoms. The non-zero elements of the 10 × 10 integral matrix H can be written as

$$\hat{H} = \begin{pmatrix} E_{sp} & a\gamma_0 & \gamma_1 & 0 & 0 & b\gamma_0+c^*\gamma_2 & d\gamma_1 & 0 & 0 & 0 \\ a^*\gamma_0 & E_{sp} & a^*\gamma_0 & \gamma_1 & 0 & d\gamma_1 & b^*\gamma_0+c\gamma_2 & d\gamma_1 & 0 & 0 \\ \gamma_1 & a\gamma_0 & E_{sp} & a\gamma_0 & \gamma_1 & 0 & d\gamma_1 & b\gamma_0+c^*\gamma_2 & d\gamma_1 & 0 \\ 0 & \gamma_1 & a^*\gamma_0 & E_{sp} & a^*\gamma_0 & 0 & 0 & d\gamma_1 & b^*\gamma_0+c\gamma_2 & d\gamma_1 \\ 0 & 0 & \gamma_1 & a\gamma_0 & E_{sp} & 0 & 0 & 0 & d\gamma_1 & b\gamma_0+c^*\gamma_2 \\ b^*\gamma_0+c\gamma_2 & d\gamma_1 & 0 & 0 & 0 & E_{sp} & a^*\gamma_0 & \gamma_1 & 0 & 0 \\ d\gamma_1 & b\gamma_0+c^*\gamma_2 & d\gamma_1 & 0 & 0 & a\gamma_0 & E_{sp} & a\gamma_0 & \gamma_1 & 0 \\ 0 & d\gamma_1 & b^*\gamma_0+c\gamma_2 & d\gamma_1 & 0 & \gamma_1 & a^*\gamma_0 & E_{sp} & a^*\gamma_0 & \gamma_1 \\ 0 & 0 & d\gamma_1 & b\gamma_0+c^*\gamma_2 & d\gamma_1 & 0 & \gamma_1 & a\gamma_0 & E_{sp} & a\gamma_0 \\ 0 & 0 & 0 & d\gamma_1 & b^*\gamma_0+c\gamma_2 & 0 & 0 & \gamma_1 & a^*\gamma_0 & E_{sp} \end{pmatrix}. \tag{2.38}$$

The Hamiltonian of Rashba spin orbit coupling in the tight-binding model reads:

$$\hat{H}_R = it_R\sum_{<i,j>} C^+_{i\sigma}\hat{\boldsymbol{z}}\cdot(S_{\sigma\sigma'}\times\boldsymbol{d}_{ij})C_{j\sigma'}. \tag{2.39}$$

When electron spin is considered, each matrix element becomes a 2×2 matrix.

Three types of hopping between the atoms in the unit cell are summarize as:

a) From site 2 to site 1:

$\boldsymbol{d}_{ij} = (1/2, \sqrt{3}/2)$, $i(\boldsymbol{S} \times \boldsymbol{d}_{ij}) = i(\boldsymbol{S}_x\sqrt{3}/2 - 1/2\boldsymbol{S}_y)$ In k-space, the corresponding element should read:

$$H_{2,1} = t_R e^{ik_x \frac{a}{2}} \begin{pmatrix} 0 & -\frac{1}{2} + i\frac{\sqrt{3}}{2} \\ \frac{1}{2} + i\frac{\sqrt{3}}{2} & 0 \end{pmatrix}. \tag{2.40}$$

b) From site 12 to site 1:

$\boldsymbol{d}_{ij} = (-1, 0)$, $i(\boldsymbol{S} \times \boldsymbol{d}_{ij}) = i(0 \times \boldsymbol{S}_x - (-1)\boldsymbol{S}_y)$ In k-space, the corresponding element should read:

$$H_{12,1} = t_R e^{ik_x(-a)} \begin{pmatrix} 0 & 1 \\ -1 & 0 \end{pmatrix}. \tag{2.41}$$

c) From site 3 to site 2:

$\boldsymbol{d}_{ij} = (-1/2, \sqrt{3}/2)$, $i(\boldsymbol{S} \times \boldsymbol{d}_{ij}) = i(\boldsymbol{S}_x\sqrt{3}/2 - (-1/2)\boldsymbol{S}_y)$ In k-space, the corresponding element should read:

$$H_{3,2} = t_R e^{ik_x(-a)} \begin{pmatrix} 0 & \frac{1}{2} + i\frac{\sqrt{3}}{2} \\ -\frac{1}{2} + i\frac{\sqrt{3}}{2} & 0 \end{pmatrix}. \tag{2.42}$$

2.3.2 zigzag nanoribbons

For the zigzag graphene nanoribon with index N shown in Fig. 2.2, H can be obtained using the same method. Here we show the derivation of the non-zero elements in the

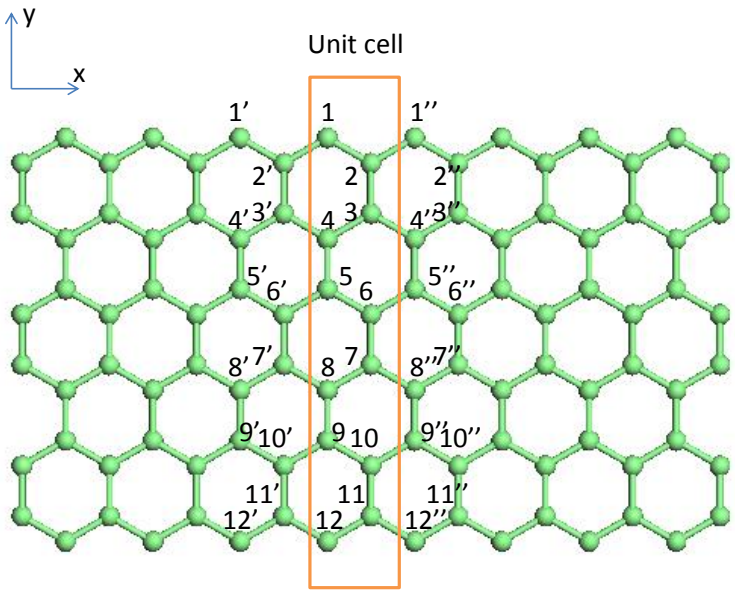

Figure 2.2: Zigzag nanoribbon with the width N=12.

first row $H_{1,1}$,$H_{1,2}$ and $H_{1,3}$.

$$H_{1,1} = \frac{1}{N}\sum_{\boldsymbol{r}_1}[\langle \upsilon_1(\boldsymbol{r}-\boldsymbol{r}_1)|H_{op}|\upsilon_1(\boldsymbol{r}-\boldsymbol{r}_1)\rangle + e^{i\boldsymbol{k}_x\cdot(\boldsymbol{r}_{1'}-\boldsymbol{r}_1)}\langle \upsilon_1(\boldsymbol{r}-\boldsymbol{r}_1)|H_{op}|\upsilon_1(\boldsymbol{r}-\boldsymbol{r}_{1'})\rangle$$
$$+ e^{i\boldsymbol{k}_x\cdot(\boldsymbol{r}_{1''}-\boldsymbol{r}_1)}\langle \upsilon_1(\boldsymbol{r}-\boldsymbol{r}_1)|H_{op}|\upsilon_1(\boldsymbol{r}-\boldsymbol{r}_{1''})\rangle] = E_{sp} + e^{-ik_x\sqrt{3}a_0}\gamma_1 + e^{ik_x\sqrt{3}a_0}\gamma_1$$
$$= E_{sp} + 2\cos(\sqrt{3}k_x a_0)\gamma_1 = E_{sp} + p\gamma_1. \tag{2.43}$$

$$H_{1,2} = \frac{1}{N}\sum_{\boldsymbol{r}_1}[e^{i\boldsymbol{k}_x\cdot(\boldsymbol{r}_{2'}-\boldsymbol{r}_1)}\langle \upsilon_1(\boldsymbol{r}-\boldsymbol{r}_1)|H_{op}|\upsilon_1(\boldsymbol{r}-\boldsymbol{r}_{2'})\rangle$$
$$+ e^{i\boldsymbol{k}_x\cdot(\boldsymbol{r}_2-\boldsymbol{r}_1)}\langle \upsilon_1(\boldsymbol{r}-\boldsymbol{r}_1)|H_{op}|\upsilon_1(\boldsymbol{r}-\boldsymbol{r}_2)\rangle] = e^{-ik_x\frac{\sqrt{3}}{2}a_0}\gamma_0 + e^{ik_x\frac{\sqrt{3}}{2}a_0}\gamma_0$$
$$= 2\cos(\frac{\sqrt{3}}{2}k_x a_0)\gamma_0 = q\gamma_0. \tag{2.44}$$

$$H_{1,3} = \frac{1}{N}\sum_{\boldsymbol{r}_1}[e^{i\boldsymbol{k}_x\cdot(\boldsymbol{r}_{3'}-\boldsymbol{r}_1)}\langle \upsilon_1(\boldsymbol{r}-\boldsymbol{r}_1)|H_{op}|\upsilon_1(\boldsymbol{r}-\boldsymbol{r}_{3'})\rangle$$
$$+ e^{i\boldsymbol{k}_x\cdot(\boldsymbol{r}_3-\boldsymbol{r}_1)}\langle \upsilon_1(\boldsymbol{r}-\boldsymbol{r}_1)|H_{op}|\upsilon_1(\boldsymbol{r}-\boldsymbol{r}_3)\rangle] = e^{-ik_x\frac{\sqrt{3}}{2}a_0}\gamma_1 + e^{ik_x\frac{\sqrt{3}}{2}a_0}\gamma_1$$
$$= 2\cos(\frac{\sqrt{3}}{2}k_x a_0)\gamma_1 = q\gamma_1. \tag{2.45}$$

The 8×8 matrix H is written as

$$\hat{H} = \begin{pmatrix} E_{sp}+p\gamma_1 & q\gamma_0 & q\gamma_1 & 0 & 0 & 0 & 0 & 0 \\ q\gamma_0 & E_{sp}+p\gamma_1 & \gamma_0 & q\gamma_1 & 0 & 0 & 0 & 0 \\ q\gamma_1 & \gamma_0 & E_{sp}+p\gamma_1 & q\gamma_0 & q\gamma_1 & 0 & 0 & 0 \\ 0 & q\gamma_1 & q\gamma_0 & E_{sp}+p\gamma_1 & \gamma_0 & q\gamma_1 & 0 & 0 \\ 0 & 0 & q\gamma_1 & \gamma_0 & E_{sp}+p\gamma_1 & q\gamma_0 & q\gamma_1 & 0 \\ 0 & 0 & 0 & q\gamma_1 & q\gamma_0 & E_{sp}+p\gamma_1 & \gamma_0 & q\gamma_1 \\ 0 & 0 & 0 & 0 & q\gamma_1 & \gamma_0 & E_{sp}+p\gamma_1 & q\gamma_0 \\ 0 & 0 & 0 & 0 & 0 & q\gamma_1 & q\gamma_0 & E_{sp}+p\gamma_1 \end{pmatrix}. \tag{2.46}$$

The Hamiltonian for Rashba spin orbit coupling in the tight-binding model reads:

$$\hat{H}_R = it_R \sum_{<i,j>} C^+_{i\sigma}\hat{\boldsymbol{z}}\cdot(S_{\sigma\sigma'}\times\boldsymbol{d}_{ij})C_{j\sigma'}. \tag{2.47}$$

It is noted that unlike the armchair nanoribbon, the hopping in zigzag nanoribbon in the unit cell should include the hopping from the neighbor unit cell. For example, The hopping from atomic site 12 to site 11 should include the hopping between $12''$ to site 11. In zigzag nanoribbon, there are only two different hopping.

a) From site 12 to site 11 and $12''$ to site 11:

$\boldsymbol{d}_{ij} = (\sqrt{3}/2, 1/2)$, $i(\boldsymbol{S}\times\boldsymbol{d}_{ij})\times e^{(ik_x\sqrt{3}/2a)} = i(\boldsymbol{S}_x 1/2 - \sqrt{3}/2\boldsymbol{S}_y)\times e^{(ik_x\sqrt{3}/2a)}$ $\boldsymbol{d}_{ij} = (-\sqrt{3}/2, 1/2)$, $i(\boldsymbol{S}\times\boldsymbol{d}_{ij})\times e^{(-ik_x\sqrt{3}/2a)} = i(\boldsymbol{S}_x 1/2 + \sqrt{3}/2\boldsymbol{S}_y)\times e^{(-ik_x\sqrt{3}/2a)}$.

In k-space, the corresponding element should read:

$$H_{12,11} = t_R\begin{pmatrix} 0 & i\cos(\frac{\sqrt{3}k_x a}{2}) - i\sqrt{3}\sin(\frac{\sqrt{3}k_x a}{2}) \\ i\cos(\frac{\sqrt{3}k_x a}{2}) + i\sqrt{3}\sin(\frac{\sqrt{3}k_x a}{2}) & 0 \end{pmatrix}. \tag{2.48}$$

b) From site 3 to site 2:

$\boldsymbol{d}_{ij} = (0, 1)$, $i(\boldsymbol{S} \times \boldsymbol{d}_{ij}) = i(1 \times \boldsymbol{S}_x - 0 \times \boldsymbol{S}_y)$ In k-space, the corresponding element should read:

$$H_{2,3} = t_R \begin{pmatrix} 0 & i \\ i & 0 \end{pmatrix}. \tag{2.49}$$

2.4 Kubo formula

In order to calculate the spin response to the electric field, we evaluate the current-induced spin density within the framework of linear response theory,

$$\boldsymbol{\delta} < \boldsymbol{S}_\alpha > (\boldsymbol{q}, \omega) = -\frac{i}{\Omega} \boldsymbol{x}_{\alpha,\beta}(\boldsymbol{q}, \omega) E_\beta(\boldsymbol{q}, \omega), \tag{2.50}$$

where $\boldsymbol{\delta} < \boldsymbol{S}_\alpha >$ is the current-induced spin density, E is the applied electric field, and $\boldsymbol{x}_{\alpha,\beta}$ the spin-current response function. The spin density is along the axis α and the index β sums over the x,y,z axis. We follow the standard procedure to find the spin-current response function. Suppose that at some time, an external perturbation is applied to the system. The Hamiltonian for the holes in electromagnetic field contains two parts: $\hat{H}$ is the Hamiltonian of the system. The second term stems from the external electromagnetic field, which is given by the coupling of the electrons to the vector potential.

$$\hat{H} = \hat{H}_0 - \int d\boldsymbol{r} \boldsymbol{J}(\boldsymbol{r}) \boldsymbol{A}(\boldsymbol{r}, t), \tag{2.51}$$

where $\boldsymbol{E} = \partial \boldsymbol{A} / \partial t$ is an external field. According to the Kubo formula, we can rewrite the spin density as:

$$\boldsymbol{\delta} < \boldsymbol{S}_\alpha(\boldsymbol{r}, t) > = \int d\boldsymbol{r}' \int dt' \boldsymbol{x}_{\alpha,\beta}(\boldsymbol{r} - \boldsymbol{r}'; t - t') \boldsymbol{A}_\beta(\boldsymbol{r}', t'), \tag{2.52}$$

and

$$\boldsymbol{x}_{\alpha,\beta}(\boldsymbol{r}-\boldsymbol{r}';t-t') = -i\theta(t-t') < [\boldsymbol{S}^I_\alpha(\boldsymbol{r},t), \boldsymbol{j}^I_\beta(\boldsymbol{r}',t')] >, \tag{2.53}$$

$<>$ is the thermal average of an operator $\hat{P}$, i.e., $< \hat{P} >= Tr[e^{\frac{-\hat{H}_{el}}{k_B t}}\hat{P}]$ and the symbol I stands for the interaction picture. We use the imaginary time τ to replace $\frac{i}{\hbar}t$. $\hat{P}_I = e^{\hat{H}\tau}\hat{P}e^{-\hat{H}\tau}$.

Using the Fourier transform, we can find the formula in momentum space

$$\boldsymbol{x}_{\alpha,\beta}(\boldsymbol{q}, i\Omega) = \int d\boldsymbol{r} \int d\tau_B e^{-i(\boldsymbol{q}\boldsymbol{r}-\Omega_n\tau_B)}\boldsymbol{x}_{\alpha,\beta}(\boldsymbol{r},\tau_B), \tag{2.54}$$

where $\Omega = 2\pi n k_B T$ is Matsubara frequency in the external field. We expand Eq.2.51 and then get:

$$\boldsymbol{x}_{\alpha,\beta}(\boldsymbol{q}, i\Omega_n) =< \boldsymbol{S}_\alpha(\boldsymbol{q},\Omega_n)\boldsymbol{j}_\beta(-\boldsymbol{q},-\Omega_n) > . \tag{2.55}$$

The spin and current density operator in momentum space can be written as

$$\boldsymbol{S}_\alpha(\boldsymbol{q}, i\Omega) = \frac{1}{\beta_B}\sum_{\boldsymbol{k},a,b,m} \psi^+_{\boldsymbol{k}a}(i\omega_m)(S_\alpha)_{ab}\psi_{\boldsymbol{k}+\boldsymbol{q},b}(i\omega_m + i\Omega_n), \tag{2.56}$$

$$\boldsymbol{J}_\alpha(\boldsymbol{q}, i\Omega) = \frac{1}{\beta_B}\sum_{\boldsymbol{k},a,b,m} \psi^+_{\boldsymbol{k}a}(i\omega_m)(J_\alpha)_{ab}\psi_{\boldsymbol{k}+\boldsymbol{q},b}(i\omega_m + i\Omega_n), \tag{2.57}$$

where $\omega_n = (2n+1)\pi n k_B T$ is the fermionic Matsubara frequency, and the $\psi^+_{\boldsymbol{k}a}$ is field operator. We define $(S_\alpha)_{a,b} = \frac{e}{\hbar}\langle\psi_{\boldsymbol{k}a}|\hat{S}_\alpha|\psi_{\boldsymbol{k}b}\rangle$ and $(j_\alpha)_{a,b} = \frac{e}{\hbar}\langle\psi_{\boldsymbol{k}a}|\frac{\partial\hat{H}}{\partial k_a}|\psi_{\boldsymbol{k}b}\rangle$. Here we ignore the diamagnetic contribution to the current. By using the Green's function

method, we can find the response function

$$\boldsymbol{x}_{\alpha,\beta}(\boldsymbol{q}, i\Omega_n) = -\frac{1}{\beta_B}\sum_m \sum_{\boldsymbol{k},a,b} (S_\alpha)_{a,b}(j_\beta)_{b,a}\hat{G}_{\boldsymbol{k},a}(i\omega_m)\hat{G}_{\boldsymbol{k}+\boldsymbol{q},b}(i\omega_m + i\Omega_n), \tag{2.58}$$

where $\hat{G}_{k,a}(i\omega_m) = (i\hbar\omega_m - (E_{ka} - E_f) + i/(2\ \tau sign(\omega_m))^{-1}$. In Eq. 2.58, we ignore the vertex corrections. We transform the Matsubara sum into contour integration. According to the residue theorem,

$$\frac{2\pi i}{\beta_B}\sum_m \boldsymbol{F}(i\omega_m) = \int_C dz f(z)\boldsymbol{F}(z), \tag{2.59}$$

then we can find

$$\frac{1}{\beta_B}\sum_m \boldsymbol{F}(i\omega_m) = \frac{1}{2\pi i}\int_C dz f(z)\boldsymbol{F}(z), \tag{2.60}$$

There are poles along the axis $Imz = 0$ and $Imz = -i\Omega_n$. For q=0, the function $\boldsymbol{F}(z)$ is

$$\boldsymbol{F}(z) = -\sum_{\boldsymbol{k},a,b} (S_\alpha)_{a,b}(j_\beta)_{b,a}\hat{G}_{\boldsymbol{k},a}(z)\hat{G}_{\boldsymbol{k}+\boldsymbol{q},b}(z + i\Omega_n). \tag{2.61}$$

By using the partial integration and choose the correct integration contour, we can get the final expression to calculate the spin density

$$\boldsymbol{x}_{\alpha,\beta} = -\frac{i\Omega}{2\pi}\sum_{\boldsymbol{k},a,b} Re[(S_\alpha)_{a,b}(\boldsymbol{j}_\beta)_{b,a}(\hat{G}^A_{k,a}\hat{G}^R_{k,b} - \hat{G}^R_{k,a}\hat{G}^R_{k,b})], \tag{2.62}$$

where $j = q\boldsymbol{v}$.Substituting the Eq. 2.62 into the Eq. 2.50, one has

$$\boldsymbol{\delta} < \boldsymbol{S}_\alpha > (\boldsymbol{q} = 0, \omega) = \frac{\hbar}{2\pi}\sum_{k,a,b} Re[(S_\alpha)_{a,b}(e\boldsymbol{v}\cdot\boldsymbol{E}(\boldsymbol{q} = 0, \omega))_{b,a}(\hat{G}^A_{k,a}\hat{G}^R_{k,b} - \hat{G}^R_{k,a}\hat{G}^R_{k,b})], \tag{2.63}$$

In the limit of $\boldsymbol{q} \to 0$, and then fixing to $\Omega \to 0$, we have

$$\boldsymbol{\delta} < \boldsymbol{S}_\alpha >= \frac{\hbar}{2\pi V} \sum_{\boldsymbol{k},a,b} Re[(S_\alpha)_{a,b}(e\boldsymbol{v}\cdot\boldsymbol{E})_{b,a}(\hat{G}^A_{k,a}\hat{G}^R_{k,b} - \hat{G}^R_{k,a}\hat{G}^R_{k,b})], \tag{2.64}$$

When band index ($\boldsymbol{k}$,a) is not equal to ($\boldsymbol{k}$,b), the calculated result is the interband spin density that we want.

2.5 Lattice Green's function method in graphene nanoribbons

We first define the time-dependent Heisenberg field operator

$$\hat{C}(x,t) = e^{\frac{i}{\hbar}Ht}\hat{C}e^{-\frac{i}{\hbar}Ht}. \tag{2.65}$$

Based on the field operator, we can define the time-ordered single particle Green's function at zero temperature

$$\hat{G}(x,x';t,t') = -\frac{i}{\hbar}\frac{\langle\psi_{x'\boldsymbol{t'}}|\hat{\boldsymbol{T}}\hat{C}(x,t)\hat{C}^+(x',t')|\psi_{x\boldsymbol{t}}\rangle}{\langle\psi_{x'\boldsymbol{t'}}|\psi_{x\boldsymbol{t}}\rangle}. \tag{2.66}$$

Here, $\hat{\boldsymbol{T}}$ is the time-order operator and it satifies $\hat{\boldsymbol{T}}A(t)B(t') = \Theta(t-t')A(t)B(t') - \Theta(t'-t)A(t')B(t)$. $|\psi_{n\boldsymbol{k}}\rangle$ is the ground states of the Hamiltonian. $\Theta(t-t')$ is Heaviside step function. At finite temperature, the Green's function is expressed as

$$\begin{aligned}\hat{G}(x,x';t,t') &= -\frac{i}{\hbar}Tr\{\rho\hat{\boldsymbol{T}}\hat{C}(x,t)\hat{C}^+(x',t')\} \\ &= -\frac{i}{\hbar} < \hat{\boldsymbol{T}}\hat{C}(x,t)\hat{C}^+(x',t') > .\end{aligned} \tag{2.67}$$

The brackets $< ... >$ denotes the thermal average and $\rho = e^{\hat{H}/kT}$ is a statistical operator. Following a standard way indicated in many textbooks, we also define the

retarded, advanced, greater, and lesser Green's function.

$$\hat{G}^r(x,x';t,t') = -\frac{i}{\hbar}\Theta(t-t') < \{\hat{C}(x,t),\hat{C}^+(x',t')\} >, \tag{2.68}$$

$$\hat{G}^a(x,x';t,t') = \frac{i}{\hbar}\Theta(t'-t) < \{\hat{C}(x,t),\hat{C}^+(x',t')\} >, \tag{2.69}$$

$$\hat{G}^>(x,x';t,t') = -\frac{i}{\hbar} < \hat{C}(x,t)\hat{C}^+(x',t') >, \tag{2.70}$$

$$\hat{G}^<(x,x';t,t') = \frac{i}{\hbar} < \hat{C}^+(x',t')\hat{C}(x,t) > . \tag{2.71}$$

Consider a non-interaction system and the retarded Green's function as the derivative with respect to the time argument in Eq. 2.65

$$\begin{aligned} & i\hbar\frac{\partial\hat{G}_0^r(x,x';t,t')}{\partial t} = \\ & (i\hbar)(-\frac{i}{\hbar}\frac{\partial\Theta(t-t')}{\partial t}) < \{\hat{C}(x,t),\hat{C}^+(x',t')\} > \\ & -(i\hbar)\frac{i}{\hbar}\Theta(t-t')\frac{\partial}{\partial t} < \{\hat{C}(x,t),\hat{C}^+(x',t')\} > \\ & = \delta(t-t')\delta(r-r') + \hat{H}_0\hat{G}_0^r(x,x';t,t'). \end{aligned} \tag{2.72}$$

By using the Fourier transform, we can work in the energy domain

$$\hat{G}^r(x,x';E) = \int d(t-t')e^{\frac{i}{\hbar}E(t-t')}\hat{G}^r(x,x';t-t'). \tag{2.73}$$

Similarly, we can transform the Eq. 2.68 from the time domain to the energy domain and then we have

$$\begin{aligned} & i\hbar\int d(t-t')e^{\frac{i}{\hbar}E(t-t')}\frac{\partial\hat{G}_0^r(x,x';t,t')}{\partial t} = \\ & \int d(t-t')e^{\frac{i}{\hbar}E(t-t')}[\delta(t-t')\delta(x-x') + \hat{H}\hat{G}_0^r(x,x';t,t')]. \end{aligned} \tag{2.74}$$

If one integrates by parts, we can find

$$E\hat{G}_0^r(x,x';E) = \delta(x-x') + \hat{H}\hat{G}_0^r(x,x';E). \tag{2.75}$$

$$\tag{2.76}$$

Finally, we induce a infinitesimal positive imaginary part to the energy for convergence and get the Green's function operator

$$\hat{G}_0^r(x,x';E) = \frac{1}{E-\hat{H}+i\epsilon}. \tag{2.77}$$

The Green's function operator is also named as "propagator". The retarded Green's function operator corresponds to the outgoing wave and is related to the transmission probability in a discrete Hamiltonian. Unfortunately, the dimension of the Hamiltonian matrix in the above equation is infinite. In general, one can divide a system into three parts: two leads and a scattering region in a matrix representation. There is no effective interaction and external fields in the leads.

$$\hat{H} = \begin{pmatrix} \hat{H}_L & \hat{H}_{LC} & 0 \\ \hat{H}_{LC} & \hat{H}_C & \hat{H}_{CR} \\ 0 & \hat{H}_{RC} & \hat{H}_R \end{pmatrix}.$$

In terms of the definition of Green's function in Eq. 2.54, one can find

$$\begin{pmatrix} \hat{G}_L^R & \hat{G}_{LC}^R & \hat{G}_{LR}^R \\ \hat{G}_{CL}^R & \hat{G}_C^R & \hat{G}_{CR}^R \\ \hat{G}_{RL}^R & \hat{G}_{RC}^R & \hat{G}_R^R \end{pmatrix} = \begin{pmatrix} E'-\hat{H}_L & -\hat{H}_{LC} & 0 \\ -\hat{H}_{CL} & E'-\hat{H}_C & -\hat{H}_{CR} \\ 0 & -\hat{H}_{RC} & E'-\hat{H}_R \end{pmatrix}^{-1}.$$

It is easy to find a group of equations according to the above matrix equation.

$$\hat{H}_{CL}\hat{G}_{LC} + E - \hat{H}_C\hat{G}_C + \hat{H}_{CR}\hat{G}_{RC} = I, \tag{2.78}$$

$$\hat{H}_{CL}\hat{G}_L + E - \hat{H}_C\hat{G}_{CL} = 0, \tag{2.79}$$

$$E - \hat{H}_C\hat{G}_{CR} + \hat{H}_{CR}\hat{G}_R = 0. \tag{2.80}$$

Substituting Eq. 2.79 and Eq. 2.80 into Eq. 2.78, then the Green's function in scattering region is obtained

$$\begin{aligned}\hat{G}^r_C(x, x'; E) &= \frac{1}{E' - \hat{H}_C - \hat{H}_{CL}\hat{g}_L\hat{H}_{LC} - \hat{H}_{CR}\hat{g}_R\hat{H}_{RC}} \\ &= \frac{1}{E - \hat{H}_C + i\epsilon - \Sigma_L - \Sigma_R},\end{aligned} \tag{2.81}$$

where $E' = E + i\epsilon$, $g_L = (E' - \hat{H}_L)^{-1}$ and $g_R = (E' - \hat{H}_R)^{-1}$ are surface Green's function of left and right lead. H_{LC} and H_{RC} are the coupling matrices between the central region and the left and right leads, respectively. The surface Green's function of left or right lead can be obtained by using Dyson equation recursively. The Dyson equation can be defined as :

$$\hat{G} = \hat{G}_0 + \hat{G}_0\hat{V}\hat{G} \tag{2.82}$$

where $\hat{G}_0$ is the Green's function calculated by the definition of Green's function for the unit cell of systems (the column for 2D or the surface for 3D), $\hat{V}$ is the hopping matrix and G is the Green's function that we need.

2.5.1 Spin denstiy in graphene nanoribbons

The particle density is related to the expectation value of the number operator in Eq. 2.53 at $t = t'$ and $r = r'$.

$$\hat{G}^{<}(x,x;t,t) = \frac{i}{\hbar} < \hat{C}^{+}(x,t)\hat{C}(x,t) >= \frac{i}{\hbar} n(x,t). \tag{2.83}$$

The lesser Green's function can be obtained by transforming the Green's function in energy domain.

$$\hat{G}^{<}(x,x';t-t') = \int \frac{dE}{2\pi} e^{\frac{i}{\hbar}E(t-t')} \hat{G}^{<}(x,x';E). \tag{2.84}$$

We consider a time-independent particle number, therefore one finds

$$n(x) = n(x)_{eq} + n(x)_{non-eq}, \tag{2.85}$$

$$n(x)_{eq} = \frac{1}{\pi} \int_{-\infty}^{E_f - eV/2} Im\hat{G}^{r}_{x,x}(E) dE. \tag{2.86}$$

$$\begin{aligned} n(x)_{non-eq} = &= -\frac{i}{2\pi} \int_{E_f - eV/2}^{E_f + eV/2} \hat{G}^{<}(x,x';E) dE \\ &= -\frac{i}{2\pi} \int_{E_f - eV/2}^{E_f + eV/2} [A_L(E) f_L(E) + A_R(E) f_R(E)] dE \\ &= -\frac{i}{2\pi} \int_{E_f - eV/2}^{E_f + eV/2} [\hat{G}_R(E)\Gamma_L \hat{G}_A(E) f_L(E) + \hat{G}_R(E)\Gamma_R \hat{G}_A(E) f_R(E)] dE. \end{aligned} \tag{2.87}$$

The first term corresponds to the equilibrium part, while the second term is the non-equilibrium part. In equilibrium, all the scattering states are filled up to the Fermi level. The degeneracy of spin states induced by the Rashba SOC is not broken due to the time-inversion-symmetry. The desired spin torque is not related to this part. In contrast, the non-equilibrium charge density should be obtained in energy regime from E-eV/2 to E+eV/2. We take the diagonal part of extended spectral function

$$\begin{aligned} n(x)_{non-eq} = &= -\frac{i}{2\pi}\int_{E_f-eV/2}^{E_f+eV/2}\hat{G}^{<}(x,x';E)dE \\ &= -\frac{i}{2\pi}\int_{E_f-eV/2}^{E_f+eV/2}[A_L(E)f_L(E)+A_R(E)f_R(E)]dE \\ &= -\frac{i}{2\pi}\int_{E_f-eV/2}^{E_f+eV/2}[\hat{G}_R(E)\Gamma_L\hat{G}_A(E)f_L(E)+\hat{G}_R(E)\Gamma_R\hat{G}_A(E)f_R(E)]dE. \end{aligned} \tag{2.88}$$

The spin density can be found

$$\boldsymbol{S_i^{ne}} = -\frac{i}{2\pi}\int_{E_f-eV/2}^{E_f+eV/2} Tr\{\hat{\boldsymbol{\Sigma}}_{\boldsymbol{i}}\cdot[\hat{G}_R(E)\Gamma_L\hat{G}_A(E)f_L(E)+\hat{G}_R(E)\Gamma_R\hat{G}_A(E)f_R(E)]\}dE. \tag{2.89}$$

In terms of the spin density the torque normalized to the plane spanned by $\boldsymbol{M}$ and spin density can be written as

$$\boldsymbol{T_n} = \boldsymbol{M}\times\boldsymbol{S}_i^{ne}. \tag{2.90}$$

Chapter 3

Microscopic Description of Spin Orbit Torque in Diluted Magnetic Semiconductors

The electrical manipulation of magnetization is central to spintronic devices such as high density magnetic random access memory [71], for which the spin transfer torque provides an efficient magnetization switching mechanism [72, 73]. Beside the conventional spin-transfer torque, the concept of spin-orbit torque in both metallic systems and diluted magnetic semiconductors (DMS) has been studied theoretically and experimentally [74, 75, 76, 77, 78, 79]. In the presence of a charge current, the spin-orbit coupling produces an effective magnetic field that generates a non-equilibrium spin density that in turn exerts a torque on the magnetization [74, 75, 76]. Several experiments on magnetization switching in strained (Ga,Mn)As have provided strong indications that such a torque can be induced by a Dresselhaus-type spin-orbit coupling, achieving critical switching currents as low as 10^6 A/cm^2 [77, 78, 79]. However, up to date very few efforts have been devoted to the nature of the spin-orbit torque in such a complex system and its magnitude and angular dependence remain unaddressed.

(Ga,Mn)As is a test bed for understanding the underlying physical mechanism behind diluted magnetic semiconductor and it is the best-understood diluted magnetic semiconductors up till now. The Curie temperature of (Ga,Mn)As is below the room temperature, and there are other diluted magnetic semiconductors such as (Ga,Mn)N with a Curie temperature above room temperature. However, (Ga,Mn)N grows in a wurtzite structure and usually presents a significant Jahn-Teller distortion that is large enough to suppress the spin-orbit coupling [80]. Furthermore, the formalism developed here applies to systems possessing delocalized holes and long range Mn-Mn interactions and is not adapted to the localized holes controlling the magnetism in (Ga,Mn)N.

We first study the spin-orbit torque in a diluted magnetic semiconductor submitted to a linear Dresselhaus spin-orbit coupling. We highlight two effects that have not been discussed before. First, a strong correlation exists between the angular dependence of the torque and the anisotropy of the Fermi surface. Second, the spin torque depends *nonlinearly* on the exchange coupling. To illustrate the flexibility offered by DMS in tailoring the spin-orbit torque, we compare the torques obtained in two stereotypical materials, (Ga,Mn)As and (In,Mn)As.

3.1 Extrinsic spin orbit torque

The system under investigation is a uniformly magnetized single domain DMS film made of, for example, (Ga,Mn)As or (In,Mn)As. We assume the system is well below its critical temperature. An electric field is applied along the $\hat{x}$ direction. It is worth pointing out that we consider here a large-enough system allowing us to disregard any effects arising from boundaries and confinement.

We use the *six-band* Kohn-Luttinger Hamiltonian to describe the band structure

of the DMS in Eq. (2.8) [79], If $\gamma_2 = \gamma_3 \neq 0$, the degeneracy between heavy holes and light holes is lifted but the two Fermi surfaces remain spherical. By setting $\gamma_2 \neq \gamma_3$, the Fermi surface around the Γ point becomes anisotropic, $\hat{\boldsymbol{J}}$ is the total angular momentum and k is the wave vector. The bulk inversion asymmetry allows us to augment the Kohn-Luttinger Hamiltonian by a strain-induced spin-orbit coupling of the Dresselhaus type [77, 75]. We assume the growth direction of (Ga,Mn)As is directed along the z-axis, two easy axes are pointed at x and y, respectively [81]. In this case, the components of the strain tensor ϵ_{xx} and ϵ_{yy} are identical. Consequently, we may have a linear Dresselhaus spin-orbit coupling [77]

$$\hat{H}_{\mathrm{DSOC}} = \beta(\hat{\sigma}_x k_x - \hat{\sigma}_y k_y), \tag{3.1}$$

given β the coupling constant that is a function of the axial strain [77, 82]. $\hat{\sigma}_{x(y)}$ is the 6×6 spin matrix of holes and $k_{x(y)}$ is the wave vector.

In the DMS systems discussed here, we incorporate a mean-field like exchange coupling to enable the spin angular momentum transfer between the hole spin ($\hat{\boldsymbol{s}} = \hbar\hat{\boldsymbol{\sigma}}/2$) and the localized ($d$-electron) magnetic moment $\hat{\boldsymbol{\Omega}}$ of ionized Mn^{2+} acceptors [83, 84],

$$\hat{H}_{\mathrm{ex}} = 2J_{\mathrm{pd}} N_{\mathrm{Mn}} S_a \hat{\boldsymbol{\Omega}} \cdot \hat{\boldsymbol{s}}/\hbar \tag{3.2}$$

where J_{pd} is the antiferromagnetic coupling constant [83, 85]. Here $S_a = 5/2$ is the spin of the acceptors. The hole spin operator, in the present six-band model, is a 6×6 matrix [83]. The concentration of the ordered local Mn^{2+} moments $N_{\mathrm{Mn}} = 4x/a^3$ is given as a function of x that defines the doping concentration of Mn ion. a is the

lattice constant. Therefore, the entire system is described by the total Hamiltonian

$$\hat{H}_{\rm sys} = \hat{H}_{\rm KL} + \hat{H}_{\rm ex} + \hat{H}_{\rm DSOC}. \tag{3.3}$$

In order to calculate the spin torque, we determine the nonequilibrium spin densities $\boldsymbol{S}$ (of holes) as a *linear* response to an external electric field [75],

$$\boldsymbol{S} = eE_x \frac{1}{V} \sum_{n,\boldsymbol{k}} \frac{1}{\hbar \Gamma_{n,\boldsymbol{k}}} \langle \hat{\boldsymbol{v}} \rangle \langle \hat{\boldsymbol{s}} \rangle \delta(E_{n,\boldsymbol{k}} - E_F). \tag{3.4}$$

where $\hat{\boldsymbol{v}}$ is the velocity operator. In Eq.(3.4), the scattering rate of hole carriers by Mn ions is obtained by Fermi's golden rule [84],

$$\begin{aligned} \Gamma_{n,\mathbf{k}}^{\rm Mn^{2+}} =& \frac{2\pi}{\hbar} N_{\rm Mn} \sum_{n'} \int \frac{d\boldsymbol{k'}}{(2\pi)^3} \left| M_{n,n'}^{\boldsymbol{k},\boldsymbol{k'}} \right|^2 \\ & \times \delta(E_{n,\boldsymbol{k}} - E_{n',\boldsymbol{k'}})(1 - \cos\phi_{\boldsymbol{k},\boldsymbol{k'}}), \end{aligned} \tag{3.5}$$

where $\phi_{\boldsymbol{k},\boldsymbol{k'}}$ is the angle between two wave vectors $\boldsymbol{k}$ and $\boldsymbol{k'}$. The matrix element $M_{n,n'}^{\boldsymbol{k},\boldsymbol{k'}}$ between two eigenstates $(\boldsymbol{k}, n)$ and $(\boldsymbol{k'}, n')$ is

$$\begin{aligned} M_{n,n'}^{\boldsymbol{k}\boldsymbol{k'}} =& J_{\rm pd} S_a \langle \psi_{n\boldsymbol{k}} | \hat{\boldsymbol{\Omega}} \cdot \hat{\boldsymbol{s}} | \psi_{n'\boldsymbol{k'}} \rangle \\ & - \frac{e^2}{\epsilon(|\boldsymbol{k} - \boldsymbol{k'}|^2 + p^2)} \langle \psi_{n\boldsymbol{k}} | \psi_{n'\boldsymbol{k'}} \rangle. \end{aligned} \tag{3.6}$$

Here ϵ is the dielectric constant of the host semiconductors and $p = \sqrt{e^2 g/\epsilon}$ is the Thomas-Fermi screening wave vector, where g is the density of states at Fermi level. Finally, we calculate the field like spin-orbit torque using [74]

$$\boldsymbol{T} = J_{\rm ex} \boldsymbol{S} \times \hat{\boldsymbol{\Omega}}, \tag{3.7}$$

where $J_{\rm ex} \equiv J_{\rm pd} N_{\rm Mn} S_a$. Throughout this Letter, the results are given in terms of

the torque efficiency $\boldsymbol{T}/eE$. The interband transitions, arising from distortions in the distribution function induced by the applied electric field, are neglected in our calculation. This implies that the torque extracted from the present model is expected to accommodate only a field-like component. The above protocols based on linear response formalism allow us to investigate the spin-orbit torque for a wide range of DMS material parameters. We plot in Fig.3.1(a) the spin torque as a function of the magnetization angle for different values of the band structure anisotropy parameter γ_3. The topology of the Fermi surface can be modified by a linear combination of γ_2 and γ_3: if $\gamma_2 = \gamma_3 \neq 0$, the Fermi surface around the Γ point is spherical, as shown in Fig.3.1(c). In this special case, the angular dependence of the torque is simply proportional to $\cos\theta$ [red curve in Fig.3.1(a)], as expected from the symmetry of the k-linear Dresselhaus Hamiltonian, Eq. (3.1) [74]. When $\gamma_3 \neq \gamma_2$, the Fermi surface deviates from a sphere [Fig.3.1(b) and (d)] and, correspondingly, the angular dependence of the torque deviates from a simple $\cos\theta$ function [i.e., curves corresponding to $\gamma_3 = 1.0$ and $\gamma_3 = 2.93$ in Fig.3.1(a)]. In a comparison to the spherical case, the maximal value of the torque at $\theta = 0$ is lower for $\gamma_3 \neq \gamma_2$. As Eq.(3.4) indicates, in the linear response treatment formulated here, the magnitude of the spin torque is determined by the transport scattering time and the expectation values of spin and velocity operators of holes. Qualitatively, as the Fermi surface deviates from a sphere, the expectation value $\langle \hat{s}_x \rangle$ of the heavy hole band, contributing the most to the spin torque, is lowered at $\theta = 0$.

More specifically, as the Fermi surface warps, the angular dependence of the spin torque develops, in addition to the $\cos\theta$ envelop function, an oscillation with a period that is shorter than π. The period of these additional oscillations increases as the Fermi surface becomes more anisotropic in k-space, see Fig. 3.1(b) and (d). To further reveal the effect of band warping on spin torque, we plot $T_y/\cos\theta$ as a function of the magnetization angle in inset of Fig.3.1(a). When $\gamma_3 = 2.0$ (spherical Fermi sphere),

$T_y/\cos\theta$ is a constant, for $T \propto \cos\theta$. When $\gamma_3 = 2.93$ or 1.0, the transport scattering time of the hole carriers starts to develop an oscillating behavior in θ [86], which eventually contributes to additional angular dependencies in the spin torque. The angular dependencies in spin-orbit torque shall be detectable by techniques such as spin-FMR [79].

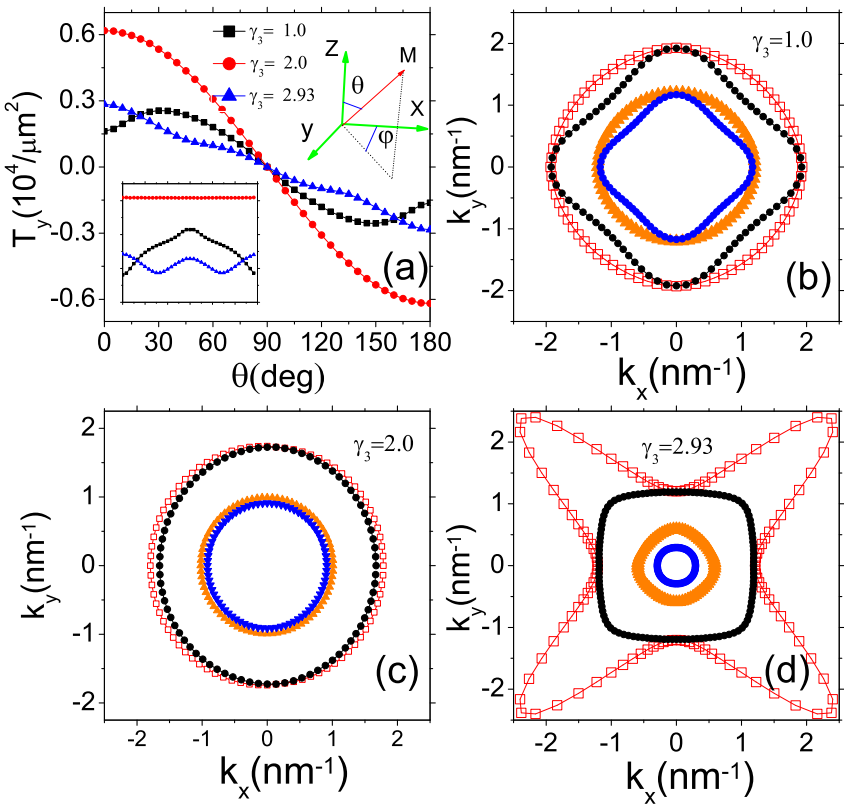

Figure 3.1: (Color online) (a)The y-component of the spin torque as a function of magnetization direction. Fermi surface intersection in the $k_z = 0$ plane for (b)$\gamma_3 = 1.0$, (c)$\gamma_3 = 2.0$ and (c)$\gamma_3 = 2.93$. The red, black, orange and blue contours stands for majority heavy hole, minority heavy hole, majority light hole and minority light hole band, respectively. Inset (a) depicts $T_y/\cos\theta$ as a function of magnetization direction. The others parameters are $(\gamma_1, \gamma_2) = (6.98, 2.0)$, $J_{\rm pd} = 55$ meV nm^3 and $p = 0.2$ nm^{-3}.

In Fig.3.2, we compare the angular dependence of spin torque (T_y) for both (Ga,Mn)As and (In,Mn)As which are popular materials in experiments and device fabrication [87, 88, 89]. Although (In,Mn)As is, in terms of exchange coupling and

general magnetic properties, rather similar to (Ga,Mn)As, the difference in band structures, lattice constants, and Fermi energies between these two materials gives rise to different density of states, strains, and transport scattering rates. For both materials, the spin torque decrease monotonically as the angle θ increases from 0 to $\pi/2$. Throughout the entire angle range $[0, \pi]$, the amplitude of the torque in (In,Mn)As is twice larger than that in (Ga,Mn)As. We mainly attribute this to two effects. First of all, the spin-orbit coupling constant β in (In,Mn)As is about twice as larger than that in (Ga,Mn)As. Second, for the same hole concentration, the Fermi energy of (In,Mn)As is higher than that of (Ga,Mn)As.

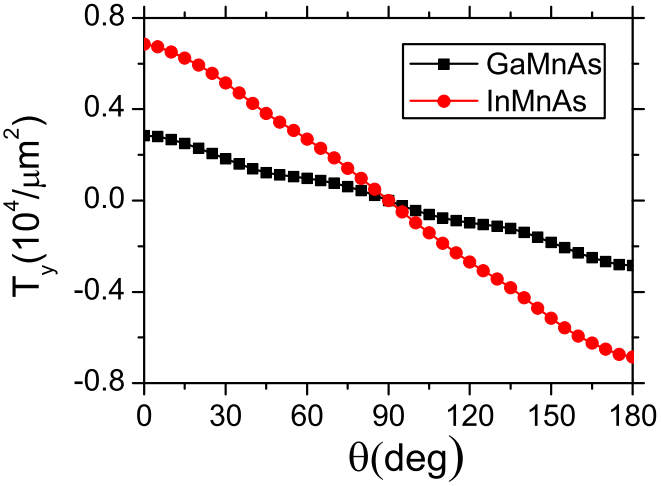

Figure 3.2: (Color online) Torque T_y as a function of the magnetization direction for (Ga,Mn)As (black square) and (In,Mn)As (red dots). For (Ga,Mn)As, $(\gamma_1, \gamma_2, \gamma_3) = (6.98, 2.0, 2.93)$; for (In,Mn)As, $(\gamma_1, \gamma_2, \gamma_3) = (20.0, 8.5, 9.2)$. The strength of the spin-orbit coupling constant is: for (Ga,Mn)As, $\beta = 1.6$ meV nm; for (In,Mn)As, $\beta = 3.3$ meV nm [90]. The exchange coupling constant $J_{\rm pd} = 55$ meV nm^3 for (Ga,Mn)As [91] and 39 meV nm^3 for (In,Mn)As [92].

In the following, we further demonstrate a counter-intuitive feature that, in the DMS system considered in this Letter, the spin orbit torque depends nonlinearly on the exchange splitting. In Fig. 3.3(a), T_y component of the spin torque is plotted as a function of the exchange coupling $J_{\rm pd}$, for different values of β. In the weak exchange coupling regime, the electric generation of non equilibrium spin density

dominates, then the leading role of exchange coupling is defined by its contribution to the transport scattering rate. We provide a simple qualitative explanation on such a peculiar $J_{\rm pd}$ dependence. Using a Born approximation, the scattering rate due to the $p-d$ interaction is proportional to $1/\tau_J = bJ_{\rm pd}^2$, where parameter b is $J_{\rm pd}$- independent. When the nonmagnetic scattering rate $1/\tau_0$ is taken into account, i.e., the Coulomb interaction part in Eq.(3.6), the total scattering time in Eq.(3.4) can be estimated as

$$\frac{1}{\hbar\Gamma} \propto \frac{1}{bJ_{\rm pd}^2 + \frac{1}{\tau_0}}, \tag{3.8}$$

which contributes to the torque by $T \propto J_{\rm pd}/(\hbar\Gamma)$. This explains the transition behavior, i.e., increases linearly then decreases, in the moderate $J_{\rm pd}$ regime in Fig.3.3. As the exchange coupling further increases, Eq.(3.8) is dominated by the spin-dependent scattering, therefore the scattering time $1/\hbar\Gamma \propto 1/J_{\rm pd}^2$. Meanwhile, the energy splitting due to the exchange coupling becomes significant, thus $\langle \hat{\boldsymbol{s}} \rangle \propto J_{\rm pd}$. In total, the spin torque is insensitive to $J_{\rm pd}$, explaining the flat curve in the large exchange coupling regime. In Fig. 3.3(b), we plot the influence of the exchange coupling on the spin torque for two materials. In (In,Mn)As, mainly due to a larger Fermi energy in a comparison to (Ga,Mn)As, the peak of the spin torque shifts towards a larger $J_{\rm pd}$. The dependence of the torque as a function of the exchange in (In,Mn)As is more pronounced than in (Ga,Mn)As, due to a stronger spin-orbit coupling.

The possibility to engineer electronic properties by doping is one of the defining features that make DMS promising for applications. Here, we focus on the doping effect which allows the spin torque to vary as a function of hole carrier concentration. In Fig. 3.4(a), the torque is plotted as a function of the hole concentration for different β parameters. With the increase of the hole concentration, the torque increases due to an enhanced Fermi energy. In the weak spin-orbit coupling regime (small β), the

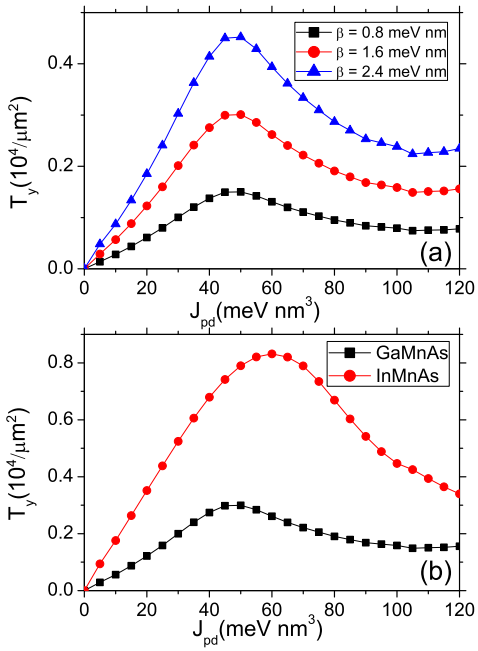

Figure 3.3: (Color online) The T_y component of the spin torque as a function of exchange coupling $J_{\rm pd}$. (a) T_y versus $J_{\rm pd}$ at various values of β, for (Ga,Mn)As. (b) T_y versus $J_{\rm pd}$, for both (Ga,Mn)As and (In,Mn)As. The magnetization is directed along the z-axis ($\theta = 0$). The other parameters are the same as those in Fig.3.2.

torque as a function of the hole concentration (p) follows roughly the $p^{1/3}$ curve as shown in the inset in Fig. 3.4(a). The spherical Fermi sphere approximation and a simple parabolic dispersion relation allow for an analytical expression of the spin torque, i.e., in the leading order in β and $J_{\rm ex}$,

$$T = \frac{m^*}{\hbar}\frac{\beta J_{\rm ex}}{E_F}\sigma_{\rm D} \tag{3.9}$$

where m^* is the effective mass. The Fermi energy E_F and the Drude conductivity are given by

$$E_F = \frac{\hbar^2}{2m^*}(3\pi^2 p)^{2/3},\ \ \sigma_D = \frac{e^2\tau}{m^*}p, \tag{3.10}$$

where τ is the transport time. The last two relations immediately give rise to $T \propto p^{1/3}$.

In the six-band model, the Fermi surface deviates from a sphere and, as the value of β increases, the spin-orbit coupling starts to modify the density of states. Both effects render the torque-versus-hole concentration curve away from the $p^{1/3}$ dependence. This effect is illustrated in Fig. 3.4(b). The former (strong spin-orbit coupling) clearly deviates from $p^{1/3}$, whereas the latter (weak spin-orbit coupling) follows the expected $p^{1/3}$ trend.

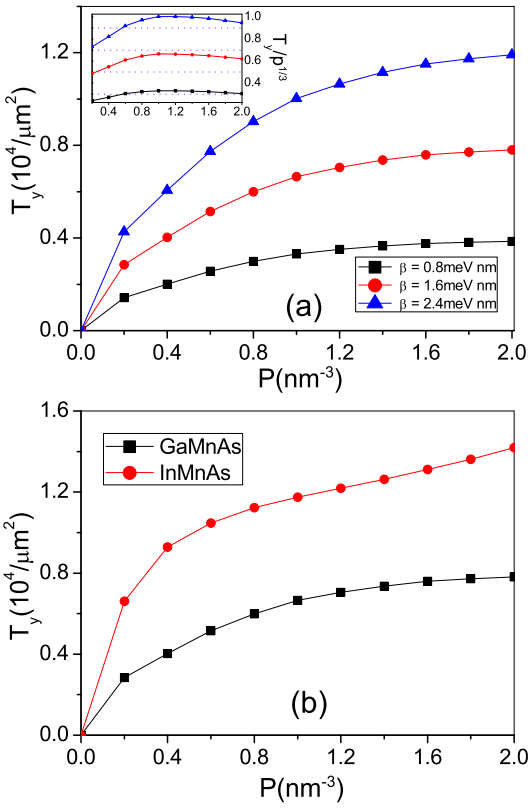

Figure 3.4: (Color online) The y-component of the spin torque as a function of hole concentration. (a) The y-component of the spin torque versus hole concentration at different β. (b) spin torque versus hole concentration in (Ga,Mn)As and (In,Mn)As. For (Ga,Mn)As, $J_{\rm pd} = 55$ meV nm^3; for (In,Mn)As, $J_{\rm pd} = 39$ meV nm^3. The other parameters are the same as in Fig.3.3.

3.2 Interband versus intraband transitions

Two main mechanisms have been invoked to explain the origin of the current-driven torques in non-centrosymmetric ferromagnets. In the first scenario, the lack of inversion symmetry enables the generation of an inverse spin galvanic effect (ISGE), i.e. the flowing current directly produces a nonequilibrium spin density $\delta\mathbf{S}$ locally, whose direction is determined by the symmetry of the spin-orbit coupling. This effect was originally predicted by Edelstein in non-magnetic, asymmetrically grown two-dimensional electron gases. Recently, it has been proposed that in non-centrosymmetric magnetic materials this nonequilibrium spin density may exert a torque on the magnetization [74, 75] $\mathbf{T} = (2J_{\mathrm{ex}}/\hbar\gamma N_m)\mathbf{m} \times \delta\mathbf{S}$, where γ is the gyromagnetic ratio, N_m the density of magnetic moments and J_{ex} the exchange coupling (having the dimension of energy) between the itinerant electron spins and the local magnetization $\mathbf{M} = M_s\mathbf{m}$ which is assumed to arise from localized magnetic moments μ only so that the saturated magnetization $M_s = \mu N_m$. This is the essence of SOTs. Alternatively, in ferromagnets adjacent to a heavy metal, it has also been proposed that the spin Hall effect (SHE) present in the heavy metal may inject a spin-polarized current into the adjacent ferromagnet, exerting a torque of the form $\mathbf{T} = \mathbf{m} \times (\mathcal{J}_{\mathrm{int}} \times \mathbf{m})$, where $\mathcal{J}_{\mathrm{int}}$ is the interfacial spin current arising from the SHE. By symmetry, the spin current flowing across the interface is polarized in the direction $\mathbf{z} \times \mathbf{j}_e$, where $\mathbf{z}$ is normal to the interface and $\mathbf{j}_e$ is the charge current [93, 94]. Whereas both effects are present in metallic bilayers, only ISGE takes place in bulk strained DMS.

A current debate aims at identifying the interplay between these different mechanisms and their impact in terms of current-driven spin torque. In the simplest physical picture, SHE induces a anti-damping-like torque, while the SOT reduces to a field-like torque generated by ISGE [94]. However, it has been recently proposed

that the incomplete absorption of the SHE-induced spin current by the ferromagnet (or, equivalently, the non-vanishing imaginary part of the interfacial spin mixing conductance) may result in a field-like component [94]. Similarly, in the context of ISGE-induced SOT, recent theories have suggested that spin relaxation and dephasing may also lead to a correction in the SOT in the form of a anti-damping-like component [95, 96, 97, 98]. In Refs. [96] and [97], the anti-damping-like SOT term arises from the electron scattering-induced spin relaxation. In Ref. [94], the semiclassical diffusion formalism was used, whereas in Refs. [95] and [98], the anti-damping-like SOT is obtained within a quantum kinetic formalism and ascribed to spin-dependent carrier lifetimes [95] or to a term arising from the weak-diffusion limit, which in the leading order is proportional to a constant carrier lifetime [98]. Intriguing material-dependence of the SOTs has been unravelled in various experiments keeping the debate on the origin of these components open [99, 100, 101, 102, 103]. The difficulty in determining the physical origin of the torques partly lies in the complexity of the ultrathin bilayer considered, involving both bulk and interfacial transport in the current-in-plane configuration. First principle calculations have indeed pointed out the significant sensitivity of the torques to the nature of the interfaces [104].

In a recent publication, Kurebayashi et al. [105] investigated the SOT in a bulk DMS. They observed a large anti-damping-like torque that cannot be ascribed to the SHE since no adjacent heavy metal is present. It was then proposed that such a torque is scattering-independent and originates from the Berry curvature of the band structure, in a similar spirit as the intrinsic SHE was introduced about ten years ago [106].

Here we present an extended theoretical study of the extrinsic and intrinsic current-driven SOTs in a magnetic system lacking inversion symmetry. We focus our attention on the current-driven spin-orbit field (called the SOT field), $\mathbf{h}^{\mathrm{so}}$, producing the spin-orbit torque $\mathbf{T} = \mathbf{M} \times \mathbf{h}^{\mathrm{so}}$. In particular, in addition to the *in-plane* SOT field

of the ISGE origin $\mathbf{h}_{\parallel}^{\mathrm{so}} = \tau_{\mathrm{FL}}\mathbf{u}_{\mathrm{so}}$ [i.e. lying in the $(\mathbf{m}, \mathbf{u}_{\mathrm{so}})$ plane and producing an out-of-plane torque], we show that the intrinsic contribution arising from interband transitions produces an *out-of-plane* field of the form $\mathbf{h}_{\perp}^{\mathrm{so}} = \tau_{\mathrm{DL}}\mathbf{u}_{\mathrm{so}} \times \mathbf{m}$ [i.e. lying perpendicular to the $(\mathbf{m}, \mathbf{u}_{\mathrm{so}})$ plane]. Analytical expressions are obtained in the prototypical case of a magnetic Rashba two-dimensional electron gas (2DEG), while numerical calculations are performed on DMSs modeled by 4×4 Luttinger Hamiltonian. Parametric dependences of the different torque components and similarities to the analytical results of the Rashba two-dimensional electron gas in the weak disorder limit are described.

3.2.1 Intraband and Interband Contributions in Kubo formula

In the present study, we consider a general single-particle Hamiltonian

$$\hat{H}_{\mathrm{sys}} = \hat{H}_0 + \hat{H}_{\mathrm{SOC}} + \hat{H}_{\mathrm{ex}} + V_{\mathrm{imp}}(\mathbf{r}) - e\mathbf{E} \cdot \hat{\mathbf{r}}, \tag{3.11}$$

where the first term includes the spin-independent kinetic and potential energies of the particle, the second term denotes the coupling between the carrier spin and its orbital angular momentum and the third one represents the interaction between the spin of the carrier and the magnetization of the ferromagnetic system. Below, we refer to these first three terms as to the unperturbed part of the Hamiltonian. The fourth term is the impurity potential and the fifth term is the electric field applied through the system. Impurities are treated within the constant relaxation time approximation while the electric field is treated within the framework of the linear response theory. As discussed below, this electric field has two distinct effects on the electronic system: (i) it modifies the carrier distribution function from its equilibrium Fermi-Dirac form and (ii) it distorts the carrier wave functions. The

former leads to intraband ISGE contributions, while the latter is responsible for the interband (Berry curvature) contribution. To calculate the SOT field, we evaluate first the nonequilibrium spin density $\delta\mathbf{S}$ using the Kubo formula in Eq. 2.64, where $G^R_{\mathbf{k}a} = (G^A_{\mathbf{k}a})^* = 1/(E_F - E_{\mathbf{k}a} + i\Gamma)$, E_F is the Fermi energy, $E_{\mathbf{k}a}$ is the energy dispersion of band a, V is the system volume and Γ is the spectral broadening due to the finite lifetime of the particle in the presence of impurities. The Bloch state $|\psi_{\mathbf{k}a}\rangle$ in band a can be found by diagonalizing the unperturbed part of the Hamiltonian in Eq. (3.11). This expression contains both intraband ($a = b$) and interband ($a \neq b$) contributions to the nonequilibrium spin density. Numerical results in Section 3.2.4 are calculated with the above equation.

In order to understand the numerical results, Eq. (2.64) can be rewritten as $\delta\mathbf{S} = \delta\mathbf{S}^{\text{intra}} + \delta\mathbf{S}^{\text{inter}}_1 + \delta\mathbf{S}^{\text{inter}}_2$ when weak impurity scattering (namely, small spectral broadening, $\Gamma \to 0$) is assumed. The three contributions are

$$\begin{aligned}
\delta\mathbf{S}^{\text{intra}} &= \frac{1}{V}\frac{e\hbar}{2\Gamma}\sum_{\mathbf{k},a}\langle\psi_{\mathbf{k}a}|\hat{\mathbf{s}}|\psi_{\mathbf{k}a}\rangle\langle\psi_{\mathbf{k}a}|\mathbf{E}\cdot\hat{\mathbf{v}}|\ \psi_{\mathbf{k}a}\rangle \\
&\quad\times\delta(E_{\mathbf{k}a} - E_F), \qquad (3.12)\\
\delta\mathbf{S}^{\text{inter}}_1 &= -\frac{e\hbar}{V}\sum_{\mathbf{k},a\neq b}2\text{Re}[\langle\psi_{a\boldsymbol{k}}|\hat{\mathbf{s}}|\psi_{b\boldsymbol{k}}\rangle\langle\psi_{b\boldsymbol{k}}|\mathbf{E}\cdot\hat{\mathbf{v}}|\psi_{a\boldsymbol{k}}\rangle] \\
&\quad\times\frac{\Gamma(E_{\mathbf{k}a} - E_{\mathbf{k}b})}{[(E_{\mathbf{k}a} - E_{\mathbf{k}b})^2 + \Gamma^2]^2}(f_{\mathbf{k}a} - f_{\mathbf{k}b}). \qquad (3.13)\\
\delta\mathbf{S}^{\text{inter}}_2 &= -\frac{e\hbar}{V}\sum_{\mathbf{k},a\neq b}\text{Im}[\langle\psi_{\mathbf{k}a}|\hat{\mathbf{s}}|\psi_{\mathbf{k}b}\rangle\langle\psi_{\mathbf{k}b}|\mathbf{E}\cdot\hat{\mathbf{v}}|\psi_{\mathbf{k}a}\rangle] \\
&\quad\times\frac{\Gamma^2 - (E_{\mathbf{k}a} - E_{\mathbf{k}b})^2}{[(E_{\mathbf{k}a} - E_{\mathbf{k}b})^2 + \Gamma^2]^2}(f_{\mathbf{k}a} - f_{\mathbf{k}b}). \qquad (3.14)
\end{aligned}$$

The first term, Eq. (3.12), is the intraband ($a = b$) contribution arising from the perturbation of the carrier distribution function by the electric field. It is proportional to the momentum scattering time ($\tau = \hbar/2\Gamma$) and is therefore an *extrinsic* contribution to the nonequilibrium spin density (i.e. it is impurity-dependent). The

second and third terms are interband ($a \neq b$) contributions arising from the perturbation of the carrier wave functions by the electric field. The second term, Eq. (3.13), is inversely proportional to the scattering time, while the third term, Eq. (3.14), is independent of the scattering in the weak scattering limit ($E_{\mathbf{k}a} - E_{\mathbf{k}b} \gg \Gamma$). The former is therefore another *extrinsic* contribution whereas the latter is an *intrinsic* contribution to the nonequilibrium spin density. The formalism described above is the established linear response theory of a translationally invariant system and has been exploited, for instance, in the context of the spin Hall and anomalous Hall effect [107]. Nevertheless, the distinction between these different contributions is particularly important in the case of the SOT since these terms give rise to different symmetries of the torque.

The concept of intrinsic SOT is illustrated in Fig. 3.5 (see also the discussion in Ref. [105]). Figure 3.5(a) represents the Fermi surface of a non-magnetic Rashba 2DEG under the application of an external electric field $\mathbf{E}$. At equilibrium ($\mathbf{E} = 0$) the spin direction (pink arrows) is tangential to the Fermi surface (grey circle) at all k-points, and the total spin density vanishes. Applying the electric field accelerates the electrons on the Fermi surface and they feel a modified spin-orbit field $\delta\mathbf{B} \propto \mathbf{z} \times \dot{\mathbf{p}} \equiv \mathbf{z} \times \mathbf{E}$ (thick blue arrow) around which the spin momenta (red arrows) start to precess. In the limit of a non-magnetic 2DEG, the resulting spin density vanishes. Now, let us consider the case of a magnetic Rashba 2DEG in the strong ferromagnetic limit [Fig. 3.5(b)]. At equilibrium, the spin momenta (pink arrows) are mostly aligned along the magnetization direction $\mathbf{m}$ (thin black arrow) for all k-points of the Fermi surface (grey circle). Under the application of an external electric field, the spin momenta (red arrows) precess around $\delta\mathbf{B}$ (thick blue arrow) resulting in a non-vanishing spin density. Following the convention adopted in Fig. 3.5(b), the electric field is applied along $\mathbf{y}$, the displacement of the Fermi surface produces a spin density along $\mathbf{x}$ and the spin precession around $\delta\mathbf{B}$ produces a spin density

aligned along **z**. The latter results in an additional torque that does not depend on the disorder [105]. This simple picture can be extended to more complex spin-orbit coupling situation and only requires inversion symmetry breaking in the system.

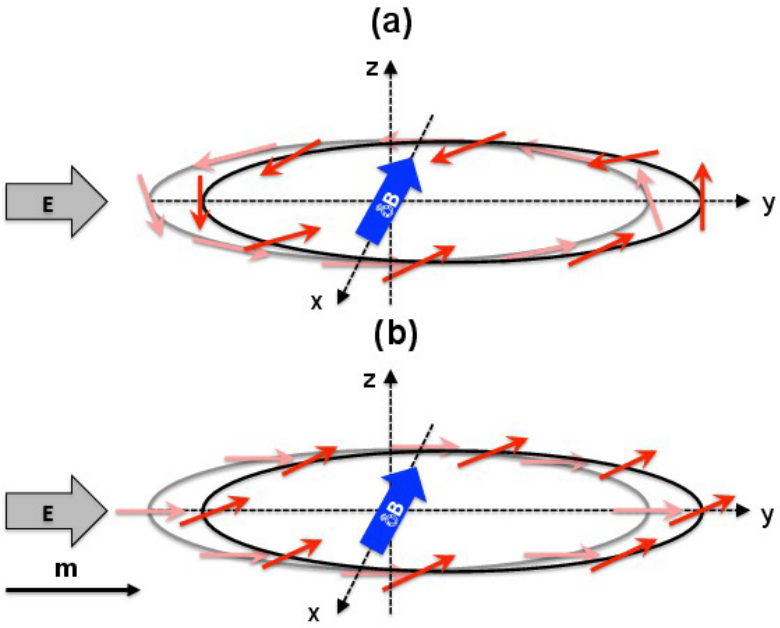

Figure 3.5: (Color online) (a) Fermi surface of a non-magnetic Rashba 2DEG: under the application of an external electric field (thick cyan arrow), a non-equilibrium field $\delta\mathbf{B}$ is produced (thick blue arrow) that distorts the spin direction out of the plane (red arrows). After averaging, the spin density vanishes. (b) Fermi surface of a magnetic Rashba 2DEG in the strong ferromagnetic regime: in this case, since the spin directions (pink arrows) are initially mostly aligned along the magnetization **m** (black arrow), the resulting non-equilibrium spin density (red arrows) does not vanish and is aligned along **z**.

We remark that Eqs. (2.64) and (3.14) are also the basis of semiclassical Boltzmann and quantum mechanical Kubo formula calculations of current-driven SOTs in uniform (Ga,Mn)As performed by Garate and MacDonald [75]. We use this computational approach in our detailed analysis of the SOT which we present in the following sections. Here we point out, however, that the notion of the SOT as a consequence of a unidirectional current-induced magnetocrystalline anisotropy energy, introduced in Ref. [75] (but not used for the calculations), is misleading. This is

particularly apparent in the semiclassical Boltzmann transport theory in which the entire intraband SOT stems from the non-equilibrium redistribution of carriers on the Fermi surface of the system. Since the Fermi surface is an equal-energy surface, the total energy (sum of energies of all occupied states) is unchanged by the Fermi surface redistribution. The magnetocrystalline anisotropy energy is the difference between total energies for different magnetization orientations. Therefore, if the total energy is unchanged by the current, there is also no current-induced change of the magnetocrystalline anisotropy.

3.2.2 Two-dimensional Rashba ferromagnet

We first apply this formalism to a ferromagnetic 2DEG in the presence of Rashba spin-orbit coupling. This system is the prototypical free-electron model for SOTs in ultra thin ferromagnets embedded between two asymmetric interfaces [74, 108, 75]. Although the actual band structure of magnetic bilayers such as Pt/Co is complex, recent first principle calculations indicate that this simple Rashba model qualitatively captures most of the relevant physics at these interfaces [104]. This section is therefore developed mostly for pedagogical purposes in order to make the dependence on various parameters explicit. The unperturbed Hamiltonian in Eq. (3.11) can be rewritten as:

$$\hat{H}_{\mathrm{2DEG}} = \frac{\hbar^2 k^2}{2m^*} - \alpha \hat{\boldsymbol{\sigma}} \cdot (\mathbf{z} \times \mathbf{k}) + J_{\mathrm{ex}} \mathbf{m} \cdot \hat{\boldsymbol{\sigma}}. \tag{3.15}$$

where $\mathbf{k} = (k_x, k_y, 0) = k(\cos\varphi_k, \sin\varphi_k, 0)$, α is the Rashba parameter and the magnetization direction is $\mathbf{m} = (\cos\varphi \sin\theta, \sin\varphi \sin\theta, \cos\theta)$. By diagonalizing Eq. (3.15),

the eigenvalues and eigenvectors of itinerant electrons are

$$E_{\mathbf{k}\pm} = \frac{\hbar^2 k^2}{2m^*} \pm \Delta_{\mathbf{k}}, \tag{3.16}$$

$$\Delta_{\mathbf{k}} = \sqrt{J_{\rm ex}^2 + \alpha^2 k^2 + 2\alpha k J_{\rm ex} \sin(\varphi - \varphi_k) \sin\theta}, \tag{3.17}$$

$$|\mathbf{k}, +\rangle = \begin{pmatrix} e^{i\gamma_{\mathbf{k}}} \cos\frac{\chi_k}{2} \\ \sin\frac{\chi_k}{2} \end{pmatrix}; |\mathbf{k}, -\rangle = \begin{pmatrix} -e^{i\gamma_{\mathbf{k}}} \sin\frac{\chi_k}{2} \\ \cos\frac{\chi_k}{2} \end{pmatrix} \tag{3.18}$$

where we have $\cos\chi_k = J_{\rm ex}\cos\theta/\Delta_{\mathbf{k}}$ and $\tan\gamma_{\mathbf{k}} = \frac{\alpha k\cos\varphi_k + J_{\rm ex}\sin\varphi\sin\theta}{\alpha k\sin\varphi_k - J_{\rm ex}\cos\varphi\sin\theta}$. The velocity operator is given by $\hat{\mathbf{v}} = \frac{\hbar}{m^*}\mathbf{k} + \frac{\alpha}{\hbar}\mathbf{z}\times\hat{\boldsymbol{\sigma}}$. Exploiting Eqs. (3.12)-(3.14) in the weak exchange limit ($\alpha k_{\rm F} \gg J_{\rm ex} \gg \Gamma$), the nonequilibrium spin density reads

$$\delta\mathbf{S}^{\rm intra} = \frac{1}{4\pi}\frac{\alpha m^*}{\hbar^2\Gamma}(\mathbf{z}\times e\mathbf{E}) \tag{3.19}$$

$$\delta\mathbf{S}_1^{\rm inter} = -\frac{1}{8\pi}\frac{\Gamma}{\alpha E_F}(\mathbf{z}\times e\mathbf{E}) \tag{3.20}$$

$$\delta\mathbf{S}_2^{\rm inter} = \frac{1}{4\pi}\frac{J_{\rm ex}}{\alpha E_F}(\mathbf{m}\cdot\mathbf{z})e\mathbf{E} \tag{3.21}$$

and in the strong exchange limit ($J_{\rm ex} \gg \alpha k_{\rm F} \gg \Gamma$),

$$\delta\mathbf{S}^{\rm intra} = \frac{1}{2\pi}\frac{\alpha m^*}{\hbar^2\Gamma}\mathbf{m}\times[(\mathbf{z}\times e\mathbf{E})\times\mathbf{m}] \tag{3.22}$$

$$\delta\mathbf{S}_1^{\rm inter} = -\frac{1}{2\pi}\frac{\alpha m^*\Gamma}{\hbar^2 J_{\rm ex}^2}\mathbf{m}\times[(\mathbf{z}\times e\mathbf{E})\times\mathbf{m}] \tag{3.23}$$

$$\delta\mathbf{S}_2^{\rm inter} = -\frac{1}{2\pi}\frac{\alpha m^*}{\hbar^2 J_{\rm ex}}\mathbf{m}\times(\mathbf{z}\times e\mathbf{E}) \tag{3.24}$$

In summary, the SOT field defined as $\mathbf{h} = J_{\rm ex}\delta\mathbf{S}/\gamma\hbar N_m$, takes on the following form in the two limits:

$$J_{\rm ex} \ll \alpha k_{\rm F}\colon\ \mathbf{h} = \frac{J_{\rm ex}\alpha m^*}{4\pi\gamma N_m\hbar^3\Gamma}\left(1-\frac{\Gamma^2}{\alpha^2 k_{\rm F}^2}\right)(\mathbf{z}\times e\mathbf{E}) + \frac{J_{\rm ex}^2}{4\pi\gamma N_m\hbar\alpha E_F}(\mathbf{m}\cdot\mathbf{z})e\mathbf{E}, \tag{3.25}$$

$$J_{\rm ex} \gg \alpha k_{\rm F}\colon\ \mathbf{h} = \frac{J_{\rm ex}\alpha m^*}{2\pi\gamma N_m\hbar^3\Gamma}\left(1-\frac{\Gamma^2}{J_{\rm ex}^2}\right)\mathbf{m}\times[(\mathbf{z}\times e\mathbf{E})\times\mathbf{m}] + \frac{\alpha m^*}{2\pi\gamma N_m\hbar^3}\mathbf{m}\times(\mathbf{z}\times e\mathbf{E}) \tag{3.26}$$

Three important facts ought to be pointed out. First, the extrinsic contributions (either intra- or interband) both give rise to an in-plane SOT field [even in magnetization, lying in the $(\mathbf{m}, \mathbf{z}\times\mathbf{E})$ plane]. The resulting extrinsic torque is then out-of-plane and odd in magnetization. Second, the intrinsic contribution [second term in Eqs. (3.25) and (3.26)] only produces a SOT field odd in magnetization. It lies perpendicular to the $(\mathbf{m}, \mathbf{z}\times\mathbf{E})$ plane in the strong exchange limit, see Eq. (3.26). This term is *independent* of the exchange $J_{\rm ex}$, in sharp contrast with the ISGE-induced SOT field, while in the weak exchange limit, Eq. (3.25), it is second order in exchange and proportional to $m_z e\mathbf{E}$. The resulting intrinsic torque is in-plane and even in magnetization. As will be seen in the next section, the parameters dependence displayed in Eqs. (3.25) and (3.26) is not restricted to the simple case of the Rashba model. Third, notice that in the strong exchange limit the ratio of the anti-damping-like to the field like torque is $\approx \Gamma/J_{\rm ex}$. This dependence is the inverse of what was found in Refs. [95] and [98] in the diffusive limit and ignoring the interband scattering, where the ratio between the two torques is governed by $J_{\rm ex}/\Gamma$. A corrective anti-damping-like torque proportional to $\Gamma_{\rm sf}/J_{\rm ex}$ is also obtained when considering a finite spin-flip relaxation time $\tau_{\rm sf} = \hbar/\Gamma_{\rm sf}$ [98, 95].

In the case of the anomalous Hall effect, the intrinsic contribution dominates over

the extrinsic contributions in the strong scattering limit [109, 107]. As a consequence, one is tempted to anticipate that the intrinsic contribution to the SOT discussed presently becomes important when strong momentum scattering is present (such as in disordered Pt/Co interfaces for example) and dominates over the corrections found in Refs. [98, 95] in this limit. Nevertheless, these different contributions have been derived in different limits — i.e. strong [98, 95] versus weak scattering (this work) — and should to be treated on equal footing for a rigorous comparison (e.g., see Ref. [109]). Such a comprehensive model is beyond the scope of the present work.

3.2.3 Dilute Magnetic Semiconductors

Method

We now extend the previous results beyond the simple ferromagnetic 2DEG model with Rashba spin-orbit coupling. We consider a bulk three-dimensional DMS, such as (Ga,Mn)As, with a homogeneous magnetization. In order to model the SOT field of (Ga,Mn)As, we adopt a Hamiltonian including a mean-field exchange coupling between the hole spin ($\hat{\mathbf{J}}$) and the localized (d-electron) magnetic moment $\mu S_a \mathbf{m}$ of ionized Mn^{2+} acceptors [83, 84] and a four-band strained Luttinger Hamiltonian. The total Hamiltonian of the DMS reads

$$\hat{H}_{\mathrm{DMS}} = \hat{H}_{\mathrm{L}} + \hat{H}_{\mathrm{strain}} + J_{\mathrm{pd}} N_{\mathrm{Mn}} S_a \mathbf{m} \cdot \hat{\mathbf{J}} \tag{3.27}$$

where $J_{\mathrm{pd}} = 55\ \mathrm{meV} \cdot \mathrm{nm}^3$ is the antiferromagnetic coupling constant for (Ga,Mn)As and $S_a = 5/2$ is the localized Mn spin. The hole spin operator is a 4×4 matrix [83]. The concentration of the ordered local Mn^{2+} moments $N_{\mathrm{Mn}} = 4x/a^3$ is the product of x that defines the doping by Mn^{2+} ions and inverse volume per Ga atom (a is the GaAs lattice constant). The Luttinger Hamiltonian in Eq. (3.27) is expressed as

[110]

$$\hat{H}_{\mathrm{L}} = \frac{\hbar^2}{2m}\Big[\gamma_1 k^2 \hat{\mathrm{I}} - 4\gamma_3[k_x k_y\{\hat{\mathrm{J}}_x, \hat{\mathrm{J}}_y\} + c.p.] \\ -2\gamma_2[(\hat{\mathrm{J}}_x^2 - \frac{1}{3}\hat{\mathbf{J}}^2)k_x^2 + c.p.]\Big]. \tag{3.28}$$

This Hamiltonian applies close to the Γ point to centro-symmetric crystals with a diamond structure and strong spin-orbit coupling in the valence bands. The Luttinger parameters for GaAs are $(\gamma_1, \gamma_2, \gamma_3) = (6.98, 2.06, 2.93)$, $\hat{\mathrm{I}}$ is the 4×4 unity matrix, $\hat{\mathrm{J}}_x$, $\hat{\mathrm{J}}_y$, and $\hat{\mathrm{J}}_z$, are the angular momentum matrices for spin $\frac{3}{2}$. They follow the relation $\{\hat{\mathrm{J}}_x, \hat{\mathrm{J}}_y\} = (\hat{\mathrm{J}}_x\hat{\mathrm{J}}_\mathrm{y} + \hat{\mathrm{J}}_y\hat{\mathrm{J}}_\mathrm{x})/2$, and *c.p.* denotes cyclic permutation of the preceding term. The first term denotes the kinetic energy of the holes. The second and third terms are associated with the spin-orbit coupling of the diamond crystal. In zinc-blende crystals, such as GaAs, bulk inversion asymmetry gives rise to the so-called cubic Dresselhaus spin-orbit coupling [111]. We neglect this term in the present study since there is no experimental indication that it contributes significantly to the SOT in (Ga,Mn)As. $\hat{H}_{\mathrm{DMS}}$ should be understood as an effective model attempting to describe the current-driven SOT in (Ga,Mn)As rather than the complete description of the electronic structure in this material. In a cubic diamond crystal, $\gamma_2 \neq \gamma_3$. When $\gamma_2 = \gamma_3$, dispersions following from Eq. (3.28) become spherically symmetric and when the spin-orbit coupling is removed completely ($\gamma_1 = 2.0, \gamma_2 = \gamma_3 = 0$), Eq. (3.28) reduces to a parabolic model. The impact of these three degrees of approximation (parabolic model, spherical approximation and diamond crystal) on the SOT will be addressed in Section 3.2.4.

At this level of approximation the effective Hamiltonian, Eq. (3.28), does not break bulk inversion symmetry even though the actual crystal of the host GaAs does. Indeed, although the full model of GaAs contains additional terms that are odd in $\mathbf{k}$, it is experimentally established that the SOT in (Ga,Mn)As is sensitive to the strain.

We therefore assume, in line with experiments [79], that the key inversion-breaking term is proportional to the strain. The strain Hamiltonian is given by

$$\begin{aligned}\hat{H}_{\text{strain}} &= C_4[\hat{\mathrm{J}}_x k_x(\epsilon_{yy}-\epsilon_{zz}) + c.p.] \\ &+ C_5[(\hat{\mathrm{J}}_x k_y - \hat{\mathrm{J}}_y k_x)\epsilon_{xy} + c.p.]\end{aligned} \tag{3.29}$$

where ϵ_{ii} and ϵ_{ij} $(i \neq j)$ are the diagonal and non-diagonal elements of the strain tensor, respectively. We assume $\epsilon_{xx} \equiv \epsilon_{yy}$ and $\epsilon_{xy} \equiv \epsilon_{yx}$.

In Eq. (3.29), the first term ($\propto C_4$) originates from the lattice mismatch between the crystal structure of the substrate and the one of the ferromagnet, and produces a spin-orbit coupling with Dresselhaus symmetry ($\propto \epsilon_{zz}$). The second term ($\propto C_5$) is the shear strain and possesses the symmetry of Rashba spin-orbit coupling ($\propto \epsilon_{xy}$). Among the different terms linear in $\mathbf{k}$ and resulting from the inversion symmetry breaking, $\hat{H}_{\text{strain}}$ is the only one that acts in the manifold of heavy and light-hole states. It is worth pointing out that we consider here a large-enough system that allows us to disregard any effects arising from boundaries and confinement. In the following, we assume $C_4 = C_5 = 0.5$ eV·nm [79, 77] and mostly consider, however, only the lattice mismatch strain (with $\epsilon_{zz} \neq \epsilon_{yy} = \epsilon_{xx} = 0$ and $\epsilon_{xy} = 0$). Physical presence of the shear strain ($\epsilon_{xy} \neq 0$) in unpatterned (Ga,Mn)As samples is below the detection limit [112], yet it has been introduced in previous studies to model the in-plane uniaxial anisotropy [113]. Calculations with nonzero ϵ_{xy} are explicitly pointed out in the following.

The SOT field $\mathbf{h} = J_{\text{pd}}\delta\mathbf{S}/\gamma\hbar$ is evaluated once the energies $E_{\mathbf{k}a}$ and eigenfunctions $|\psi_{\mathbf{k}a}\rangle$ implied by the Hamiltonian in Eq. (3.27) are numerically calculated and the current-driven spin density $\delta\mathbf{S}$ is determined using Eq. (2.64). In general, the SOT

field can be decomposed as

$$\mathbf{h} = h_{\mathrm{m}}\mathbf{m} + h_{\parallel}\hat{e}_{\parallel} + h_{\perp}\hat{e}_{\perp} \tag{3.30}$$

where vectors $\hat{e}_{\parallel}, \hat{e}_{\perp}$ have unit length, $\hat{e}_{\perp}||\mathbf{m} \times \mathbf{u}$, $\hat{e}_{\parallel} = \hat{e}_{\perp} \times \mathbf{m}$, the subscript "so" has been removed for simplicity, and the direction of $\mathbf{u}$ (whose length is also set equal to one) should be chosen depending on the system. For example, we find $\mathbf{u}||\mathbf{z} \times \mathbf{E}$ for the Rashba 2DEG. On the other hand, $\mathbf{u} = \mathbf{x}$ in (Ga,Mn)As with growth strain ($\propto \epsilon_{zz}$) as described by Eq. (3.27) and current flowing along the [100] crystallographic direction. Our results presented below always assume $\hat{e}_{\perp}$ pointing in the positive $\mathbf{z}$ direction.

In the following, we disregard the component of the SOT field which is parallel to the magnetization (h_{m}) since it does not exert any torque on it. The two remaining components in Eq. (3.30) turn out to produce, in (Ga,Mn)As, the anti-damping-like SOT in the case of $h_{\perp}$ which is due to *intrinsic* interband mixing (of impurity-independent origin) and a combination of anti-damping-like and field-like *extrinsic* SOT in the case of $h_{\parallel}$ which depends through Γ on the disorder strength. The angular dependence of the two components, $h_{\parallel,\perp}$, reflects the details of the band structure as discussed in Sec. 3.2.4.

3.2.4 Numerical Results

For all the calculations presented in this section, the electric field $E = 0.02$ V/nm is assumed to be applied along the x-axis and we varied the hole concentration between 0.3 nm^{-3} and 1 nm^{-3}. This corresponds, respectively, to a Fermi energy of about 200 and 450 meV. Except for Sec. 3.2.4, magnetization always lies along the y-axis ($\varphi = 90°$).

Intrinsic Versus Extrinsic Spin-Orbit Torques

We first investigate the impact of impurity scattering on the intraband and interband contributions to the SOT fields. Figure 3.6 displays the SOT field as a function of the energy broadening Γ for different values of hole concentrations. Although Γ is of the order of hundreds of meV in realistic (Ga,Mn)As, we choose $\Gamma < 10$ meV so as to be able to compare these results with the analytical ones obtained in Sec. 3.2.2 for the ferromagnetic Rashba 2DEG which are valid in the small Γ limit.

The intraband contribution to the SOT field, $h_{\parallel}^{\text{intra}}$, is inversely proportional to Γ for all hole densities as it is seen in Fig. 3.6(a). This agrees with Eq. (3.12) and also Eqs. (3.19,3.22) which ensue for the ferromagnetic Rashba 2DEG. No $h_{\perp}^{\text{intra}}$ component exists. On the other hand, the interband part ($a \neq b$) of Eq. (2.64) contributes both to $h_{\parallel}$ and $h_{\perp}$ which is shown in Fig. 3.6(b,c). The former is a correction to the intraband SOT field and it scales $h_{\parallel}^{\text{inter}} \propto \Gamma$ in the weak scattering limit. It tends to counteract the intraband contribution, as it is the case in the ferromagnetic Rashba 2DEG described by Eqs. (3.25,3.26). The out-of-plane component $h_{\perp}^{\text{inter}}$ converges to a finite value when Γ vanishes, indicating the intrinsic character of this part of the SOT field. These results are consistent with the analytical solutions obtained in Eqs. (3.22)-(3.24) in the ferromagnetic Rashba 2DEG and weak scattering limit. It is worth noticing that this dependence on spectral broadening holds over a wide range of Γ in the case of intraband contribution [see inset in Fig. 3.6(a)], while it breaks down already for Γ equal to few meV for the interband contributions.

Ferromagnetic splitting

The band structure of (Ga,Mn)As changes with the Mn doping that would, in the absence of the SOI, lead to a rigid mutual shift of the majority- and minority-spin bands. Such ferromagnetic splitting would be proportional to $J_{\text{ex}} = J_{pd} N_{\text{Mn}}$ and we can distinguish two limiting situations in a system where the SOI is present: $E_{SO} \ll J_{\text{ex}}$

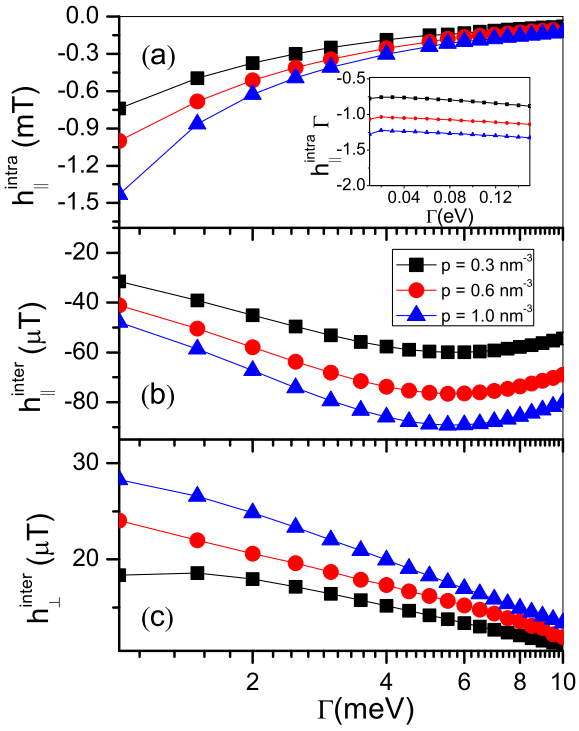

Figure 3.6: (Color online) (a) Intraband and (b)-(c) interband contributions to the SOT field as a function of spectral broadening Γ for otherwise typical (Ga,Mn)As sample (doping concentration $x = 5\%$, lattice-mismatch strain $\epsilon_{zz} = -0.3\%$). Inset of panel (a) shows that $h_{\parallel}^{\rm intra} \propto 1/\Gamma$ holds over a broad range of Γ. Only lattice-mismatch strain is considered, so that $\epsilon_{xy} = 0$ in Eq. (3.29).

and $E_{SO} \gg J_{\rm ex}$. In view of the analytical results presented in Sec. 3.2.2, it is meaningful to take $E_{SO} = \alpha k_F$ in the Rashba 2D system. For each component of the non-equilibrium spin-density $\delta\mathbf{S}^{\rm intra}$, $\delta\mathbf{S}_1^{\rm inter}$, $\delta\mathbf{S}_2^{\rm inter}$, there is a transition between different types of behaviour in the two limits. For example, the out-of-plane component of the SOT field $\mathbf{h}$ changes from the $\propto J_{\rm ex}^2$ behaviour in the $\alpha k_F \gg J_{\rm ex}$ limit implied by Eq. (3.21) into a $J_{\rm ex}$-independent behaviour in the opposite $\alpha k_F \ll J_{\rm ex}$ limit implied by Eq. (3.24). We checked that this transition occurs also in the numerical calculations across the whole range of $J_{\rm ex}$.

Contrary to the Rashba 2D system, the situation is more complicated in (Ga,Mn)As because of the additional SOI terms in Eq. (3.28). Due to their mutual competition,

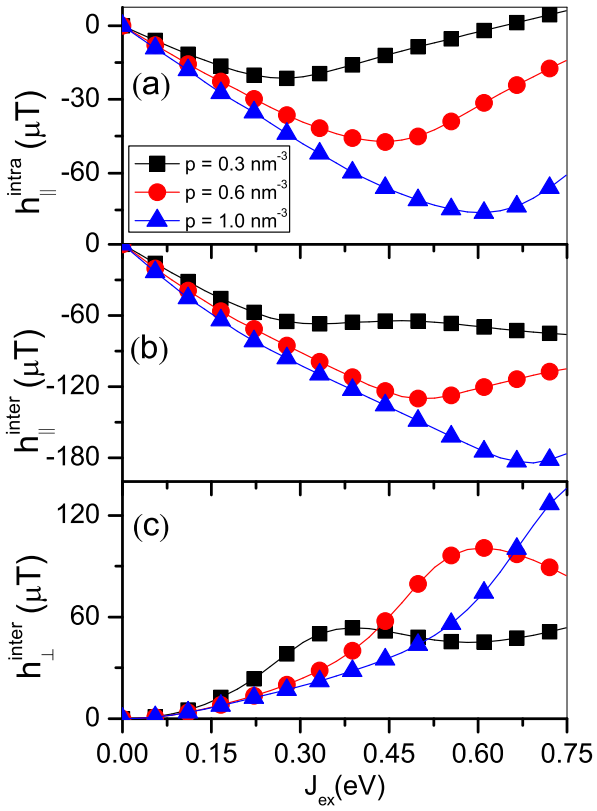

Figure 3.7: (Color online) (a) Intraband and (b)-(c) interband SOT field as a function of exchange interaction $J_{\rm ex} = J_{pd}N_{\rm Mn}$. Varied values of $J_{\rm ex}$ can be understood as a proxy to different Mn doping concentrations, e.g. $x = 5\%$ corresponds to $J_{\rm ex} = 0.06$ eV, the spectral broadening is set to 50 meV and other parameters are the same as in Fig. 3.6.

it is not obvious what E_{SO} should be. Looking at the $J_{\rm ex}$-dependence of the individual SOT field components in Fig. 3.7, we nevertheless recognize similarities to the $E_{SO} \gg J_{\rm ex}$ limit behaviour of the Rashba 2D system. To some extent, this is a surprising finding since the disorder broadening used for calculations in Fig. 3.7 is quite large ($\Gamma = 50$ meV), better corresponding to realistic (Ga,Mn)As samples but further away from the assumptions used to derive the analytical results presented in Sec. 3.2.2. When $J_{\rm ex}$ is small, both $h_{\parallel}^{\rm intra}$ and $h_{\parallel}^{\rm inter}$ are proportional to $J_{\rm ex}$ as seen in Eqs. (3.19) and (3.20), respectively. On the other hand, $h_{\perp}^{\rm inter} \propto J_{\rm ex}^2$ in the bottom panel of Fig. 3.7 which is reminiscent of Eq. (3.21). No similarities to the Rashba 2D system behaviour of the opposite limit ($E_{SO} \ll J_{\rm ex}$) are found in our calculations for

(Ga,Mn)As.

Hole concentration

We display in Fig. 3.8 the SOT field as a function of the hole density for different magnitudes of the lattice-mismatch strain ϵ_{zz}. First of all, we notice that the SOT field components increase linearly with the strain. Second, increase of the hole concentration results in an increase in the in-plane SOT field $h_{\parallel}$ approximatively following a $p^{1/3}$ law, as shown in Fig. 3.8(a,b). This is consistent with Eq. (17) in Ref. [114] in case of the intraband component. Interestingly, the in-plane interband SOT field $h_{\parallel}^{\text{inter}}$ shows a similar tendency [Fig. 3.8(b)], while the out-of-plane interband SOT field $h_{\perp}^{\text{inter}}$ has a different dependence on p. This anti-damping-like SOT field in Fig. 3.8(c) first increases with the hole concentration in the low hole density regime and later decreases towards a saturated value. This could be because of the competition of the different SOI types in (Ga,Mn)As as noticed by Kurebayashi et al. [105]. Indeed, when the diamond-lattice spin-orbit coupling is absent ($\gamma_2 = \gamma_3 = 0$), the out-of-plane interband SOT field $h_{\perp}^{\text{inter}}$ increases with the hole concentration following the same $p^{1/3}$ law as for the in-plane field [see inset of Fig. 3.8(c)]. For a four-band Luttinger model that includes band warping ($\gamma_2 \neq \gamma_3$), the competition between the diamond spin-orbit coupling and the strain-induced spin-orbit coupling results in a reduction of $h_{\perp}^{\text{inter}}$, as shown in Fig. 4 of Ref. [105]. The reason why the competition between the diamond spin-orbit coupling and the strain-induced spin-orbit coupling leads to the deviation from the analytical formula only in the case of the $h_{\perp}^{\text{inter}}$ and not for $h_{\parallel}^{\text{intra,inter}}$ remains to be explored in detail.

At this point, we remark that shear strain in Eq. (3.29) leads to $h_{\parallel}^{\text{intra}}$ comparable to values shown in Fig. 3.8(a) when the value of ϵ_{xy} is comparable to ϵ_{zz} used in Fig. 3.8. However, since the relevant values of ϵ_{xy} in unpatterned epilayers are typically order-of-magnitude lower [113] than those of ϵ_{zz}, we can typically expect

an order-of-magnitude smaller $h_{\parallel}^{\text{intra}}$ originating from the C_5-term in Eq. (3.29) as compared to the C_4-term.

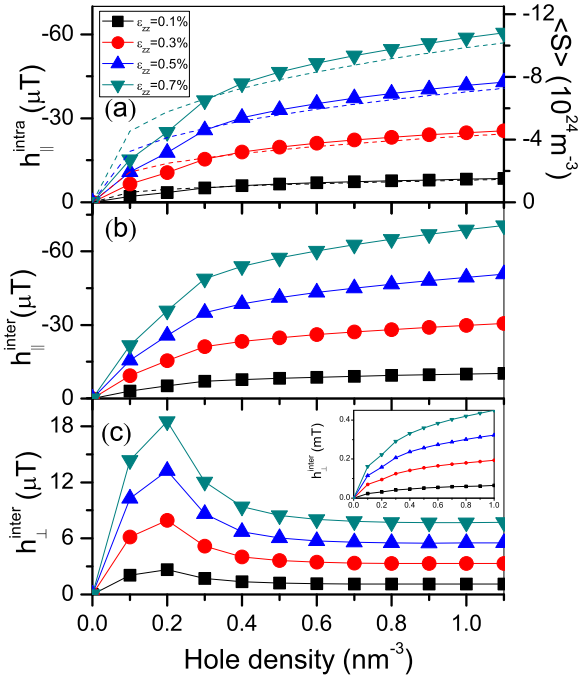

Figure 3.8: (Color online) (a) Intraband and (b)-(c) interband SOT field as a function of hole concentration for different lattice-mismatch strain ϵ_{zz}. Inset in (c): interband SOT field in the parabolic model. The dashed lines in panel (a) are calculated using Eq. (17) in Ref. [114] and follow a $p^{1/3}$-law. Parameters are the same as in Fig. 3.7 except for $J_{pd}N_{\text{Mn}}$ fixed to a value corresponding to Mn doping $x = 5\%$.

Impact of the Band Structure

The total DMS Hamiltonian given in Eq. (3.27) has both centro-symmetric and non-centro-symmetric components given by Eqs. (3.28) and (3.29), respectively. As discussed in the previous section, the spin-orbit coupling of the centro-symmetric component of the Hamiltonian [i.e., the terms in Eq. (3.28) proportional to γ_2 and γ_3] affects also the SOT field, notably their dependence on the magnetization direction [recall the definition of φ and θ below Eq. (3.15)]. Apart from the findings of Ref. [105]

discussed above, it was shown in Ref. [115] that the shape of the Fermi surface has a strong impact on the angular dependence of the intraband SOT field $h_{\parallel}^{\text{intra}}$.

We now systematically explore the influence of the spin-orbit coupling of the diamond crystal on the different components of the SOT field, i.e. $h_{\parallel}^{\text{intra}}$, $h_{\parallel}^{\text{inter}}$ and $h_{\perp}^{\text{inter}}$. The centro-symmetric component of the total DMS Hamiltonian, Eq. (3.28), accounts for the spin-orbit coupling through a set of the Luttinger parameters, $\gamma_{1,2,3}$. By tuning these three parameters, one can modify the form of the centro-symmetric spin-orbit coupling. We model three distinct cases: (i) the parabolic approximation where no centro-symmetric spin-orbit coupling is present ($\gamma_1 = 2.0, \gamma_2 = \gamma_3 = 0$), (ii) the spherical approximation where the centro-symmetric spin-orbit coupling is turned on but spherical symmetry is retained ($\gamma_2 = \gamma_3 = 2.5$) and (iii) the diamond crystal where both cubic symmetry and centro-symmetric spin-orbit coupling are accounted for ($\gamma_2 \neq \gamma_3$). This approach allows us to identify the role of the last two terms of Eq. (3.28) on the SOT fields. In Fig. 3.9, we show the angular dependence of the different contributions to the SOT field for the spin-orbit coupling induced by the lattice-mismatch strain in the context of models (i)–(iii). The magnetization lies in the (x, y) plane ($\theta = \pi/2$) and its direction is given by the azimuthal angle φ.

As expected from the symmetry of the C_4 term in Eq. (3.29), the three components of the SOT field have a dependence of the form $\sin\varphi$ in the parabolic model ($\square$ symbols in Fig. 3.9). When diamond-lattice spin-orbit coupling is switched on but the spherical approximation is assumed, the interband SOT fields [$\triangle$ symbols in Figs. 3.9(b) and (c)] deviate from this dependence, while the angular dependence of the intraband term remains unaffected [$\triangle$ symbols in Figs. 3.9(a)]. Furthermore, the magnitudes of interband and intraband SOT fields strongly decrease. This is a manifestation of the competition between the strain-induced terms in Eq. (3.29) with the centro-symmetric Luttinger spin-orbit terms in Eq. (3.28) [105].

When the spherical approximation is lifted ($\gamma_2 \neq \gamma_3$) electronic bands become

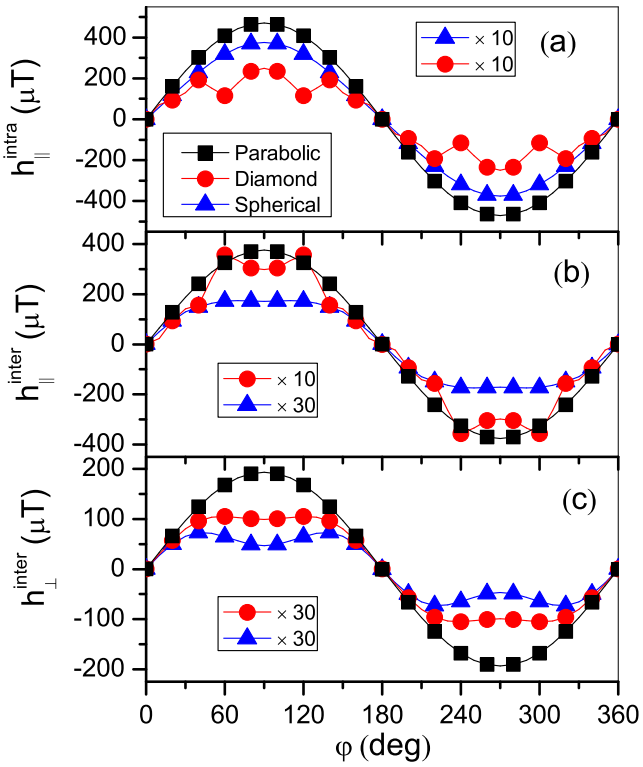

Figure 3.9: (Color online) Intraband and interband SOT field as a function of the magnetization direction for different models labelled (i), (ii) and (iii) in the text. The red (◯), blue (△) and black (□) data stand for the full four-band Luttinger model, its spherical approximation and the parabolic model, respectively. The parameters are the same as in Fig. 3.8 except for fixed $p = 1.0$ nm^{-3} and $\epsilon_{zz} = -0.3\%$.

warped, especially those of the heavy holes. This results into an increase of the interband SOT fields and an additional angular dependence shown by ◯ symbols in Fig. 3.9. Microscopically, the latter effect is caused by the distorted spin textures on the Fermi surface. The influence of the centro-symmetric spin-orbit field on the spin torque in GaMnAs has also been identified by Haney et al. [116] in DMS spin-valves.

Chapter 4

Valley-Dependent Spin-Orbit Torques in Two Dimensional Graphene-Like Materials

4.1 Introduction

The inverse spin galvanic effect (ISGE), referring to the electrical or optical generation of a nonequilibrium spin density in non-centrosymmetric materials, has attracted much attention over the last years [117, 118, 119, 120, 121, 62]. It originates from the momentum relaxation of carriers in an electrical field and their asymmetric redistribution in subbands that are spin-split by spin-orbit coupling [118]. ISGE was first observed in bulk tellurium and soon generalized to low-dimensional structures such as GaAs quantum wells [119, 120].

From an applied perspective, in ferromagnets lacking inversion symmetry ISGE enables the electrical control of the local magnetization through angular momentum transfer, a mechanism called spin-orbit torque (SOT) [120, 121, 62]. This effect has been scrutinized in dilute magnetic semiconductors such as ferromagnetic bulk (Ga,Mn)As [64, 122, 123] and metallic multilayers comprising heavy metals and

ferromagnets [124, 125]. These observations have been recently extended to bilayers involving topological insulators displaying extremely large SOT efficiencies [126, 127]. We note that in metallic multilayers, spin Hall effect in the adjacent heavy metal also leads to a torque [128, 129], which complicates the interpretation of the underlying physics.

From a theoretical perspective, the torque stemming from ISGE on the magnetization $\mathbf{M}$ has the general form

$$\mathbf{T} = T_{\mathrm{DL}}\mathbf{M} \times (\mathbf{u} \times \mathbf{M}) + T_{\mathrm{FL}}\mathbf{M} \times \mathbf{u}, \tag{4.1}$$

where the first term is called the antidamping-like torque and the second term is referred to as the field-like torque [95, 96, 115, 130, 131, 132]. The antidamping-like torque is *even* in magnetization direction and competes with the damping, while the field-like torque is *odd* in magnetization direction and acts like a magnetic field. The vector $\mathbf{u}$ depends on the current direction $\mathbf{j}$ and the symmetries of the spin-orbit coupling. For instance, in a ferromagnetic two-dimensional electron gas (normal to $\mathbf{z}$) with Rashba spin-orbit coupling, $\mathbf{u} = \mathbf{z} \times \mathbf{j}$ [74]. An interesting aspect of the formula given above is that the antidamping-like torque arises from the distortion of the wavefunction induced by the electric field, a mechanism closely related to the material′s Berry curvature [133, 130, 134].

In parallel to the development of SOT in ferromagnetic structures, the study of spin-orbit coupled transport has also been extended to low-dimensional hexagonal crystals such as graphene. Experimentally, a spin-splitting induced by Rashba spin-orbit coupling has been observed in graphene grown on heavy metals or surface alloys [135, 136]. Furthermore, a ferromagnetic insulator EuO was successfully deposited on graphene and spin-polarized states were detected [137, 138, 139]. The recent fabrication of low-dimensional hexagonal crystals with strong intrinsic spin-orbit coupling

such as silicene [140, 141], germanene [142] and possibly stanene [143], has enriched the graphene physics. These materials offer a rich platform for the investigation of spin, orbital and valley-dependent phenomena [144, 36]. The wide tunability of their model band structure presents an interesting opportunity to study the impact of the band geometry (e.g. their Berry curvature) on nonequilibrium mechanisms such as SOTs.

In this chapter, we theoretically investigate the nature of SOT in two-dimensional hexagonal IV group elements crystals such as graphene, silicene, germanene and stanene. Using Kubo formula, we investigate the impact of the band structure on the different components of SOT. We find that intrinsic spin-orbit coupling affects the antidamping-like and field-like components differently. The former is sensitive to the presence of a staggered potential while the latter is not. We understand these results in terms of Berry curvature origin of the antidamping torque. The presence of both magnetization and staggered potential enables the emergence of a valley-dependent antidamping torque, providing an additional degree of freedom to the system.

4.2 Model and Method

A possible structure to realize valley-dependent SOT is a single-layered hexagonal lattice (such as graphene, silicene, germanene or stanene) sandwiched by a ferromagnetic layer and a non-magnetic substrate (see Fig. 4.1(a)). The ferromagnetic layer may be chosen as EuO [145], or YIG [146], which induces a weak exchange coupling on the spin-polarized carriers. The underlying non-magnetic provides Rashba spin-orbit coupling [147, 148, 149, 150]. Note that in principle, a magnetic insulator could supply for both exchange field and Rashba spin-orbit coupling [101, 151, 152].

The concept of valley-dependent SOT is illustrated in Fig. 4.1(a). In the absence of a magnet, the interaction between the substrate and graphene-like layer breaks

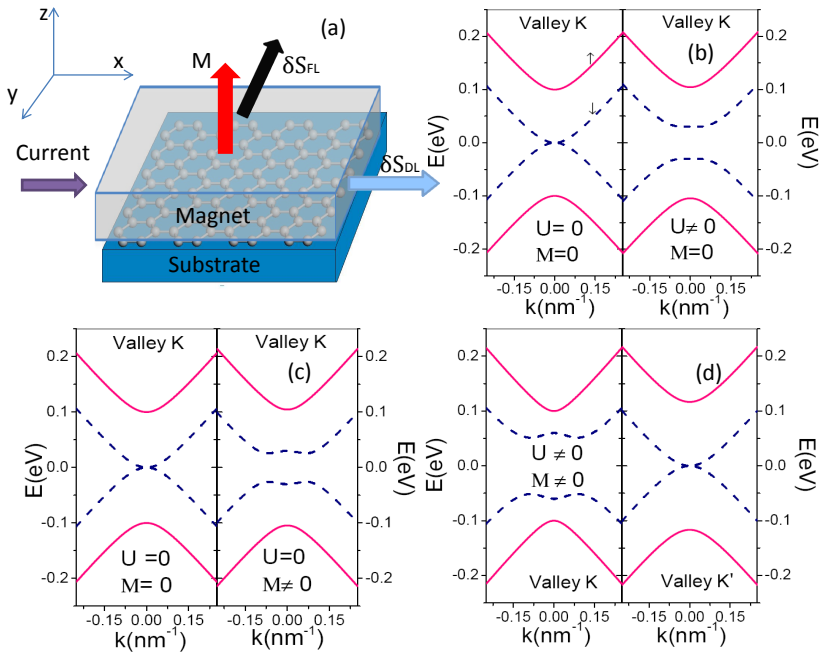

Figure 4.1: (Color online) Schematics of the device based on graphene-like materials with field-like and antidamping-like SOT. (b)-(d) Energy dispersion of graphene-like materials with (b) $U = 0.03\ eV$ (c) $M = 0.03\ eV$ (d) $U = 0.03\ eV$ and $M = 0.03\ eV$. The current flows from left to right. Magnetization is assumed to be directed along the z-axis.

the inversion symmetry and leads to a Rashba spin-orbit coupling. As a results, a transverse nonequilibrium spin density builds up when a current is injected along the horizontal direction. Both Rashba and intrinsic spin-orbit coupling are valley dependent as shown in Eq. (4.2) and thus they can not break the valley degeneracy. In the presence of a magnet, a field-like spin density and an antidamping-like spin density are generated as shown in Fig. 4.1(a) [153, 93]. The exchange field only breaks the time-reversal-symmetry while the sublattice symmetry (two-fold rotational symmetry in the plane) is preserved as shown in Fig. 4.1(c). The interaction between the substrate and graphene-like layer can also induce a staggered potential, which enlarges the band gap without affecting the valley degeneracy, as shown in Fig. 4.1(b).

However, in the presence of both staggered potential and ferromagnetic exchange field, the valley degeneracy is lifted since both the time-reversal and sublattice symme-

tries are broken as shown in Fig. 4.1(d). As a result, SOT becomes valley dependent. Furthermore, as discussed in the next section, the band structure distortion displayed in Figs. 4.1(b)-(d) affects the magnitude of the SOT components.

We adopt a low-energy continuum model Hamiltonian which describes Dirac electrons near to the Fermi energy and captures the physics behind the formation of the valley-dependent SOT in the vicinity of K and K′ points. The total Hamiltonian at K or K′ valley in the basis of $\{\psi_{A,\uparrow}, \psi_{B,\downarrow}, \psi_{B,\uparrow}, \psi_{A,\downarrow}\}$ reads [154]

$$\begin{aligned}\hat{H}_{\rm sys} &= v(\tau k_x\hat{\sigma}_x - k_y\hat{\sigma}_y)\otimes\hat{\rm I} + \frac{\lambda_R}{2}(\tau\hat{\sigma}_x\otimes\hat{s}_y - \hat{\sigma}_y\otimes\hat{s}_x)\\ &+ \tau\lambda_{so}\hat{\sigma}_z\otimes\hat{s}_z + J_{\rm ex}\hat{\rm I}\otimes\mathbf{M}\cdot\hat{\mathbf{s}} + U\hat{\sigma}_z\otimes\hat{\rm I},\end{aligned} \tag{4.2}$$

where $v = \sqrt{3}at/2$ with t being a nearest-neighbor hopping parameter, $\tau = +1(-1)$ stands for the K or (K′) valley, $\hat{\rm I}$ is a $2\times$ 2 unity matrix, a is the lattice constant and $J_{\rm ex}$ is the ferromagnetic coupling constant. $\hat{\boldsymbol{\sigma}}$ and $\hat{\mathbf{s}}$ are Pauli matrices denoting the AB-sublattice and spin degrees of freedom, respectively. $\mathbf{M}$ is the magnetization direction. The first term includes the spin-independent kinetic energy of the particle, the second term denotes the Rashba coupling and the third one represents the intrinsic spin-orbit coupling. The fourth term is the interaction between the spin of the carrier and the local moment of the ferromagnetic system. The last term is the staggered potential (induced by, for instance, an electrical field or a substrate [155, 156, 157]), where $U = 1$ (-1) for A (B) site.

To compute the current-induced effective magnetic field, we first evaluate the nonequilibrium spin density $\delta\mathbf{S}$ at K (K′) valley using Kubo formula in Eq. (2.64) [105], where $\mathbf{E}$ is the electric field, $\hat{\mathbf{v}} = \frac{1}{\hbar}\frac{\partial H}{\partial \mathbf{k}}$ is the velocity operator, $\hat{G}^R_{\mathbf{k}a} = (\hat{G}^A_{\mathbf{k}a})^* = 1/(E_F - E_{\mathbf{k}a} + i\Gamma)$. $\Gamma = \hbar/2\tau$ is the disorder-induced energy spectral broadening due to the finite life time of the particle in the presence of impurities and τ is the momentum scattering time. E_F is the Fermi energy, $E_{\mathbf{k}a}$ is the energy of electrons in

band a. The eigenvector $|\psi_{\mathbf{k},a}\rangle$ in band a can be found by diagonalizing Eq. (4.2). Equation (4.2) contains both intraband ($a = b$) and interband ($a \neq b$) contributions to the nonequilibrium spin density. The former stems from the perturbation of the carrier distribution function by the electric field and it is inversely proportional to Γ. The latter arises from the perturbation of the carrier wave functions by the electric field. The interband contribution also depends on Γ but survives when $\Gamma \to 0$.

In order to evaluate the current-driven SOT in different materials, we define the electrical efficiency of the torque as [74]

$$\eta = \frac{2J_{\mathrm{ex}}\delta S}{\hbar\sigma_{xx}\mathrm{E}} \tag{4.3}$$

where σ_{ij} is conductivity tensor component defined [158]

$$\sigma_{ij} = e^2\hbar\mathrm{Re}\sum_{\mathbf{k},a,b}[\langle\psi_{\mathbf{k}a}|\hat{\mathbf{v}}_i|\ \psi_{\mathbf{k}b}\rangle\langle\psi_{\mathbf{k}b}|\hat{\mathbf{v}}_j|\ \psi_{\mathbf{k}a}\rangle] \times [\hat{G}^R_{\mathbf{k}b}\hat{G}^A_{\mathbf{k}a} - \hat{G}^R_{\mathbf{k}b}\hat{G}^R_{\mathbf{k}a}]. \tag{4.4}$$

At this stage, we wish to point out the limits of the approach outlined above. First, in the presentwork we consider short-range (δ-like) nonmagnetic impurities. We disregard other types of defects such as ripples, magnetic defects, or topological dislocations, which may have a significant impact on transport in graphene. Second, we limit our calculations to the first Born approximation without calculating the vertex corrections. It is well known that vertex corrections are crucial to model spin-orbit coupled transport in systems with high symmetry such as Rashba two-dimensional electron gas. However, while these corrections have been found to exactly cancel the intrinsic spin Hall effect and antidamping torque in the presence of spin-independent impurities, it seems that they are much less dramatic in graphene, only resulting is a renormalization factor of the order of unity. Nonetheless, we also notice that recent calculations by Ado et al. indicate that extending the vertex correction beyond the usual noncrossing diagrams (i.e., including χ and ψ crossing diagrams) produces

non-negligible impurity-independent contributions. Such contributions could indeed be important for the quantities of interest in this work but are left to further studies.

4.3 Inverse spin Galvanic effect

The characteristics of the SOT in two-dimensional hexagonal honeycomb lattices are expected to be different from the well studied case of bulk GaMnAs [74, 75, 95, 96, 115, 130]. Unlike the three-dimensional ferromagnetic GaMnAs in the weak limit ($\lambda_R << J_{\rm ex},\ J_{\rm ex} \sim 1eV$ and $\lambda_{\rm R} \sim 0.1$eV), the graphene-like materials often fall into the strong limit ($\lambda_R >> J_{\rm ex}$), leading to a nonzero interband contribution. The nontrivial Dirac kinetic term (first term in Eq. (4.2)) gives rise to nonlinear transitions of spin density when tuning the Fermi energy. Furthermore, the spin density is more sensitive to band topology tunable by intrinsic spin-orbit coupling or staggered potential. More importantly, the Dirac kinetic term and spin-orbit coupling terms are valley-dependent. In order to better understand the valley-dependent SOT, we first examine spin torque with and without valley degeneracy in section 4.3 and 4.4 respectively.

4.3.1 Non-magnetic honeycomb lattice

We first compute the spin density induced by ISGE in *non-magnetic* graphene. In this material, we choose the following parameters: E_f in [0, 0.3] eV [159], λ_R in [10, 130] meV [147, 148], and $J_{\rm ex}$ in [5, 30] meV [160, 161]. For all the calculations shown in this section, the electrical field is assumed to be along the x-axis and the energy broadening is Γ =0.01 eV. To understand the physical origin of the SOT and establish connections with previous works [130], we parse the SOT into intraband and interband contributions.

Figure 4.2 presents the intraband (a,c) and interband contributions (b,d) to the

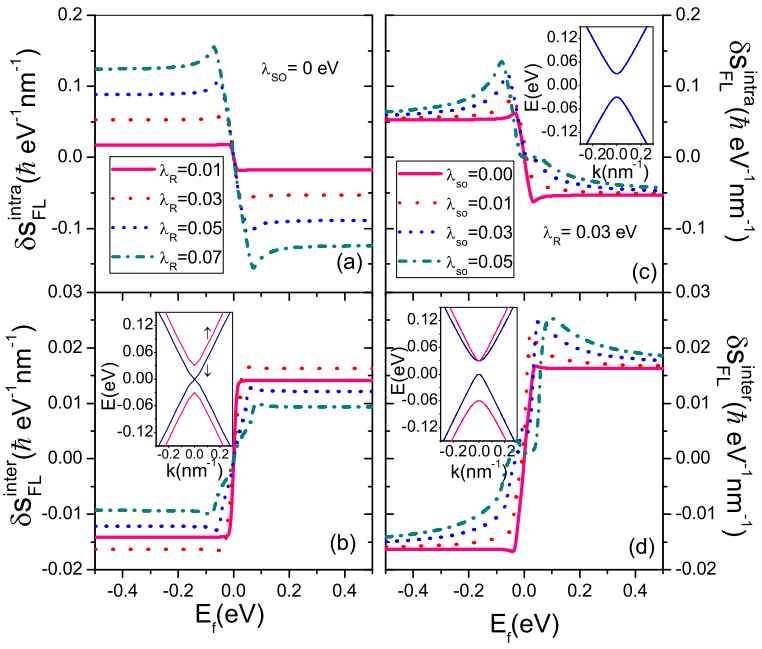

Figure 4.2: (Color online) (a) Intraband and (b) interband contributions to spin density as a function of Fermi energy E_f for various Rashba spin-orbit coupling in the absence of intrinsic spin-orbit coupling λ_{so}. (c) Intraband and (d) interband spin density as a function of Fermi energy E_f for various intrinsic spin-orbit coupling at λ_R=0.03 eV. Inset (b): Band structure of graphene-like materials with λ_R=0.03 eV and λ_{so}=0 eV. Inset (c): Band structure with λ_R=0 eV and λ_{so}=0.03 eV Inset (d): Same as inset (b) but with λ_{so}=0.03 eV. The current is injected along the x axis.

ISGE-driven spin density for various strengths of λ_{R} (a,b) and λ_{so} (c,d). In non-magnetic graphene, intraband contribution produces a spin density aligned toward the y-direction, which is expected from the geometry of our system and consistent with the well known ISGE in two-dimensional electron gases [162, 74]. There is also interband contribution in the strong limit ($\lambda_R >> J_{\mathrm{ex}}$), smaller than the intraband contribution and opposite to it, in agreement with our previous analytical solutions in the case of Rashba two-dimensional electron gas [130]. When increasing the absolute value of Fermi energy, the spin density first experiences a sharp enhancement at small values of E_{f} and quickly saturates. This result is consistent with previous results [163] and can be readily understood by considering the band structure in the inset of Fig. 4.2(b). When the Fermi energy lies in the energy gap of two spin-split subbands, only

one spin species contributes to ISGE and the intraband spin density increases with the Fermi energy. As the Fermi energy lies above the subband gap, the two subbands compensate each other and the spin density saturates. The peaks in Fig. 4.2(a) correspond to the minimum ($E > 0$) or maximum ($E < 0$) of the spin-up subband (see inset of Fig. 4.2(b)) which is of the order of λ_{R}.

Another interesting feature is the spin density as a function of the Rashba spin-orbit coupling. The intraband contribution increases linearly with λ_{R} (see Fig. 4.2(a)), while the interband contribution first increases and then decreases (see Fig. 4.2(b)). The interband contribution depends on the energy difference between the subbands, which itself is of the order of λ_{R}. Indeed, one can show that in the weak impurity limit, the interband contribution is proportional to $1/(\mathrm{E}_{\mathbf{k}\mathrm{a}}\text{-}\mathrm{E}_{\mathbf{k}\mathrm{b}})$ [105, 130, 132]. This results in the non-linear dependence as a function of λ_{R} observed in Fig. 4.2(b) as well as in Fig. 4.3(c).

Rashba spin-orbit coupling is not the only spin-orbit coupling that affects the spin density. In graphene-like systems Rashba spin-orbit coupling is always accompanied by an intrinsic spin-orbit coupling, $\sim \tau\lambda_{so}\hat{\sigma}_z \otimes \hat{s}_z$, which originates from the substrate or a low buckled structure [155, 164]. In Figs. 4.2(c) and (d), we display the Fermi energy dependence of the intraband and interband contributions to spin density for various intrinsic spin-orbit coupling. As expected, the intrinsic spin-orbit coupling opens up a band gap and distorts the topology of the band structure as seen in the inset of Fig. 4.2(c) and (d). For a given K or K′ Valley (ignore τ), this term plays the same role as the ferromagnetic exchange field along the z axis in unit cell when the two sublattices contribute to spin density equivalently (σ_z replaced by $\hat{\mathrm{I}}$). When the two sublattices contribute to spin density inversely, this term acts as an anti-ferromagnetic exchange field and the symmetry of profiles of the spin density is broken and it shifts to the left. Furthermore, the asymmetry of the profiles of the spin density becomes more evident with the increase of λ_{so}. The energy at which the spin

density is maximum equals $\lambda_{so} + \lambda_R$ when $E_f < 0$. Note that the intrinsic spin-orbit coupling does not drive ISGE by itself, but it affects the ISGE-induced spin density driven by Rashba spin-orbit coupling through the modulation of the topology of the bands.

4.3.2 Magnetic honeycomb lattice

Let us now turn to the case of *magnetic* two-dimensional honeycomb lattices. To understand the role of spin-orbit coupling, we plot the intraband and interband spin density as a function of Rashba spin-orbit coupling for different intrinsic spin-orbit coupling in the presence of magnetization in Fig. 4.3. Due to the presence of magnetism, the interband contribution also produces an antidamping component (see Figs. 4.3(c)), i.e. a spin density contribution oriented towards $\sim \mathbf{M}\times\mathbf{y}$ [105, 130, 132] and with a magnitude comparable to the one of the field-like component (see Figs. 4.3(c)). As seen in Figs. 4.3(a)-(c) the interband field-like and antidamping contributions first increase and then decrease. This can be understood as a competition between the spin density driven by Rashba spin-orbit coupling and the suppression of interband scattering due to the distance between the subbands that increases with λ_R.

The intraband contribution decreases with the increasing intrinsic spin-orbit coupling while the interband contribution behaves the opposite way. By opening a band gap, the intrinsic spin-orbit coupling alters the band filling, resulting in a reduced intraband contribution to spin density. An analytical solution of energy depending on intrinsic spin-orbit coupling can be found in previous study [165]. On the other hand, the intrinsic spin-orbit coupling reduces the splitting between the subbands for $E_f > 0$ (see inset in Fig. 4.2(d)), which results in an enhancement of the interband contributions. This result is valuable to current-driven magnetic excitations since the antidamping torque is responsible for magnetization switching and excitations

[153, 93, 166].

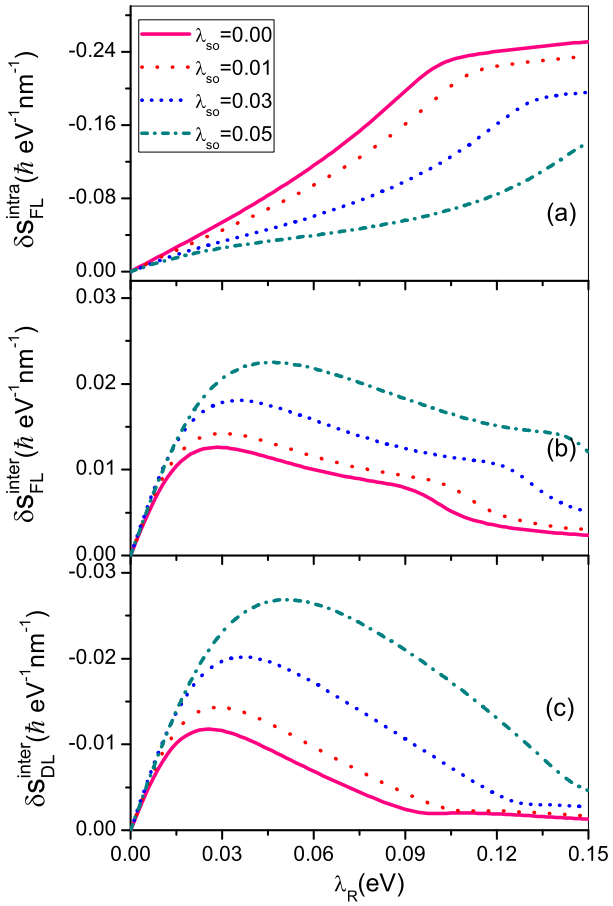

Figure 4.3: (Color online)(a) Intraband and (b)-(c) interband spin density as a function of Rashba spin-orbit coupling for different intrinsic spin-orbit coupling with $J_{\text{ex}} = 0.01\ eV$ and $E_f = 0.1\ eV$. The magnetization is directed along the z axis.

4.4 Valley-Dependent Spin-Orbit Torque

The valley degree of freedom can be used as a tool to enhance the functionality of two-dimensional honeycomb lattices [167]. Recently, a valley-dependent anomalous quantum hall state has been predicted in silicene and silicene nanoribbons owing to the topological phase transition [155, 168]. A charge-neutral Hall effect has been measured in graphene devices [169, 170]. These suggest the emergence of valley Hall

effect. It is thus natural to expect a valley-modulated SOT in our settings.

4.4.1 Staggered Potential

The sublattice degeneracy can be removed by depositing graphene-like materials on hexagonal boron-nitride [169, 171, 172] or silicon carbide [157], or by applying an electrical field in a low buckled structure [155]. When the staggered potential and exchange field are present and the valley degeneracy is broken, the spin density becomes valley-dependent as shown in Figs. 4.4.

In Figs. 4.4(a)-(c), we display the intraband and interband contributions to spin density as a function of Fermi energy in the presence of staggered potential with and without the intrinsic spin-orbit coupling. The imbalance between the contribution of the two valleys to the spin density, i.e., valley polarization, defined as $P = \frac{\delta \mathbf{S}_K - \delta \mathbf{S}_{K'}}{\delta \mathbf{S}_K + \delta \mathbf{S}_{K'}}$, is reported on Figs.4.4(d)-(f). The largest imbalance occurs mainly around the neutrality point $\mathrm{E_F} = 0$. The valley imbalance of the antidamping-like component can reach 100% as shown in Figs.4.4(f), i.e., that for certain energies, this component is dominated by only one valley. When the intrinsic spin-orbit coupling is present, the magnitudes of the valley imbalance can be switched from -100% to 100% by simply tuning the Fermi energy.

4.4.2 Angular dependence

A noticeable effect of lifting the valley degeneracy is its impact on the angular dependence of SOT components. Figure 4.5 displays the angular dependence of the different components of the spin density when the magnetization is rotated in the (x,z) plane. In a ferromagnetic two-dimensional electrons gas with Rashba spin-orbit coupling, the spin density has the general form $\delta \mathbf{S} = \delta S_{\parallel} \cos\theta \mathbf{x} + \delta S_y \mathbf{m} \times \mathbf{y} - \sin\theta \delta S_{\parallel} \mathbf{z}$, where θ is the angle between the magnetization and $\mathbf{z}$. More complex angular dependence may appear in the strong Rashba limit ($\lambda_R >> J_{\mathrm{ex}}$) due to D$'$yakonov-Perel relaxation or

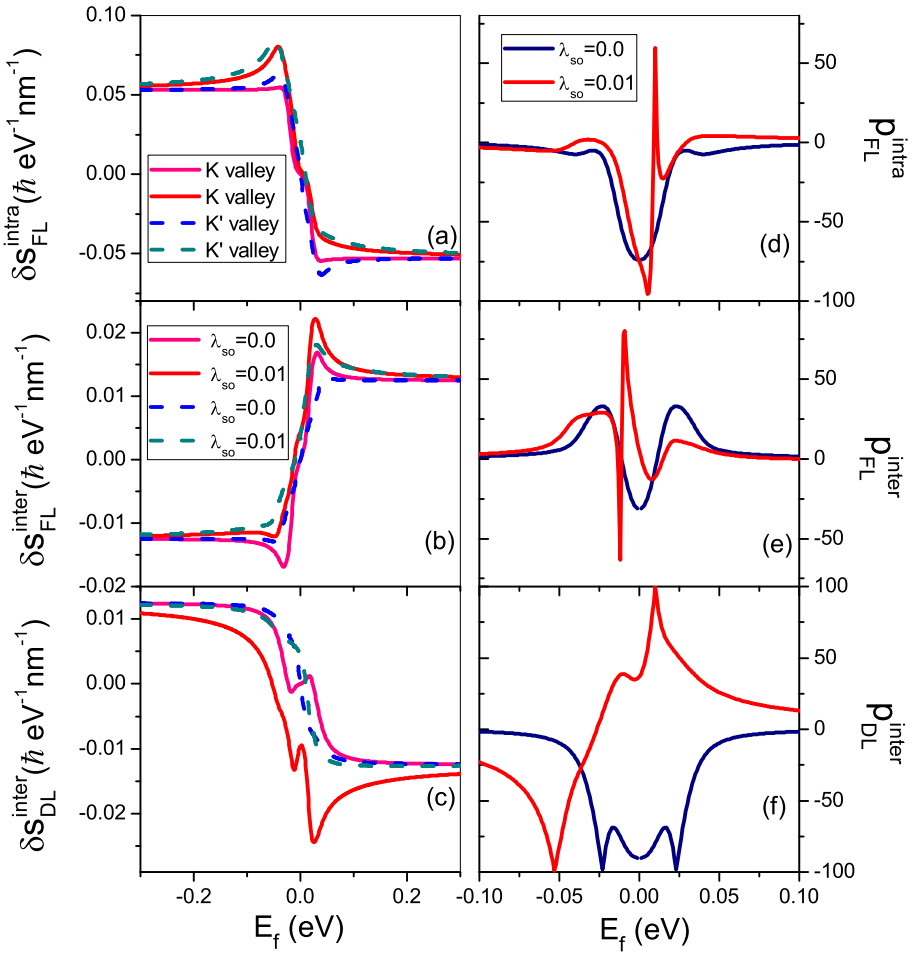

Figure 4.4: (Color online) (a) Intraband and (b)-(c) interband spin density of two valleys as a function of Fermi energy for different intrinsic spin-orbit coupling with $U = 0.01\ eV$ and $J_{\rm ex} = 0.01\ eV$. Valley spin polarization for intraband (d) and interband (e)-(f) components for different intrinsic spin-orbit coupling.

in the intermediate regime ($\lambda_R \sim J_{\rm ex}$) due to a "breathing" Fermi circle [132].

Similarly, in the case of magnetic honeycomb lattices, different components of the spin density display a clear deviation from the simple $\sim \cos\theta$ dependence of the ferromagnetic Rashba gas (see dotted lines in Fig. 4.5). This is attributed to the "breathing" Fermi circle, i.e., the distortion of the Fermi circle, and the modification of the band filling as a function of the direction of the magnetization when the exchange is comparable to the Rashba parameters.

In the absence of valley degeneracy, the angular dependence at K and K' points

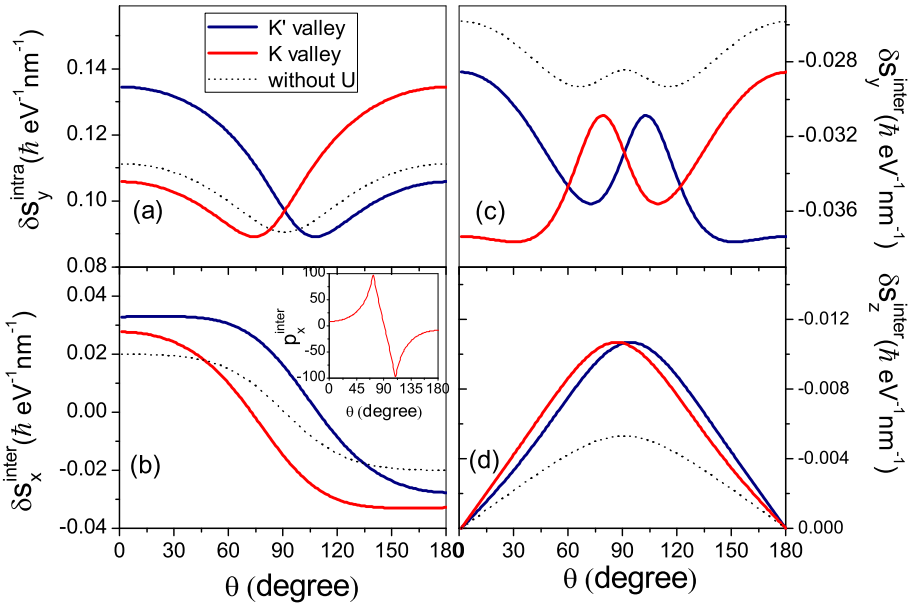

Figure 4.5: (Color online) Intraband and interband spin density as a function of the magnetization direction with (solid lines) and without (dashed lines)staggered potential for the different valleys when U = 0.03 eV. Inset (b) Valley spin polarization of interband spin density for x-component.

differ significantly from each other (red and blue lines in Fig. 4.5, respectively). As a consequence, by tuning the magnetization angle the valley imbalance varies strongly (from -100% to 100% for the x-component, as shown in inset of in Fig. 4.5(b)). We also notice that additional structures are visible in the angular dependence of the field-like component, related to interband transitions (see Fig. 4.5(c)). These features are unique to the case of honeycomb lattices and absent in standard two dimensional free electron gases.

4.5 Connection Between Spin-Orbit Torque and Berry curvature

Berry's phase plays a crucial role in the transport properties of semiconductors especially for graphene-like materials. Due to the inequivalent contribution from two valleys, Berry curvature induces valley hall effect in graphene with broken inversion

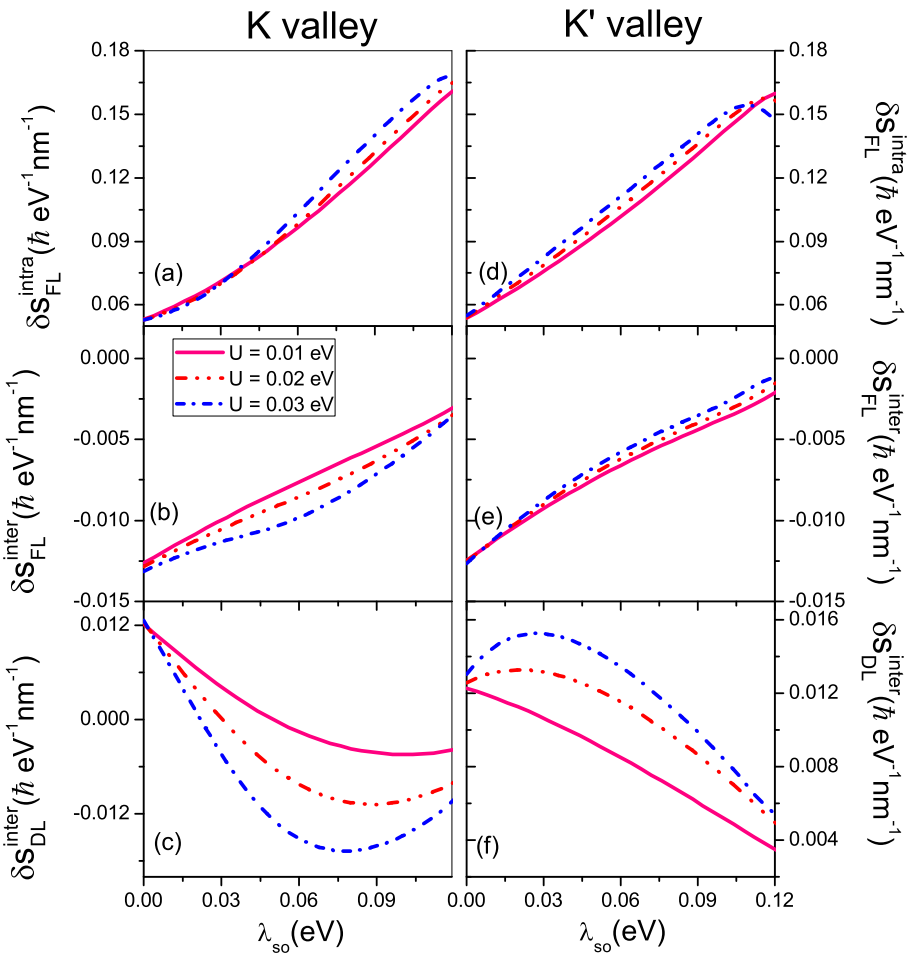

Figure 4.6: (Color online) Intraband and interband spin density as a function of intrinsic spin-orbit coupling for different staggered potential for the K valley (a)-(c) and K′ valley (d)-(f). The parameters are: $E_f = -0.16\ eV$, and $J_{\text{ex}} = 0.01\ eV$ and $\lambda_R = 0.03\ eV$.

symmetry [169]. Recently, the link between SOT and Berry curvature was established in bulk ferromagnetic GaMnAs [105]. The intrinsic spin-orbit coupling distorts the Fermi circle and gives rise to the oscillations in torque magnitudes, as already observed in (Ga,Mn)As [105].

In order to show the connection between the SOT and the band structure distortion, let us analyze the influence of intrinsic spin-orbit coupling on SOT in the presence of a staggered potential. The intraband and interband contributions to spin density as a function of intrinsic spin-orbit coupling for various staggered potential

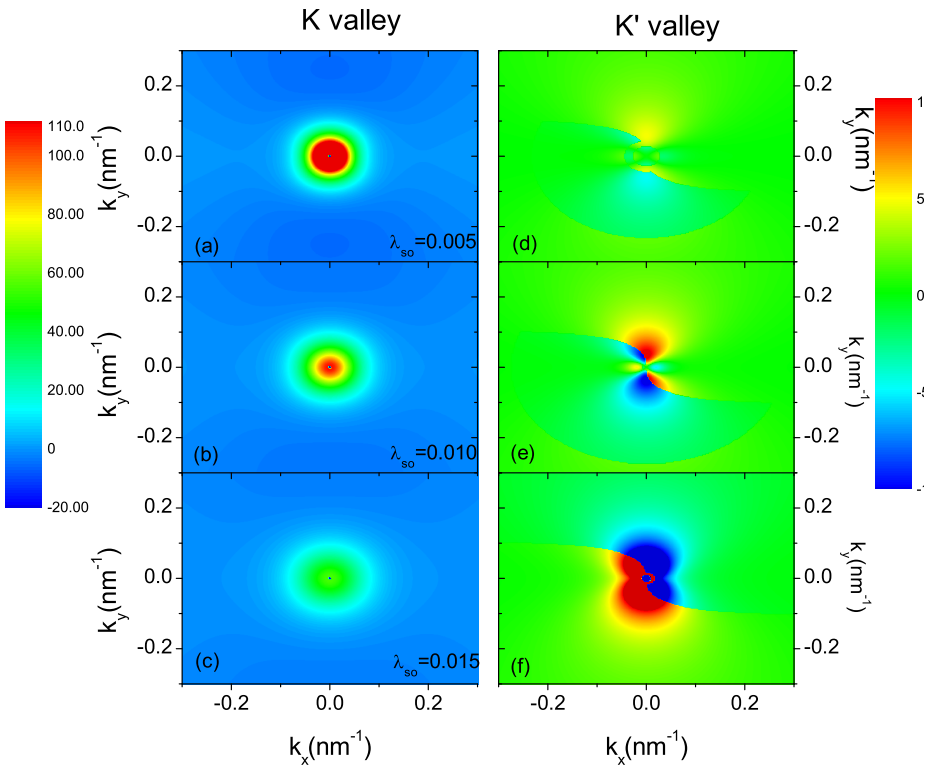

Figure 4.7: (Color online) Contour of valley-polarized Berry curvature distribution for different intrinsic spin-orbit coupling in $k_x - k_y$ plane with U = 0.03 eV. (a) and (d) λ_{so} = 0.005 eV. (b) and (e) λ_{so} = 0.01 eV. (c) and (f) λ_{so} = 0.015 eV. Others parameters are the same as in Fig.4.6.

both at K and K′ valley are displayed in Fig. 4.6. We find that both the field-like intraband and interband contributions to the spin density, $\delta S_{\mathrm{FL}}^{\mathrm{intra}}$ and $\delta S_{\mathrm{FL}}^{\mathrm{inter}}$. They increase with the intrinsic spin-orbit coupling and are only weakly affected by the staggered potential (see Figs. 4.6 (a,b) and (d,e)). In contrast, the antidamping-like component of the spin density, $\delta S_{\mathrm{DL}}^{\mathrm{inter}}$, displays a non-linear dependence as a function of the intrinsic spin-orbit coupling that is very different for the two valleys and highly sensitive to the staggered potential (see Figs. 4.6 (c) and (f)).

To understand this difference, we plot the contour of Berry curvature for different intrinsic spin-orbit coupling at K and K′ valleys in $k_x - k_y$ plane in Fig. 4.7. A large Berry curvature mainly concentrates around the Dirac point and decays away from it, in agreement with previous results [173, 154]. For the K valley, Berry curvature

decreases with the increase of intrinsic spin-orbit coupling. Yet for the K′ valley, Berry curvature increases. This trend is in accordance with the variations of $\delta S_{\mathrm{DL}}^{\mathrm{inter}}$ displayed in Figs. 4.7 (c) and (f) and not in accordance with the variations of $\delta S_{\mathrm{FL}}^{\mathrm{inter}}$ displayed in Figs. 4.7 (b) and (e). It illustrates the fact that while $\delta S_{\mathrm{FL}}^{\mathrm{inter}}$ and $\delta S_{\mathrm{DL}}^{\mathrm{inter}}$ both originate from interband transitions, only the latter is related to Berry curvature, i.e., the field-like SOT is purely due to ISGE instead of the superposition of Berry curvature and ISGE in ferromagnetic GaMnAs as pointed out by Kurebayashi et al. [105].

4.6 Discussion

To complete the present study, we computed the magnitude of antidamping-like and field-like components of the spin density and corresponding electrical efficiencies for various graphene-like honeycomb lattices, assuming $\lambda_R = 0.1\ eV$ and $J_{\mathrm{ex}} = 0.03\ eV$. The results are reported in Table 1, showing that the largest SOT is obtained for stanene ($\sim 100 \times 10^{10}\ eVA^{-1}m^{-1}$). As a comparison, the corresponding efficiencies of field-like SOT in (Ga,Mn)As [130], two-dimensional Rashba systems [74] and topological insulators [174] are of the order of $\sim 1 \times 10^{10}$, $\sim 10 \times 10^{10}$ and $\sim 100 \times 10^{10}\ eVA^{-1}m^{-1}$, respectively, in agreement with the orders of experimental results [77, 79, 153, 175]. Therefore, for moderate Rashba and exchange parameters, honeycomb lattices seem to display large field-like torques. Interestingly, the antidamping-like torque remains about one order of magnitude smaller than the field-like torque, as already observed in two-dimensional Rashba gases and (Ga,Mn)As [130].

Finally, we propose a device to detect the valley-dependent SOT. We consider a multi-terminal device as shown in Fig. 4.8. This is a typical device used to detect charge neutral-currents [169, 170]. The device consists of a graphene-like material

Table 4.1: Efficiency of spin torque for various two dimensional hexagonal lattices

	$\sigma_{xx}(e^2/\hbar)$	s_{DL}	s_{FL}	η_{DL}	η_{FL}
C	23.3809×10^{-3}	0.0083	0.1193	21.3	306
Si	9.0068×10^{-3}	0.0137	0.1975	91.3	1316
Ge	8.4004×10^{-3}	0.0141	0.2019	100.7	1442
Sn	6.5818×10^{-3}	0.0155	0.220	14.13	2006

s_{DL} (s_{FL}) is in unit of $\hbar(eV \cdot nm)^{-1}$ while η_{DL} (η_{FL}) is in unit of $eV(A \cdot nm)^{-1}$.

sandwiched between a magnetic insulator and a non-magnetic substrate such as a topological insulator [149]. The substrate [176] can induce a staggered potential that breaks the valley degeneracy. The voltage is applied to the sidearms and the current flows from the lower sidearm to the upper one. In the absence of magnetization, a valley Hall effect may be detected in the two horizontal terminals [169]. In the presence of magnetization, the torque exerted on the magnetization of the magnetic insulator deposited on top of the left or right terminal will be different.

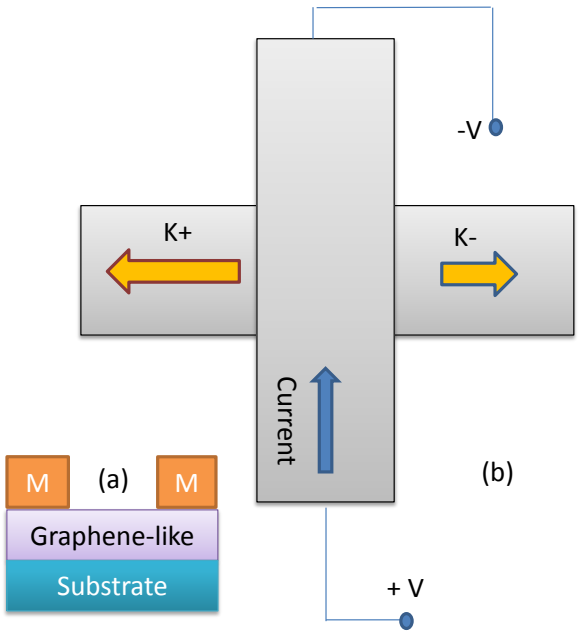

Figure 4.8: Schematics of the realization of valley-dependent antidamping-like SOT: (a) Top view and (b) Side view. The current is injected into the vertical arm. The presence of both magnetization and staggered potential results in a nonequivalent spin density for the valleys. This leads to a different valleys on the horizontal sidearms.

4.7 Conclusion

In summary, we have investigated the nature of SOTs in two dimensional hexagonal crystals and qualitatively recovered most of the results obtained on different systems such as (Ga,Mn)As and two-dimensional Rashba gases [130]. We showed that the staggered potential and intrinsic spin-orbit coupling can strongly affect the magnitude of the torque components as well as their angular dependence. In the presence of staggered potential and exchange field, the valley degeneracy can be lifted and we obtain a valley-dependent antidamping SOT, while the field-like component remains mostly unaffected. This feature is understood in terms of Berry curvature and we show that the valley imbalance can be as high as 100% by tuning the bias voltage or magnetization angle.

Chapter 5

Spin Orbit Torque in One-Dimensional Graphene Nanoribbons

5.1 Introduction

Topological insulators, a new phase of matter, have attracted intense research interest due to their nontrivial physical properties and potential applications in spintronics [177]. Similarly to a conventional or band insulator, it possesses a band gap in the bulk. Yet, differently from a conventional insulator, it has time-reversal-symmetry-protected spin-polarized surface states or edge states in the bulk band gap. These states may experience a transition from a topological insulator to a band insulator (i.e., a topological phase transition) by reasonable structural design and manipulations such as doping with impurities [178, 179], applying to a strain or pressure [180, 181], or interacting with nonmagnetic substrates [182], due to the variations of band topology caused by lattice distortions or spin-orbit coupling. Interestingly, even without the structural manipulations, topological phase transitions can also be

driven by the coupling between topological insulators and magnetic substrates. For example, a transition from a band insulator to a quantum spin Hall insulator can be induced by tuning the exchange coupling between proximity magnetic layers and silicene, which is associated with variations of Berry curvature [183, 168]. Among these studies, the influence of topological phase transitions on Hall conductivities and spin textures in momentum space has been confirmed theoretically and experimentally [184, 179]. From a topological standpoint, a charge or spin current in a topological insulator is also a topological current. Hence, unlike semiconductors and metals, charge conductivities and spin polarized edge states in topological insulators can be controlled not only by an electric field but also by topological phase transitions.

Besides topological phase transitions, charges flowing at the surface or edge of topological insulators are accompanied by a non-equilibrium spin polarization due to the large spin-momentum of surface states [185]. This magneto-electric effect can be used to excite and switch the magnetization of a ferromagnet deposited on the surface, as studied theoretically [186, 187] and demonstrated experimentally [175, 188, 126]. This spin-orbit torque displays a larger electrical efficiency [175, 188, 126] compared with spin torque in bilayers involving heavy metals [153, 93]. Alternatively, the spin-to-charge conversion present at the surface of topological insulators can be probed through charge pumping, i.e. the Onsager reciprocal of spin-orbit torques [189, 190]. In fact, while a charge current creates a torque on the magnetization, a precessing magnetization induces a charge current along the interface. This effect was originally observed in magnetic bilayers involving heavy metals and attributed to the inverse spin Hall effect present in the bulk of the heavy metal [191]. This observation has been recently extended to two dimensional systems such as hexagonal lattices [192], heavy metals [193] and more recently to the surface of topological insulators [194, 195, 193]. In these systems, the spin-charge conversion is attributed to the spin-momentum locking induced by interfacial (Rashba or Dirac) spin-orbit

coupling. While magneto-electric effects have been studied in topological insulators in the metallic regime [186, 187], the influence of topological phase transitions on these mechanisms has been essentially overlooked. In particular, besides the emergence of quantized magneto-electric effect [185], it is not clear how the topologically non-trivial edge states contribute to spin-orbit torque and charge pumping.

In this paper, we theoretically investigate both charge pumping and spin-orbit torque in quasi-one-dimensional zigzag silicene-like nanoribbons with a hexagonal lattice in the presence of intrinsic spin-orbit coupling. Depending on the strength of the spin-orbit coupling this system displays topological phase transitions between trivial (metallic) and non-trivial (quantum spin Hall) phases [156, 183]. Here, we demonstrate that spin-charge conversion efficiency is dramatically enhanced at the topological transition, resulting in large damping-like spin-orbit torque and dc charge pumping.

5.2 Spin-orbit torque and charge pumping

Let us first formulate the reciprocity relationship between spin-orbit torques and charge pumping (see also Ref. [189, 190]). We start from the definition of magnetization dynamics and charge current

$$\begin{aligned} \partial_t \mathbf{m} =& \gamma \mathbf{m} \times \partial_{\mathbf{m}} F + \hat{\chi} \cdot \mathbf{E}, \\ \mathbf{J}_c =& \hat{\sigma} \cdot \mathbf{E} + \hat{\xi} \cdot \partial_{\mathbf{m}} F, \end{aligned} \tag{5.1}$$

where $-\partial_{\mathbf{m}} F = -\partial_{\mathbf{m}} \Omega / M_s$ is the effective field that drives the dynamics of the magnetization in the absence of charge flow. Ω is the magnetic energy density and M_s being the saturation magnetization. $\mathbf{E}$ is the electric field that drives the charge

current through the conductivity tensor $\hat{\sigma}$ is the absence of magnetization dynamics. $\hat{\chi}$ and $\hat{\xi}$ are the tensors accounting for current-driven torques and charge pumping, respectively. We can rewrite these two equations in a more compact form

$$\begin{pmatrix} \partial_t n_i \\ \partial_t m_i \end{pmatrix} = \begin{pmatrix} L_{n_i,f_e^j} & L_{n_i,f_m^j} \\ L_{m_i,f_e^j} & L_{m_i,f_m^j} \end{pmatrix} \begin{pmatrix} f_e^j \\ f_m^j \end{pmatrix} \tag{5.2}$$

where we define the particle current $\partial_t n_i = S\mathrm{J_{c,i}/e}$, the electric and magnetic forces $f_e^j = deE_j$, $f_m^j = \mu_B \partial_{m_j} F$. Onsager coefficients are then

$$\begin{pmatrix} L_{n_i,f_e^j} & L_{n_i,f_m^j} \\ L_{m_i,f_e^j} & L_{m_i,f_m^j} \end{pmatrix} = \begin{pmatrix} W\sigma_{ij}/e^2 & \xi^{ij}/\mu_B \\ \chi^{ij}/d & -(\gamma/\mu_B)(\mathbf{e}_i \times \mathbf{e}_j)\cdot\mathbf{m} \end{pmatrix}. \tag{5.3}$$

Here, we consider a magnetic volume of width W, thickness d and section normal to the current flow $S = Wd$. Applying Onsager reciprocity principle [189, 196]

$$L_{n_i,f_m^j}(\mathbf{m}) = -L_{m_j,f_e^i}(-\mathbf{m}), \tag{5.4}$$

and we obtain $\xi^{ij}(\mathbf{m})/\mu_B = -\chi^{ji}(-\mathbf{m})/d$. In two-dimensional magnets with interfacial inversion asymmetry, the spin-orbit torque $\mathbf{T} = \hat{\chi}\cdot\mathbf{E}$ can be parsed into two components (see e.g. Refs. [187, 130])

$$\mathbf{T} = \tau_{\mathrm{DL}}\mathbf{m}\times((\mathbf{z}\times\mathbf{E})\times\mathbf{m}) + \tau_{\mathrm{FL}}\mathbf{m}\times(\mathbf{z}\times\mathbf{E}), \tag{5.5}$$

referred to as the damping-like (τ_{DL}) and field-like torque (τ_{FL}). Hence, by definition

$$\begin{aligned} \chi^{ij}(\mathbf{m}) =& \tau_{\mathrm{DL}}[\mathbf{m}\times((\mathbf{z}\times\mathbf{e}_j)\times\mathbf{m})]\cdot\mathbf{e}_i \\ &+ \tau_{\mathrm{FL}}[\mathbf{m}\times(\mathbf{z}\times\mathbf{e}_j)]\cdot\mathbf{e}_i. \end{aligned} \tag{5.6}$$

Then, applying Onsager reciprocity, we obtain the charge pumping coefficient

$$\begin{aligned}\xi^{ij}(\mathbf{m}) = &-(\mu_B/d)\tau_{\mathrm{DL}}(-\mathbf{m})[\mathbf{m}\times((\mathbf{z}\times\mathbf{e}_i)\times\mathbf{m})]\cdot\mathbf{e}_j \\ &+(\mu_B/d)\tau_{\mathrm{FL}}(-\mathbf{m})[\mathbf{m}\times(\mathbf{z}\times\mathbf{e}_i)]\cdot\mathbf{e}_j. \end{aligned} \tag{5.7}$$

And finally, the charge current induced by the magnetization dynamics reads

$$\begin{aligned}\mathbf{J}_c = &-\frac{\mu_B}{d\gamma}\tau_{\mathrm{DL}}(-\mathbf{m})\mathbf{z}\times(\mathbf{m}\times\partial_t\mathbf{m}) \\ &+\frac{\mu_B}{d\gamma}\tau_{\mathrm{FL}}(-\mathbf{m})\mathbf{z}\times\partial_t\mathbf{m}. \end{aligned} \tag{5.8}$$

This equation establishes the correspondance between the current-driven spin-orbit torque and the charge current pumped by a time-varying magnetization. In the following, we will compute the current-driven spin density $\delta\mathbf{S}$ from Kubo formula [Eq. (2.64)]. The torque is simply $\mathbf{T} = (2J_{\mathrm{ex}}/\hbar)\mathbf{m}\times\delta\mathbf{S}$, so that that the conclusions drawn for spin-orbit torques equally apply to charge pumping.

5.3 Model and method

Let us now consider a single-layered zigzag nanoribbon with a hexagonal lattice (e.g. silicene, germanene, stanene etc.) deposited on top of a ferromagnetic layer. The ferromagnetic layer may be chosen as EuO [145] or YIG [192, 146], and induces a weak exchange coupling on the spin-polarized carriers as well as Rashba spin-orbit coupling.

In a tight-binding representation, Hamiltonian for silicene-like material can be described by [154]

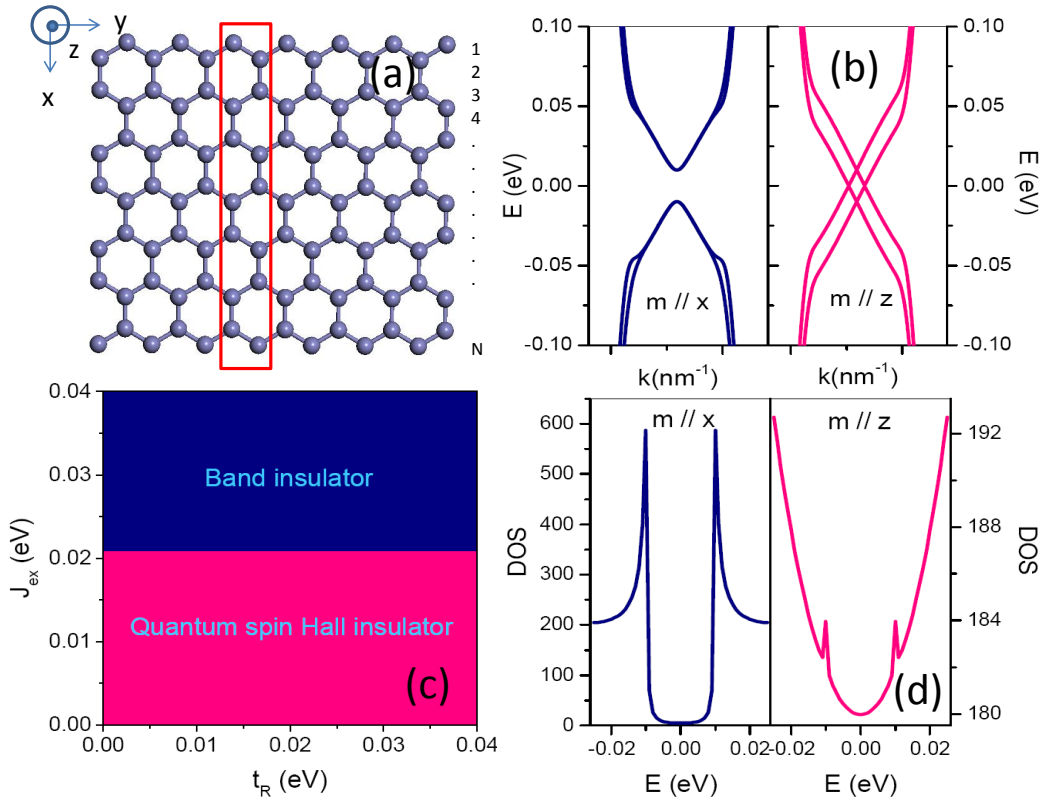

Figure 5.1: (Color online) (a) Top view of zigzag silicene-like nanoribbons switched by a nonmagnetic topological insulator and a magnetic topological insulator. The super unit cell as indicated by the red rectangle. (b) Band structure for different magnetization direction **m**. (c) Phase diagram for various Rashba and magnetization. (d) Density of states for different magnetization direction. The current is directed along the x axis. The parameters are t_{so}= 36 meV and $J_{\rm ex}$= 10 meV.

$$\hat{H}_0 = \sum_{\langle i,j\rangle\alpha} t\hat{c}^+_{i,\alpha}\hat{c}_{j,\alpha} + i\frac{t_{so}}{3\sqrt{3}}\sum_{\langle\langle i,j\rangle\rangle\alpha\beta} c^+_{i,\alpha}v_{ij}\hat{s}^z_{\alpha\beta}c_{j,\beta}$$
$$+i\frac{2t_R}{3}\sum_{\langle i,j\rangle\alpha\beta} c^+_{i,\alpha}\hat{z}\cdot(\hat{\mathbf{s}}_{\alpha\beta}\times\mathbf{d}_{ij})c_{j,\beta} + J_{\rm ex}\sum_{i,\alpha} c^+_{i,\alpha}\hat{\mathbf{s}}\cdot\hat{\mathbf{M}}c_{i,\alpha}. \quad (5.9)$$

where $\hat{c}^+_{i,\alpha}$ ($\hat{c}_{i,\alpha}$) creates (annihilates) an electron with spin α on site i. $\langle i,j\rangle$ ($\langle\langle i,j\rangle\rangle$) runs over all the possible nearest-neighbor (next-nearest-neighbor) hopping sites. t_R (t_{so}) is the Rashba (intrinsic) spin-orbit coupling constant. $v_{ij} = \pm 1$ when the trajectory of electron hopping from the site j to the site i is anti-clockwise (clockwise). $J_{\rm ex}$

is the ferromagnetic coupling constant. The first term denotes the nearest-neighbor hopping, the second term denotes the intrinsic spin-orbit coupling and the third one represents the extrinsic Rashba spin-orbit coupling. The fourth term is the exchange interaction between the spin of the carrier and the local moment of the ferromagnet.

We assume that the nanoribbon is uniform and periodic along the transport direction. A super unit cell is chosen as shown in the red rectangle in Fig. 5.1(a). To compute the spin torques and charge pumping, we first evaluate the nonequilibrium spin density $\delta\mathbf{S}$ using Kubo formula [105] in Eq. (2.64), where $\mathbf{E}$ is the electric field, $\hat{\mathbf{v}} = \frac{1}{\hbar}\frac{\partial H}{\partial \mathbf{k}}$ is the velocity operator, $\hat{G}^R_{\mathbf{k}a} = (\hat{G}^A_{\mathbf{k}a})^* = 1/(E_F - E_{\mathbf{k}a} + i\Gamma)$. Γ is the energy spectral broadening, and V is the unit cell area. E_F is the Fermi energy, $E_{\mathbf{k}a}$ is the energy of electrons in band a. The eigenvector $|\psi_{\mathbf{k},a}\rangle$ in band a can be found by diagonalizing Eq. (5.9). Equation (2.64) contains both intraband ($a = b$) and interband ($a \neq b$) contributions to the nonequilibrium spin density (see the discussion in Ref. [130]). The former is related to impurity scattering and the latter only includes intrinsic contributions related to Berry curvature at $\Gamma = 0$. We ignore the vertex corrections as they only result in a renormalization factor of the order of unity in two dimensional hexagonal lattices [163].

For a nanoribbon in the absence of spin-orbit couping, the eigenvalues and eigenvectors around the Dirac point are independent on the magnetization direction. However, when intrinsic spin-orbit couping is present, it acts as a valley-dependent antiferromagnetic effective field along the z direction. In the low energy limit, it reads $\sim \tau\lambda_{so}\hat{\sigma}_z \otimes \hat{s}_z$. When the magnetization is directed along the x axis, the cooperation of magnetic exchange and Rashba spin-orbit coupling can open up a band gap turning the system into a (trivial) band insulator, as shown in the left panel of Fig. 5.1(b) (see also Ref. [165]). The corresponding density of states in the left panel of Fig. 5.1(d) displays an evident gap. In contrast, when the magnetization is directed along the z axis, the system evolves towards the quantum spin Hall regime (insulating bulk

and conducting spin polarized edges) as shown in the right panel of Fig. 5.1(b). It is related to the fact that the magnetic field couples with the intrinsic spin-orbit coupling and leads to the redistribution of ground states [156]. Unlike the band insulator, the corresponding density of states show a parabolic dependence on energy as shown in the right panel of Fig. 5.1(d). For silicene-like materials, the exchange coupling is about 30 meV [161]. In this parametric range, there are only two different topological phases: trivial band insulator and quantum spin Hall insulator as shown in Fig. 5.1(c). The others topological phases such as quantum anomalous Hall insulator stand beyond this parametric range.

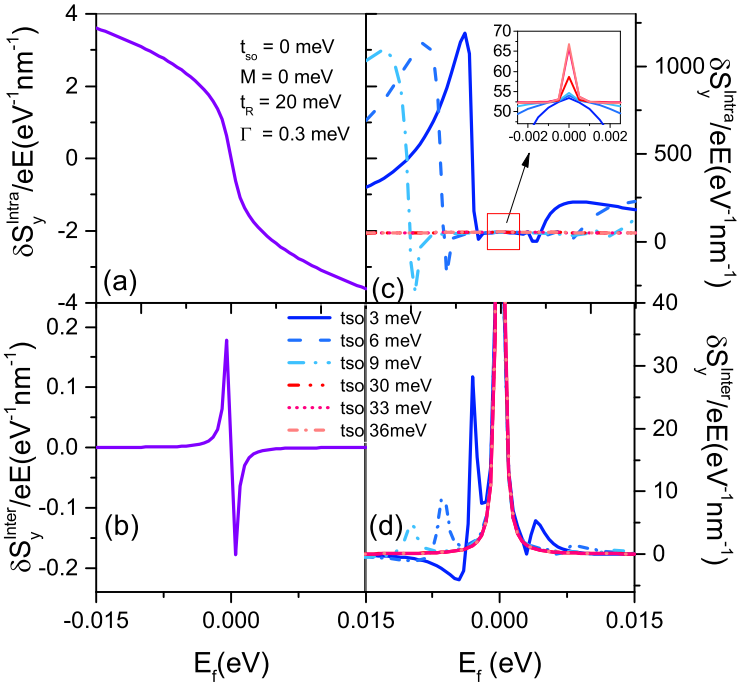

Figure 5.2: (Color online) Intraband and interband components of spin density as a function of Fermi energy in a non-magnetic nanoribbon without (a)-(b) and with intrinsic spin-orbit coupling (c)-(d). The electric field is directed along the x axis.

5.4 Spin-orbit torques

In order to understand the influence of topological phase transition on spin-orbit torque, we first investigate the influence of intrinsic spin-orbit coupling on the nonequilibrium spin density in a non magnetic nanoribbon. In this system, Rashba spin-orbit coupling enables the electrical generation of a non-equilibrium spin density, δS_y, an effect known as the inverse spin galvanic effect and studied in details in bulk two dimensional hexagonal crystals [163]. In Fig. 5.2 we present the intraband (a,c) and interband contributions (b,d) to the non-equilibrium spin density in a nanoribbon as a function of Fermi energy without (a,b) and with (c,d) intrinsic spin-orbit coupling. When the intrinsic spin-orbit coupling is absent [Fig. 5.2(a,b)], the system is metallic and the intraband component dominates the spin density, indicating that carriers at the Fermi surface dominate the transport. The intraband component [Fig. 5.2(a)] is one order of magnitude larger than the interband component [Fig. 5.2(b)], in agreement with the results obtained for two-dimensional graphene-like materials, or two-dimensional electron gases [115, 130]. When the intrinsic spin-orbit coupling is turned on [Fig. 5.2(c,d)], it opens up a bulk band gap and induces spin polarized edge states. In the quantum spin Hall regime (small Fermi energy, no bulk transport), the intraband and interband contributions are of the same order of magnitude, while beyond the quantum spin Hall regime (large Fermi energy, both edge and bulk transport coexist), the intraband contribution dominates the spin density.

Let us now turn our attention towards the case of a magnetic nanoribbon. In our configuration, $\mathbf{E} = E\mathbf{x}$, and the non-equilibrium spin density can be parsed into two components,

$$\delta\mathbf{S} = \delta S_{\mathrm{DL}}\mathbf{y} \times \mathbf{m} + \delta S_{\mathrm{FL}}\mathbf{y}, \tag{5.10}$$

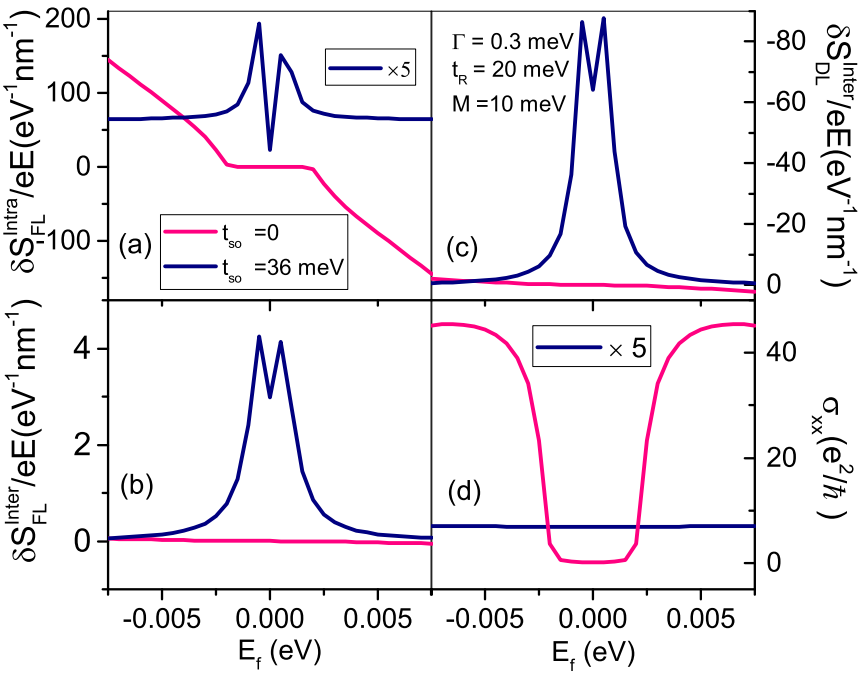

Figure 5.3: (Color online)(a) Intraband, (b)-(c) interband spin density and (d) conductance as a function of Fermi energy without and with intrinsic spin-orbit coupling. The magnetization is directed along the z axis.

referred to as damping-like ($\delta S_{\rm DL}$) and field-like ($\delta S_{\rm FL}$). We plot the field-like and the damping-like spin densities with and without intrinsic spin-orbit coupling in Fig. 5.3. When the intrinsic spin-orbit coupling is absent and the exchange interaction is present, the intraband component dominates the field-like spin density in Fig. 5.3(a) and (b) similar to the case without exchange interaction displayed in Fig. 5.2(a,b). Moreover, the damping-like spin density [Fig. 5.3(b)] is smaller than the field-like spin density [Fig. 5.3(a)] because the former is a correction arising from the precession of non-equilibrium spin density around the magnetization caused by the acceleration of carriers in the electric field [106, 105, 130]. When the intrinsic spin-orbit coupling is turned on, the nanoribbon enters the quantum spin Hall regime: transport only occurs through spin-polarized edge states, resulting in quantized conductance [Fig. 5.3(d)]. The interband and interband field-like spin densities [Fig. 5.3(a,c)] becomes of comparable magnitude but with opposite sign, while the damping-like spin density

is significantly enhanced [Fig. 5.3(b)]. As a result, the damping-like spin density dominates over the field-like spin density. Furthermore, since the conductance is only due to edge states, the overall electrical efficiency of the torque (= torque magnitude / conductance) is dramatically enhanced in the quantum spin Hall regime.

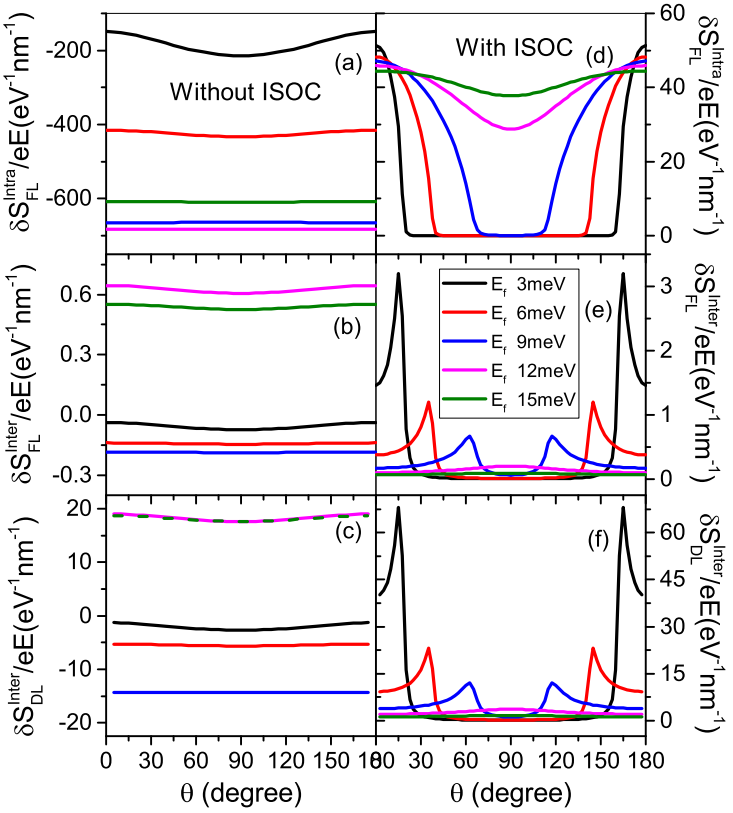

Figure 5.4: (Color online) Intraband and interband spin density as a function of magnetization angle for different Fermi energy. (a)-(c) without intrinsic spin-orbit coupling and (d)-(f) with intrinsic spin-orbit coupling.

The topological phase transition can be induced not only by tuning the intrinsic spin-orbit coupling but also by rotating the magnetization as shown in Fig. 5.1(b,c). In Fig. 5.4, we plot the intraband and interband contributions to spin density as a function of the magnetization angle for different Fermi energies in the absence (a,b,c) or presence (d,e,f) of intrinsic spin-orbit coupling. Dramatic features can be observed depending on whether the nanoribbon experiences a phase transition or not.

When intrinsic spin-orbit coupling is absent [Fig. 5.4(a,b,c)], or when intrinsic

spin-orbit coupling is present and the Fermi energy large enough [$>$ 10 meV in Fig. 5.4(d,e,f)], the nanoribbon remains metallic independently on the magnetization direction. The spin density adopts the form given in Eq. (5.10) and commonly observed in two dimensional Rashba gases [74]. Minor angular dependence is observable due to the small distortion of the Fermi surface (see also Ref. [132]). In contrast, when intrinsic spin-orbit coupling is turned on and the Fermi energy is small enough [$<$ 10 meV in Fig. 5.4(d,e,f)], the nanoribbon experiences a topological phase transition from the metallic ($\theta \approx 0, \pi$) to the quantum spin Hall regime ($\theta \approx \pi/2$). This transition is clearly seen in Fig. 5.4(d), where the intraband field-like spin density decreases dramatically (but does not vanish) upon setting the magnetization away from $\theta \approx 0, \pi$. Correspondingly, the interband damping-like and field-like contributions display an abrupt and dramatic enhancement when the magnetization angle is varied through the topological phase transition.

5.5 Charge pumping

By the virtue of Onsager reciprocity, the results obtained above for the current-driven spin densities apply straightforwardly to the charge pumping. Indeed, from the definition of the torque, we get $\tau_{\mathrm{DL}} = 2J_{\mathrm{ex}}\delta S_{\mathrm{DL}}/E$, and $\tau_{\mathrm{FL}} = 2J_{\mathrm{ex}}\delta S_{\mathrm{FL}}/E$. And henceforth the charge current pumped by a precessing magnetization reads

$$\begin{aligned}\mathbf{J}_c = &- \frac{2J_{\mathrm{ex}}\mu_B}{d\gamma}\frac{\delta S_{\mathrm{DL}}}{E}\mathbf{z}\times(\mathbf{m}\times\partial_t\mathbf{m}) \\ &+ \frac{2J_{\mathrm{ex}}\mu_B}{d\gamma}\frac{\delta S_{\mathrm{FL}}}{E}\mathbf{z}\times\partial_t\mathbf{m}. \end{aligned} \tag{5.11}$$

The first component gives both AC and DC signals [197], while the second term is purely AC. The study of non-equilibrium spin density reported above indicates that the second component $\sim \mathbf{z} \times \partial_t \mathbf{m}$ dominates in the metallic regime (since $\delta S_{\rm FL} > \delta S_{\rm DL}$), while the first component $\sim \mathbf{z} \times (\mathbf{m} \times \partial_t \mathbf{m})$ can be dramatically enhanced in the quantum spin Hall regime ($\delta S_{\rm DL} > \delta S_{\rm FL}$). Furthermore, because changing the magnetization direction can induce topological phase transitions, one can expects that charge pumping with the magnetization lying perpendicular to the two dimensional nanoribbon is much more efficient than with an in-plane magnetization. A large charge pumping efficiency is expected at the topological phase transition.

5.6 Discussion and conclusion

In summary, we have investigated the impact of topological phase transition on the nature of spin-orbit torque and charge pumping in quasi-one dimensional hexagonal nanoribbons. By tuning the magnetization angle or the intrinsic spin-orbit coupling, the system can change from a band insulator to a quantum spin Hall insulator. We find that spin-charge conversion efficiencies (i.e. damping torque and charge pumping) are significantly enhanced in the quantum spin Hall regime.

Recently, a gigantic damping torque has been reported at the surface of topological insulators, with electrical efficiencies about two orders of magnitude larger than in transition metal bilayers [175]. To the best of our knowledge, no theory is currently able to explain such an observation (see discussion in Ref. [187]). Although the present model does not precisely apply to the experimental case, it emphasizes that close or in the quantum spin Hall regime, (i) the electrical efficiency of the spin-orbit torque is dramatically enhanced due to the reduction of the conductance and, most remarkably, (ii) the competition between interband and intraband contributions reduce

the field-like torque, resulting in a dominating damping-like torque. Such an effect, properly adapted to the case of topological insulators, could open interesting perspectives for the smart design of efficient spin-orbit interfaces through the manipulation of topological phase transition.

Chapter 6

Spin Orbit Torque in Two-Dimensional MoS_2

Recent experimental development on spin-charge conversion in two-dimensional transition metal dichalcogenides (TMDs) has motivated us to explore the nature of spin-orbit torque and charge pumping in these materials. In a nutshell, TMDs have a large gap induced by orbital symmetry breaking rather than spin orbit coupling. We also included vertex corrections in this chapter.

6.1 introduction

Recent breakthroughs in nanomaterials synthesis have shed a new light on the physics of intriguing two dimensional materials beyond graphene. These fascinating systems cover materials such as M-Xene [198, 199], black phosphorus [200] or transition metal dichalcogenides [201]. The electronic properties of these materials are now thoroughly investigated in the context of emerging microelectronics [202]. In this short chapter, we turn our attention towards TMDs, as very recent experiments have suggested large spin-charge conversion efficiency in these systems [203]. Recently, a single atom thin MoS_2 have been also prepared successfully [201]. Unlike the graphene, it possesses a direct band gap, and it is more stable than silicene and germanene in air. More

importantly, the monolayer MoS_2 has inversion asymmetry, leading to the potential application of degree of freedom of valley. For each valley, the valence and conduction bands are spin polarized due to the large spin-orbit coupling [204]. Spin polarization in the two valleys are equal in magnitude but opposite in sign due to time-reversal symmetry. In order to exploit MoS_2 and its siblings in valleytronic devices, the key is to generate a non-equilibrium charge carrier imbalance between valleys. An alternative approach is to utilize circularly polarized optical excitation, in which the interband transitions in the vicinity of the K (K$'$) point couple exclusively to right (left)-handed circularly polarized light [205]. Although a more direct way to lift valley degeneracy would be to simply break time-reversal symmetry using an external magnetic field, this effect remains unpractical as a field of 65T would only result in less than 1 meV valley splitting [206]. On the other hand, the exchange coupling between the ferromagnetic layer and the TMD layer, as achieved in Ref [203]. The bilayered structure may induce a Rashba spin orbit coupling and lead to a non-equilibrium spin polarization interacting with the ferromagnetic layer. Their competitive effect, i.e., spin orbit torque, makes it possible to observe valley dependent spin polarization by electric method such as charge pumping or second harmonic Hall voltage. Up till now, the influences of valley polarization on spin torque effects have been scarcely reported.

6.2 Model and Method

We use the low-energy continuum model Hamiltonian that can describe carriers near the Fermi energy in the system. The total Hamiltonian of system at K or K$'$ valley

on the basis of $\{\psi_{HOMO,\uparrow}, \psi_{LUMO,\downarrow}, \psi_{LUMO,\uparrow}, \psi_{HOMO,\downarrow}\}$ reads

$$\hat{H}_{\rm sys} = at(\tau k_x \hat{\sigma}_x + k_y \hat{\sigma}_y) \otimes \hat{\rm I} + \frac{U}{2}\hat{\sigma}_z \otimes \hat{\rm I} + t_{so}\tau \frac{\hat{\sigma}_z - 1}{2} \otimes \hat{s}_z + \frac{t_R}{2}(\tau \hat{\sigma}_x \otimes \hat{s}_y - \hat{\sigma}_y \otimes \hat{s}_x) + J_{\rm ex}\hat{\rm I} \otimes \mathbf{M} \cdot \hat{\mathbf{s}}, \tag{6.1}$$

where t is a nearest-neighbor hopping parameter, $\tau = +1(-1)$ stands for the K (K′) valley , $\hat{\rm I}$ is a 2× 2 unity matrix, a is the lattice constant and $J_{\rm ex}$ is the ferromagnetic coupling constant. $\hat{\boldsymbol{\sigma}}$ and $\hat{\mathbf{s}}$ are Pauli matrices denoting the molecular orbitals (HOMO/LUMO) and spin degrees of freedom, respectively. $\mathbf{M}$ denotes the magnetization direction. U is the staggered potential. t_{so} is the intrinsic spin orbit coupling. t_R is the Rashba spin orbit coupling. The first term includes the spin-independent kinetic energies of the particle, the second term is the energy gap between valence and conduction orbitals (HOMO/LUMO) of Molybdenum. The third one represents the intrinsic spin-orbit coupling stemming from the d orbitals of Molybdenum and s_z is related to the fact that only the in-plane components of the momentum contribute to transport in the two-dimensional materials. The fourth term denotes the Rashba coupling induced by interfacial symmetry breaking. The last term is the interaction between the spin of the carrier and the local moment of the ferromagnetic system.

We calculate the non-equilibrium spin density $\delta\mathbf{S}$ using Kubo formula in Eq. (2.64). Notice that the subbands are based on general spinors in which the HOMO/LUMO and real spin degrees of freedom are included. $\Gamma = \hbar/2\tau$ is the homogeneous energy spectral broadening due to the finite lifetime of the particle in the presence of impurities and τ is a relaxation time. The Bloch state $|\psi_{\mathbf{k}a}\rangle$ in the subband a can be found by diagonalizing Eq. (6.1). This expression contains both intraband ($a = b$) and interband ($a \neq b$) contributions to the nonequilibrium spin density. We further consider the influences of impurity-scattering on the spin density. Assume that the scattering potential is dominated by a point-like random potential

with the Gaussian correlations $\langle V(r)V(r')\rangle = n_i V_0^2 \delta(r-r')$. Correspondingly, Green's function should include the influence of impurity-scattering for the correct evaluation of the contribution to spin density. The self-energy of a single electron reads:

$$\hat{\Sigma}_i^R(E) = n_i V_0^2 \int \frac{d^2\mathbf{k}}{(2\pi)^2} \hat{G}_{\mathbf{k}a}^R(E). \tag{6.2}$$

In the self-consistent Born approximation, only those contributions from non-crossed-disorder-line parts in Feynman diagram are important in the weak scattering limit. Hence, the retarded Green's function is written as:

$$\hat{g}^R = 1/(1/\hat{G}_{\mathbf{k}a}^R - \hat{\Sigma}_i^R(E)). \tag{6.3}$$

The summation over the ladder diagrams can be written as the vertex corrections to the non-equilibrium spin density [207]. The renormalized vertex function related to the spin should satisfy:

$$\hat{\mathbf{S}}_\mathbf{i} = \hat{\mathbf{s}}_i \otimes \hat{\mathrm{I}} + n_i V_0^2 \int \frac{d^2\mathbf{k}}{(2\pi)^2} \hat{g}^A \hat{\mathbf{S}}_\mathbf{i} \hat{g}^R, \tag{6.4}$$

where i = 0, x, y, z. Assuming that $\hat{\mathbf{S}}_\mathbf{i} = a_i \hat{s}_x \otimes \hat{\mathrm{I}} + b_i \hat{s}_y \otimes \hat{\mathrm{I}} + c_i \hat{s}_z \otimes \hat{\mathrm{I}} + d_i \hat{s}_0 \otimes \hat{\mathrm{I}}$, we can find the coefficients a_i,b_i,c_i and d_i. Finally, the spin operators in Eq. (2) should be replaced by new spin-vertex operators. In our calculations, we use the same parameters as in Ref. [173]: $t = 1.1\ eV$, $t_{so} = 0.075\ eV$, $a = 0.319\ nm$ constant and $U = 1.66\ eV$.

6.3 Results

In Fig. 6.1, we first plot the influence of each term in Eq. (1) on the band structure. In these calculation, we progressively turn on and off the various parameters in order

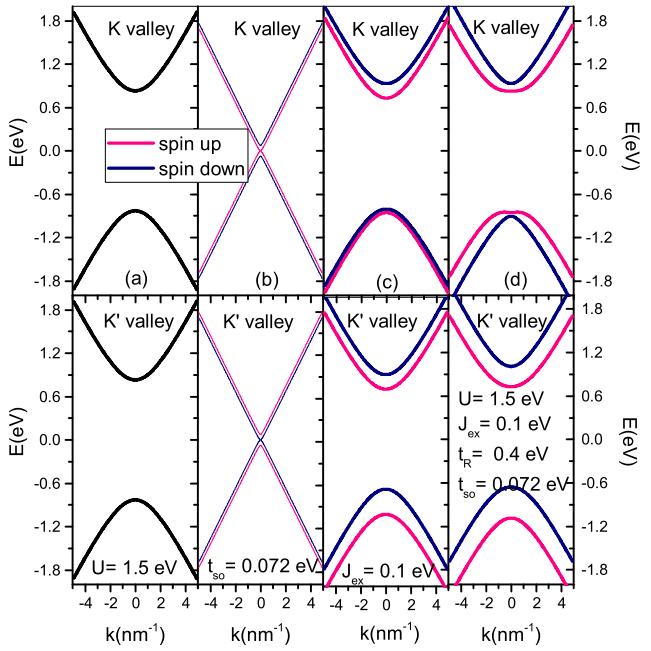

Figure 6.1: Band structure (a) $U = 1.5\ eV$ (b) $t_{so} = 0.072\ eV$ (c) $J_{ex} = 0.1\ eV, t_{so} = 0.072\ eV$ and $U = 1.5\ eV$(d) $J_{ex} = 0.1\ eV, t_{so} = 0.072\ eV, U = 1.5\ eV$ and $t_R = 0.1\ eV$.

to clarify their impact on the band structure. Fig. 6.1(a) displays the band structure in the presence of a staggered potential only ($t_{so} = J_{ex} = t_R = 0$) while Fig. 6.1(b) displays the band structure in the presence of intrinsic spin-orbit coupling only ($U = J_{ex} = t_R = 0$). The staggered potential opens a large orbital gap, while spin-orbit coupling polarizes the bands. Note that this polarization is opposite on the two valleys. In Fig. 6.1(c), staggered potential and intrinsic spin-orbit coupling as well as exchange coupling are all present, but Rashba spin-orbit coupling is turned off. The competition between intrinsic spin-orbit coupling and exchange results in a valley-dependent polarization. Finally, Rashba spin-orbit coupling is turned on in Fig. 6.1(d) and one can observe an additional band splitting that is very clear on K valley but almost undetectable in K' valley. This is due to the fact that the magnetic exchange induces a stronger splitting on the K' valley and therefore dominates over Rashba spin-orbit coupling in this valley.

To further understand the role of intrinsic spin orbit coupling term, we plot the

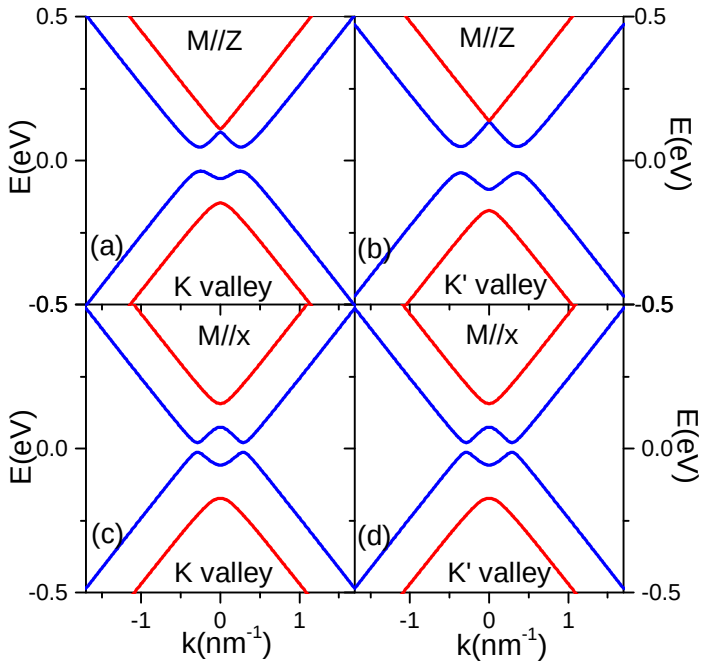

Figure 6.2: Band structure for the different magnetization with $t_R = 0.1\ eV$ and $t_{so} = 0.072\ eV$. (a) and (b) Magnetization is directed along z direction, (c) and (d) Magnetization is directed along x direction.

band structure for different magnetization directions in the presence of magnetic exchange and Rashba spin orbit coupling. The system has two degrees of freedom: spin angular momentum (controlled by magnetization) and molecular orbitals (associated with the intrinsic spin orbit coupling and staggered potential). Along the z direction, these degrees of freedom couple with the valley degrees of freedom. Once the degeneracy of these two degrees of freedom is removed, the valley degeneracy is also broken. For the z direction, the molecular orbitals degeneracy is removed by intrinsic spin orbit coupling. When the magnetization is pointing at the z axis, the spin degeneracy is absent. Hence, there is a large difference in band structure of the valleys. However, the valley does not couple with spin polarization when the magnetization lies along the x direction and the two valleys contribute to same magnitudes band structure but with an opposite spin polarization. As a consequence, there should be a large difference in band structure when the magnetization is directed along z and

the x axis, respectively, as seen in Fig. 6.2. Staggered potential plays the same role as intrinsic spin orbit coupling. Nevertheless, the magnitudes of staggered potential is much larger than intrinsic spin orbit coupling. Hence, the magnetic anisotropy of the system is dominated by the staggered potential.

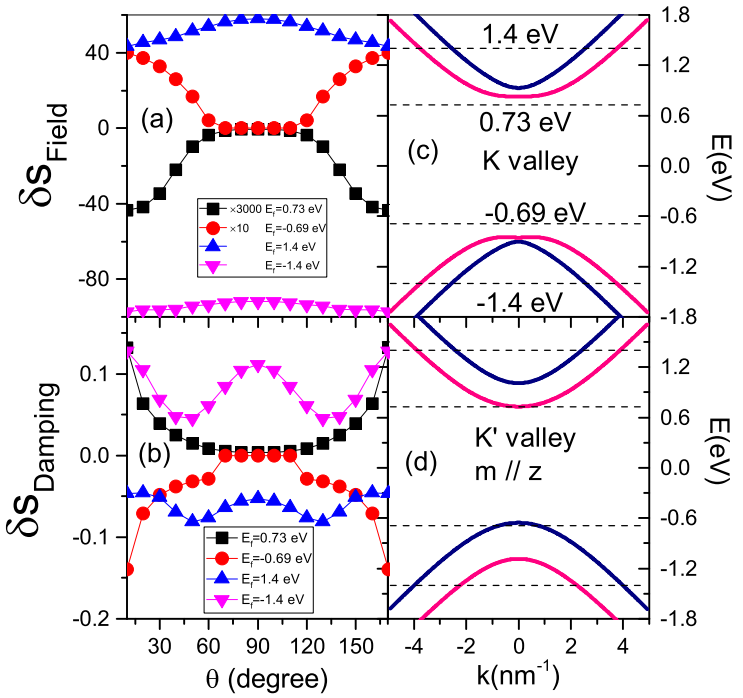

Figure 6.3: (a) Field-like and (b) damping-like spin density as a function of magnetization angle for different Fermi energy. Band structure for K valley (c) and K' valley (d) when $m//z$. The dashed lines in (c) and (d) are the different Fermi energies guide for eyes.

In Fig. 6.3(a) and (b), we plot the spin density of field-like and damping-like components as a function of magnetization for different Fermi energy. We chose two energies close to the gap ($E_f = 0.73\ eV$ for electron transport and $E_f = -0.67\ eV$ for hole transport as indicated by dashed lines in Fig. 6.3(c) and (d)), as well as two energies away from the gap $E_f = 1.4\ eV$ for electron transport and $E_f = -1.4\ eV$ for hole transport). As seen in Fig. 6.3(a) and (b), both the field-like and damping-like components decrease evidently with the increasing magnetization angle at $E_f = 0.73$ or $-0.67\ eV$. Both the magnitudes of field-like and damping-like components are sen-

sitive to the Fermi energy. This is attributed to the variations of valley polarization. As discussed already, the band structures of the two valleys are the same at $\theta = 90$ and different at $\theta = 0$. However, when the Fermi energy lies in the metallic regime ($E_f = 1.4$ or -1.4 eV), the valley asymmetries is not evident as shown in Fig. 6.3(c) and (d). Hence, unlike the case of lower Fermi energy, the field-like and damping like components remain almost a constant.

Chapter 7

Concluding Remarks

In the race of low power operation of electrically driven microelectronic devices, spin-based solutions have attracted increasing interest due to their intrinsic non-volatility. The potential of spintronics for microelectronic applications has been recently illustrated by the release of spin torque magnetic random access memories. In this context, the ability to electrically control magnetic degrees of freedom via spin-orbit coupling offers appealing opportunities in terms of system design. Although the technology is still at its infancy and the eventual exploitation of spin-orbit materials for real-life applications remained to be proven, this thesis intends to contribution to this fascinating field by investigating the nature of spin-orbit torque in various semiconductors using robust quantum transport theory.

We first studied the intraband and interband SOT fields using the Kubo formula, in the prototypical case of a ferromagnetic 2DEG with Rashba spin-orbit coupling, as well as in a three-dimensional DMS modeled by a kinetic-exchange Kohn-Luttinger Hamiltonian. For the latter, parameters pertaining to (Ga,Mn)As were used. In the limit of low doping concentration and weak exchange coupling, we find similarities between the two systems, demonstrating that the general trends of the intrinsic and extrinsic SOT fields can be, in some respect, understood analytically using the Rashba 2DEG in the weak scattering limit. Nevertheless, the numerical analysis of the three-dimensional DMS system also unravels the complex interplay between the

different types of spin-orbit coupling (centrosymmetric and noncentro-symmetric) involved in realistic systems resulting in complex dependencies of the SOT fields on the magnetization direction as well as significant differences from the Rashba 2DEG model. The contribution of interband mixing to the SOT presents an outstanding opportunity to explain the emergence of large anti-damping-like torques that cannot be readily attributed to spin Hall effect, offering an interesting platform to interpret recent puzzling results. The large differences in Hall angle have been detected from metallic system to topological insulator. All these Hall angles are gigantic compared to standard heavy metals, which suggests that additional mechanisms such as the ones discussed in the present work might dominate over the spin Hall effect in these structures.

Second, we have investigated the nature of SOTs in two dimensional hexagonal crystals and qualitatively recovered most of the results obtained on different systems such as (Ga,Mn)As and two-dimensional Rashba gases. We showed that the staggered potential and intrinsic spin-orbit coupling can strongly affect the magnitude of the torque components as well as their angular dependence. In the presence of staggered potential and exchange field, the valley degeneracy can be lifted and we obtain a valley-dependent antidamping SOT, while the field-like component remains mostly unaffected. This feature is understood in terms of Berry curvature and we show that the valley imbalance can be as high as 100% by tuning the bias voltage or magnetization angle.

Third, we study the influence of topological phase transition on spin orbit torque. In quantum spin hall regime, the spin torque component are dominated by quantum spin hall effect instead of inverse galvanic effect. It has a similar character, i.e., the antidamping-like components are larger than the field-like components. The spin torque is sensitive to magnetization switching and lowered evidently when the magnetization is pointed to the in-plane direction. Similar transitions can be found by

tuning the Fermi energy.

We concluded this thesis by investigating the nature of spin-orbit torque in two dimensional transition metal dichalcogenides. These materials resemble graphene in many aspects but present both a very large orbital gap and sizable spin-orbit coupling. Recent experimental data have suggested that the spin-charge conversion efficiency in these materials can be quite large and this motivated us to explore this mechanism from a theoretical perspective. It turns out that the angular dependence of the spin-orbit torque (and therefore the spin-charge conversion) is very sensitive to the Fermi energy of the material. We have been recenlty contacted by experimental collaborators to expand this study and confront our results with their experiments.

REFERENCES

[1] C. Wasshuber, *Computational single-electronics*. Springer Science & Business Media, 2001.

[2] I. Žutić, J. Fabian, and S. D. Sarma, "Spintronics: Fundamentals and applications," *Reviews of modern physics*, vol. 76, no. 2, p. 323, 2004.

[3] M. N. Baibich, J. M. Broto, A. Fert, F. N. Van Dau, F. Petroff, P. Etienne, G. Creuzet, A. Friederich, and J. Chazelas, "Giant magnetoresistance of (001) fe/(001) cr magnetic superlattices," *Physical review letters*, vol. 61, no. 21, p. 2472, 1988.

[4] G. Binasch, P. Grünberg, F. Saurenbach, and W. Zinn, "Enhanced magnetoresistance in layered magnetic structures with antiferromagnetic interlayer exchange," *Physical review B*, vol. 39, no. 7, p. 4828, 1989.

[5] J. Daughton, J. Brown, E. Chen, R. Beech, A. Pohm, and W. Kude, "Magnetic field sensors using gmr multilayer," *Magnetics, IEEE Transactions on*, vol. 30, no. 6, pp. 4608–4610, 1994.

[6] G. A. Prinz, "Magnetoelectronics," *Science*, vol. 282, no. 5394, pp. 1660–1663, 1998.

[7] S. Wolf, D. Awschalom, R. Buhrman, J. Daughton, S. Von Molnar, M. Roukes, A. Y. Chtchelkanova, and D. Treger, "Spintronics: a spin-based electronics vision for the future," *Science*, vol. 294, no. 5546, pp. 1488–1495, 2001.

[8] J. Fabian, A. Matos-Abiague, C. Ertler, P. Stano, and I. Zutic, "Semiconductor spintronics," *Acta Phys. Slov.*, vol. 57, p. 565907, 2007.

[9] T. Jungwirth, J. Sinova, J. Mašek, J. Kučera, and A. MacDonald, "Theory of ferromagnetic (iii, mn) v semiconductors," *Reviews of Modern Physics*, vol. 78, no. 3, p. 809, 2006.

[10] H. Ohno, A. Shen, and F. Matsukura, "(ga, mn) as: a new diluted magnetic semiconductor based on gaas," *Appl. Phys. Lett*, vol. 69, p. 363, 1996.

[11] T. Dietl, H. Ohno, and F. Matsukura, "Hole-mediated ferromagnetism in tetrahedrally coordinated semiconductors," *Physical Review B*, vol. 63, no. 19, p. 195205, 2001.

[12] H. Ohno, D. Chiba, F. Matsukura, T. Omiya, E. Abe, T. Dietl, Y. Ohno, and K. Ohtani, "Electric-field control of ferromagnetism," *Nature*, vol. 408, no. 6815, pp. 944–946, 2000.

[13] D. Chiba, M. Yamanouchi, F. Matsukura, and H. Ohno, "Electrical manipulation of magnetization reversal in a ferromagnetic semiconductor," *Science*, vol. 301, no. 5635, pp. 943–945, 2003.

[14] D. Chiba, M. Sawicki, Y. Nishitani, Y. Nakatani, F. Matsukura, and H. Ohno, "Magnetization vector manipulation by electric fields," *Nature*, vol. 455, no. 7212, pp. 515–518, 2008.

[15] C. Ertler, A. Matos-Abiague, M. Gmitra, M. Turek, and J. Fabian, "Perspectives in spintronics: magnetic resonant tunneling, spin-orbit coupling, and gamnas," in *Journal of Physics: Conference Series*, vol. 129, no. 1. IOP Publishing, 2008, p. 012021.

[16] T. Dietl, H. Ohno, F. Matsukura, J. Cibert, and D. Ferrand, "Zener model description of ferromagnetism in zinc-blende magnetic semiconductors," *Science*, vol. 287, no. 5455, pp. 1019–1022, 2000.

[17] M. Johnson and R. Silsbee, "Calculation of nonlocal baseline resistance in a quasi-one-dimensional wire," *Physical Review B*, vol. 76, no. 15, p. 153107, 2007.

[18] J. Kikkawa and D. Awschalom, "Resonant spin amplification in n-type gaas," *Physical Review Letters*, vol. 80, no. 19, p. 4313, 1998.

[19] H. Zhu, M. Ramsteiner, H. Kostial, M. Wassermeier, H.-P. Schönherr, and K. Ploog, "Room-temperature spin injection from fe into gaas," *Physical Review Letters*, vol. 87, no. 1, p. 016601, 2001.

[20] M. Oestreich, J. Hübner, D. Hägele, P. Klar, W. Heimbrodt, W. Rühle, D. Ashenford, and B. Lunn, "Spin injection into semiconductors," *Applied physics letters*, vol. 74, no. 9, pp. 1251–1253, 1999.

[21] R. Fiederling, M. Keim, G. a. Reuscher, W. Ossau, G. Schmidt, A. Waag, and L. Molenkamp, "Injection and detection of a spin-polarized current in a light-emitting diode," *Nature*, vol. 402, no. 6763, pp. 787–790, 1999.

[22] W. Han, K. Pi, K. McCreary, Y. Li, J. J. Wong, A. Swartz, and R. Kawakami, "Tunneling spin injection into single layer graphene," *Physical review letters*, vol. 105, no. 16, p. 167202, 2010.

[23] R. Jansen, "Silicon spintronics," *Nature Materials*, vol. 11, no. 5, pp. 400–408, 2012.

[24] A. C. Neto, F. Guinea, N. Peres, K. S. Novoselov, and A. K. Geim, "The electronic properties of graphene," *Reviews of modern physics*, vol. 81, no. 1, p. 109, 2009.

[25] A. K. Geim and K. S. Novoselov, "The rise of graphene," *Nature materials*, vol. 6, no. 3, pp. 183–191, 2007.

[26] V. M. Apalkov and T. Chakraborty, "Fractional quantum hall states of dirac electrons in graphene," *Physical review letters*, vol. 97, no. 12, p. 126801, 2006.

[27] K. Novoselov, A. K. Geim, S. Morozov, D. Jiang, M. Katsnelson, I. Grigorieva, S. Dubonos, and A. Firsov, "Two-dimensional gas of massless dirac fermions in graphene," *nature*, vol. 438, no. 7065, pp. 197–200, 2005.

[28] V. V. Cheianov, V. Fal'ko, and B. Altshuler, "The focusing of electron flow and a veselago lens in graphene pn junctions," *Science*, vol. 315, no. 5816, pp. 1252–1255, 2007.

[29] "http://www.futuremarketsinc.com/graphene-market/."

[30] J. Güttinger, F. Molitor, C. Stampfer, S. Schnez, A. Jacobsen, S. Dröscher, T. Ihn, and K. Ensslin, "Transport through graphene quantum dots," *Reports on Progress in Physics*, vol. 75, no. 12, p. 126502, 2012.

[31] K. Wakabayashi, M. Fujita, H. Ajiki, and M. Sigrist, "Electronic and magnetic properties of nanographite ribbons," *Physical Review B*, vol. 59, no. 12, p. 8271, 1999.

[32] Y.-W. Son, M. L. Cohen, and S. G. Louie, "Half-metallic graphene nanoribbons," *Nature*, vol. 444, no. 7117, pp. 347–349, 2006.

[33] G. Z. Magda, X. Jin, I. Hagymási, P. Vancsó, Z. Osváth, P. Nemes-Incze, C. Hwang, L. P. Biró, and L. Tapasztó, "Room-temperature magnetic order on zigzag edges of narrow graphene nanoribbons," *Nature*, vol. 514, no. 7524, pp. 608–611, 2014.

[34] N. Tombros, C. Jozsa, M. Popinciuc, H. T. Jonkman, and B. J. Van Wees, "Electronic spin transport and spin precession in single graphene layers at room temperature," *Nature*, vol. 448, no. 7153, pp. 571–574, 2007.

[35] J. Bai, R. Cheng, F. Xiu, L. Liao, M. Wang, A. Shailos, K. L. Wang, Y. Huang, and X. Duan, "Very large magnetoresistance in graphene nanoribbons," *Nature nanotechnology*, vol. 5, no. 9, pp. 655–659, 2010.

[36] A. Manchon, H. Koo, J. Nitta, S. Frolov, and R. Duine, "New perspectives for rashba spin-orbit coupling," *Nature materials*, vol. 14, no. 9, pp. 871–882, 2015.

[37] C. L. Kane and E. J. Mele, "Quantum spin hall effect in graphene," *Phys. Rev. Lett.*, vol. 95, p. 226801, Nov 2005.

[38] X. Xu, W. Yao, D. Xiao, and T. F. Heinz, "Spin and pseudospins in layered transition metal dichalcogenides," *Nature Physics*, vol. 10, no. 5, pp. 343–350, 2014.

[39] "http://jqi.umd.edu/news/spin-control-modeling-transistor-future."

[40] C. Chappert, A. Fert, and F. N. Van Dau, "The emergence of spin electronics in data storage," *Nature materials*, vol. 6, no. 11, pp. 813–823, 2007.

[41] "http://www2.technologyreview.com/news/412189/tr10-racetrack-memory/."

[42] Y. Kim, X. Fong, K.-W. Kwon, M.-C. Chen, and K. Roy, "Multilevel spin-orbit torque mrams," *Electron Devices, IEEE Transactions on*, vol. 62, no. 2, pp. 561–568, 2015.

[43] Y. Huai, "Spin-transfer torque mram (stt-mram): Challenges and prospects," *AAPPS Bulletin*, vol. 18, no. 6, pp. 33–40, 2008.

[44] J. C. Sankey, Y.-T. Cui, J. Z. Sun, J. C. Slonczewski, R. A. Buhrman, and D. C. Ralph, "Measurement of the spin-transfer-torque vector in magnetic tunnel junctions," *Nature Physics*, vol. 4, no. 1, pp. 67–71, 2008.

[45] N. Locatelli, V. Cros, and J. Grollier, "Spin-torque building blocks," *Nature materials*, vol. 13, no. 1, pp. 11–20, 2014.

[46] M. Stiles and A. Zangwill, "Anatomy of spin-transfer torque," *Physical Review B*, vol. 66, no. 1, p. 014407, 2002.

[47] J. Katine, F. Albert, R. Buhrman, E. Myers, and D. Ralph, "Current-driven magnetization reversal and spin-wave excitations in co/cu/co pillars," *Physical Review Letters*, vol. 84, no. 14, p. 3149, 2000.

[48] D. Chiba, Y. Sato, T. Kita, F. Matsukura, and H. Ohno, "Current-driven magnetization reversal in a ferromagnetic semiconductor (g a, m n) a s/g a a s/(g a, m n) a s tunnel junction," *Physical review letters*, vol. 93, no. 21, p. 216602, 2004.

[49] M. Elsen, H. Jaffrès, R. Mattana, M. Tran, J.-M. George, A. Miard, and A. Lemaître, "Exchange-mediated anisotropy of (ga, mn) as valence-band probed by resonant tunneling spectroscopy," *Physical review letters*, vol. 99, no. 12, p. 127203, 2007.

[50] P. M. Haney and M. Stiles, "Current-induced torques in the presence of spin-orbit coupling," *Physical review letters*, vol. 105, no. 12, p. 126602, 2010.

[51] C.-C. Lin, A. V. Penumatcha, Y. Gao, V. Q. Diep, J. Appenzeller, and Z. Chen, "Spin transfer torque in a graphene lateral spin valve assisted by an external magnetic field," *Nano letters*, vol. 13, no. 11, pp. 5177–5181, 2013.

[52] C.-C. Lin, Y. Gao, A. V. Penumatcha, V. Q. Diep, J. Appenzeller, and Z. Chen, "Improvement of spin transfer torque in asymmetric graphene devices," *ACS nano*, vol. 8, no. 4, pp. 3807–3812, 2014.

[53] K. K. Saha, A. Blom, K. S. Thygesen, and B. K. Nikolić, "Magnetoresistance and negative differential resistance in ni/graphene/ni vertical heterostructures driven by finite bias voltage: A first-principles study," *Physical Review B*, vol. 85, no. 18, p. 184426, 2012.

[54] B. Zhou, X. Chen, H. Wang, K.-H. Ding, and G. Zhou, "Magnetotransport and current-induced spin transfer torque in a ferromagnetically contacted graphene," *Journal of Physics: Condensed Matter*, vol. 22, no. 44, p. 445302, 2010.

[55] T. Yokoyama and J. Linder, "Anomalous magnetic transport in ferromagnetic graphene junctions," *Physical Review B*, vol. 83, no. 8, p. 081418, 2011.

[56] Y. A. Bychkov and E. I. Rashba, "Oscillatory effects and the magnetic susceptibility of carriers in inversion layers," *Journal of physics C: Solid state physics*, vol. 17, no. 33, p. 6039, 1984.

[57] G. Dresselhaus, "Spin-orbit coupling effects in zinc blende structures," *Physical Review*, vol. 100, no. 2, p. 580, 1955.

[58] G. Bir, *Symmetry and strain-induced effects in semiconductors*.

[59] A. Chernyshov, M. Overby, X. Liu, J. K. Furdyna, Y. Lyanda-Geller, and L. P. Rokhinson, "Evidence for reversible control of magnetization in a ferromagnetic material by means of spin–orbit magnetic field," *Nature Physics*, vol. 5, no. 9, pp. 656–659, 2009.

[60] J. Nitta, T. Akazaki, H. Takayanagi, and T. Enoki, "Gate control of spin-orbit interaction in an inverted i n 0.53 g a 0.47 as/i n 0.52 a l 0.48 as heterostructure," *Physical Review Letters*, vol. 78, no. 7, p. 1335, 1997.

[61] A. Manchon and S. Zhang, "Theory of nonequilibrium intrinsic spin torque in a single nanomagnet," *Physical Review B*, vol. 78, no. 21, p. 212405, 2008.

[62] ——, "Theory of spin torque due to spin-orbit coupling," *Physical Review B*, vol. 79, no. 9, p. 094422, 2009.

[63] I. Garate and A. H. MacDonald, "Influence of a transport current on magnetic anisotropy in gyrotropic ferromagnets," *Physical Review B*, vol. 80, no. 13, p. 134403, 2009.

[64] A. Chernyshov, M. Overby, X. Liu, J. K. Furdyna, Y. Lyanda-Geller, and L. P. Rokhinson, "Evidence for reversible control of magnetization in a ferromagnetic material by means of spin–orbit magnetic field," *Nature Physics*, vol. 5, no. 9, pp. 656–659, 2009.

[65] I. Garate and A. H. MacDonald, "Influence of a transport current on magnetic anisotropy in gyrotropic ferromagnets," *Physical Review B*, vol. 80, no. 13, p. 134403, 2009.

[66] K. M. D. Hals, A. Brataas, and Y. Tserkovnyak, "Scattering theory of charge-current–induced magnetization dynamics," *EPL (Europhysics Letters)*, vol. 90, no. 4, p. 47002, 2010.

[67] M. Endo, F. Matsukura, and H. Ohno, "Current induced effective magnetic field and magnetization reversal in uniaxial anisotropy (ga, mn) as," *Applied Physics Letters*, vol. 97, no. 22, p. 2501, 2010.

[68] D. Fang, H. Kurebayashi, J. Wunderlich, K. Vỳbornỳ, L. Zârbo, R. Campion, A. Casiraghi, B. Gallagher, T. Jungwirth, and A. Ferguson, "Spin-orbit-driven ferromagnetic resonance," *Nature nanotechnology*, vol. 6, no. 7, pp. 413–417, 2011.

[69] D. Marchenko, A. Varykhalov, M. Scholz, G. Bihlmayer, E. Rashba, A. Rybkin, A. Shikin, and O. Rader, "Giant rashba splitting in graphene due to hybridization with gold," *Nature communications*, vol. 3, p. 1232, 2012.

[70] M. Zarea and N. Sandler, "Rashba spin-orbit interaction in graphene and zigzag nanoribbons," *Physical Review B*, vol. 79, no. 16, p. 165442, 2009.

[71] J. Katine, F. Albert, R. Buhrman, E. Myers, and D. Ralph, "Current-driven magnetization reversal and spin-wave excitations in co/cu/co pillars," *Physical Review Letters*, vol. 84, no. 14, p. 3149, 2000.

[72] J. C. Slonczewski, "Current-driven excitation of magnetic multilayers," *Journal of Magnetism and Magnetic Materials*, vol. 159, no. 1, pp. L1–L7, 1996.

[73] L. Berger, "Emission of spin waves by a magnetic multilayer traversed by a current," *Physical Review B*, vol. 54, no. 13, p. 9353, 1996.

[74] A. Manchon and S. Zhang, "Theory of nonequilibrium intrinsic spin torque in a single nanomagnet," *Physical Review B*, vol. 78, no. 21, p. 212405, 2008.

[75] I. Garate and A. H. MacDonald, "Influence of a transport current on magnetic anisotropy in gyrotropic ferromagnets," *Physical Review B*, vol. 80, no. 13, p. 134403, 2009.

[76] K. M. D. Hals, A. Brataas, and Y. Tserkovnyak, "Scattering theory of charge-current? induced magnetization dynamics," *EPL (Europhysics Letters)*, vol. 90, no. 4, p. 47002, 2010.

[77] A. Chernyshov, M. Overby, X. Liu, J. K. Furdyna, Y. Lyanda-Geller, and L. P. Rokhinson, "Evidence for reversible control of magnetization in a ferromagnetic material by means of spin–orbit magnetic field," *Nature Physics*, vol. 5, no. 9, pp. 656–659, 2009.

[78] M. Endo, F. Matsukura, and H. Ohno, "Current induced effective magnetic field and magnetization reversal in uniaxial anisotropy (ga, mn) as," *Applied Physics Letters*, vol. 97, no. 22, p. 2501, 2010.

[79] D. Fang, H. Kurebayashi, J. Wunderlich, K. Vỳbornỳ, L. Zârbo, R. Campion, A. Casiraghi, B. Gallagher, T. Jungwirth, and A. Ferguson, "Spin-orbit-driven ferromagnetic resonance," *Nature nanotechnology*, vol. 6, no. 7, pp. 413–417, 2011.

[80] A. Stroppa and G. Kresse, "Unraveling the jahn-teller effect in mn-doped gan using the heyd-scuseria-ernzerhof hybrid functional," *Physical Review B*, vol. 79, no. 20, p. 201201, 2009.

[81] U. Welp, V. Vlasko-Vlasov, X. Liu, J. Furdyna, and T. Wojtowicz, "Magnetic domain structure and magnetic anisotropy in g a 1- x m n x a s," *Physical review letters*, vol. 90, no. 16, p. 167206, 2003.

[82] B. A. Bernevig and S.-C. Zhang, "Spin splitting and spin current in strained bulk semiconductors," *Physical Review B*, vol. 72, no. 11, p. 115204, 2005.

[83] M. Abolfath, T. Jungwirth, J. Brum, and A. MacDonald, "Theory of magnetic anisotropy in iii 1- x mn x v ferromagnets," *Physical Review B*, vol. 63, no. 5, p. 054418, 2001.

[84] T. Jungwirth, M. Abolfath, J. Sinova, J. Kucera, and A. MacDonald, "Boltzmann theory of engineered anisotropic magnetoresistance in (ga, mn) as," *arXiv preprint cond-mat/0206416*, 2002.

[85] J. Van Bree, P. Koenraad, and J. Fernández-Rossier, "Single-exciton spectroscopy of single mn doped inas quantum dots," *Physical Review B*, vol. 78, no. 16, p. 165414, 2008.

[86] A. Rushforth, K. Vỳbornỳ, C. King, K. Edmonds, R. Campion, C. Foxon, J. Wunderlich, A. Irvine, P. Vašek, V. Novák *et al.*, "Anisotropic magnetoresistance components in (ga, mn) as," *Physical review letters*, vol. 99, no. 14, p. 147207, 2007.

[87] H. Ohno, H. Munekata, T. Penney, S. Von Molnar, and L. Chang, "Magnetotransport properties of p-type (in, mn) as diluted magnetic iii-v semiconductors," *Physical Review Letters*, vol. 68, no. 17, p. 2664, 1992.

[88] S. Koshihara, A. Oiwa, M. Hirasawa, S. Katsumoto, Y. Iye, C. Urano, H. Takagi, and H. Munekata, "Ferromagnetic order induced by photogenerated carriers in magnetic iii-v semiconductor heterostructures of (in, mn) as/gasb," *Physical Review Letters*, vol. 78, no. 24, p. 4617, 1997.

[89] T. Jungwirth, Q. Niu, and A. MacDonald, "Anomalous hall effect in ferromagnetic semiconductors," *Physical review letters*, vol. 88, no. 20, p. 207208, 2002.

[90] J. Fabian, A. Matos-Abiague, C. Ertler, P. Stano, and I. Zutic, "Semiconductor spintronics," *Acta Phys. Slov.*, vol. 57, p. 565907, 2007.

[91] H. Ohno, "Properties of ferromagnetic iii–v semiconductors," *Journal of Magnetism and Magnetic Materials*, vol. 200, no. 1, pp. 110–129, 1999.

[92] W. J, "Masters thesis," 202.

[93] L. Liu, C.-F. Pai, Y. Li, H. Tseng, D. Ralph, and R. Buhrman, "Spin-torque switching with the giant spin hall effect of tantalum," *Science*, vol. 336, no. 6081, pp. 555–558, 2012.

[94] P. M. Haney, H.-W. Lee, K.-J. Lee, A. Manchon, and M. Stiles, "Current induced torques and interfacial spin-orbit coupling: Semiclassical modeling," *Physical Review B*, vol. 87, no. 17, p. 174411, 2013.

[95] D. Pesin and A. MacDonald, "Quantum kinetic theory of current-induced torques in rashba ferromagnets," *Physical Review B*, vol. 86, no. 1, p. 014416, 2012.

[96] E. Van der Bijl and R. Duine, "Current-induced torques in textured rashba ferromagnets," *Physical Review B*, vol. 86, no. 9, p. 094406, 2012.

[97] K.-W. Kim, S.-M. Seo, J. Ryu, K.-J. Lee, and H.-W. Lee, "Magnetization dynamics induced by in-plane currents in ultrathin magnetic nanostructures with rashba spin-orbit coupling," *Physical Review B*, vol. 85, no. 18, p. 180404, 2012.

[98] X. Wang and A. Manchon, "Diffusive spin dynamics in ferromagnetic thin films with a rashba interaction," *Physical review letters*, vol. 108, no. 11, p. 117201, 2012.

[99] J. Kim, J. Sinha, M. Hayashi, M. Yamanouchi, S. Fukami, T. Suzuki, S. Mitani, and H. Ohno, "Layer thickness dependence of the current-induced effective field vector in ta— cofeb— mgo," *Nature materials*, vol. 12, no. 3, pp. 240–245, 2013.

[100] K. Garello, I. M. Miron, C. O. Avci, F. Freimuth, Y. Mokrousov, S. Blügel, S. Auffret, O. Boulle, G. Gaudin, and P. Gambardella, "Symmetry and magnitude of spin-orbit torques in ferromagnetic heterostructures," *Nature nanotechnology*, vol. 8, no. 8, pp. 587–593, 2013.

[101] X. Fan, J. Wu, Y. Chen, M. J. Jerry, H. Zhang, and J. Q. Xiao, "Observation of the nonlocal spin-orbital effective field," *Nature communications*, vol. 4, p. 1799, 2013.

[102] M. Jamali, K. Narayanapillai, X. Qiu, L. M. Loong, A. Manchon, and H. Yang, "Spin-orbit torques in co/pd multilayer nanowires," *Physical review letters*, vol. 111, no. 24, p. 246602, 2013.

[103] A. Mellnik, J. Lee, A. Richardella, J. Grab, P. Mintun, M. H. Fischer, A. Vaezi, A. Manchon, E.-A. Kim, N. Samarth *et al.*, "Spin transfer torque generated by the topological insulator bi_2se_3," *arXiv preprint arXiv:1402.1124*, 2014.

[104] P. M. Haney, H.-W. Lee, K.-J. Lee, A. Manchon, and M. Stiles, "Current induced torques and interfacial spin-orbit coupling: Semiclassical modeling," *Physical Review B*, vol. 87, no. 17, p. 174411, 2013.

[105] H. Kurebayashi, J. Sinova, D. Fang, A. Irvine, T. Skinner, J. Wunderlich, V. Novák, R. Campion, B. Gallagher, E. Vehstedt *et al.*, "An antidamping

spin-orbit torque originating from the berry curvature," *Nature nanotechnology*, vol. 9, no. 3, pp. 211–217, 2014.

[106] J. Sinova, D. Culcer, Q. Niu, N. Sinitsyn, T. Jungwirth, and A. MacDonald, "Universal intrinsic spin hall effect," *Physical Review Letters*, vol. 92, no. 12, p. 126603, 2004.

[107] N. Nagaosa, J. Sinova, S. Onoda, A. MacDonald, and N. Ong, "Anomalous hall effect," *Reviews of modern physics*, vol. 82, no. 2, p. 1539, 2010.

[108] K. Obata and G. Tatara, "Current-induced domain wall motion in rashba spin-orbit system," *Physical Review B*, vol. 77, no. 21, p. 214429, 2008.

[109] S. Onoda, N. Sugimoto, and N. Nagaosa, "Intrinsic versus extrinsic anomalous hall effect in ferromagnets," *Physical review letters*, vol. 97, no. 12, p. 126602, 2006.

[110] J. Luttinger, "Quantum theory of cyclotron resonance in semiconductors: General theory," *Physical Review*, vol. 102, no. 4, p. 1030, 1956.

[111] G. Dresselhaus, "Spin-orbit coupling effects in zinc blende structures," *Physical Review*, vol. 100, no. 2, p. 580, 1955.

[112] M. Kopeckỳ, J. Kub, F. Máca, J. Mašek, O. Pacherová, A. Rushforth, B. Gallagher, R. Campion, V. Novák, and T. Jungwirth, "Detection of stacking faults breaking the [110]/[1 1^{-} 0] symmetry in ferromagnetic semiconductors (ga, mn) as and (ga, mn)(as, p)," *Physical Review B*, vol. 83, no. 23, p. 235324, 2011.

[113] J. Zemen, J. Kučera, K. Olejník, and T. Jungwirth, "Magnetocrystalline anisotropies in (ga, mn) as: Systematic theoretical study and comparison with experiment," *Physical Review B*, vol. 80, no. 15, p. 155203, 2009.

[114] B. A. Bernevig and O. Vafek, "Piezo-magnetoelectric effects in p-doped semiconductors," *Physical Review B*, vol. 72, no. 3, p. 033203, 2005.

[115] H. Li, X. Wang, F. Doan, and A. Manchon, "Tailoring spin-orbit torque in diluted magnetic semiconductors," *Applied Physics Letters*, vol. 102, no. 19, p. 192411, 2013.

[116] P. M. Haney and M. Stiles, "Current-induced torques in the presence of spin-orbit coupling," *Physical review letters*, vol. 105, no. 12, p. 126602, 2010.

[117] E. Ivchenko and G. Pikus, "New photogalvanic effect in gyrotropic crystals," *JETP Lett*, vol. 27, no. 11, pp. 604–608, 1978.

[118] M. I. Dyakonov, *Spin physics in semiconductors*. Springer Science & Business Media, 2008, vol. 157.

[119] A. Y. Silov, P. Blajnov, J. Wolter, R. Hey, K. Ploog, and N. Averkiev, "Current-induced spin polarization at a single heterojunction," *Applied physics letters*, vol. 85, no. 24, pp. 5929–5931, 2004.

[120] S. Ganichev, S. Danilov, P. Schneider, V. Belkov, L. E. Golub, W. Wegscheider, D. Weiss, and W. Prettl, "Electric current-induced spin orientation in quantum well structures," *Journal of magnetism and magnetic materials*, vol. 300, no. 1, pp. 127–131, 2006.

[121] A. Manchon and S. Zhang, "Theory of nonequilibrium intrinsic spin torque in a single nanomagnet," *Physical Review B*, vol. 78, no. 21, p. 212405, 2008.

[122] M. Endo, F. Matsukura, and H. Ohno, "Current induced effective magnetic field and magnetization reversal in uniaxial anisotropy (ga,mn) as," *Applied Physics Letters*, vol. 97, no. 22, p. 2501, 2010.

[123] D. Fang, H. Kurebayashi, J. Wunderlich, K. Vỳbornỳ, L. Zârbo, R. Campion, A. Casiraghi, B. Gallagher, T. Jungwirth, and A. Ferguson, "Spin-orbit-driven ferromagnetic resonance," *Nature nanotechnology*, vol. 6, no. 7, pp. 413–417, 2011.

[124] I. M. Miron, G. Gaudin, S. Auffret, B. Rodmacq, A. Schuhl, S. Pizzini, J. Vogel, and P. Gambardella, "Current-driven spin torque induced by the rashba effect

in a ferromagnetic metal layer," *Nature materials*, vol. 9, no. 3, pp. 230–234, 2010.

[125] J. Kim, J. Sinha, M. Hayashi, M. Yamanouchi, S. Fukami, T. Suzuki, S. Mitani, and H. Ohno, "Layer thickness dependence of the current-induced effective field vector in ta— cofeb— mgo," *Nature materials*, vol. 12, no. 3, pp. 240–245, 2013.

[126] A. Mellnik, J. Lee, A. Richardella, J. Grab, P. Mintun, M. Fischer, A. Vaezi, A. Manchon, E.-A. Kim, N. Samarth *et al.*, "Spin-transfer torque generated by a topological insulator," *Nature*, vol. 511, no. 7510, pp. 449–451, 2014.

[127] X. Fan, J. Wu, Y. Chen, M. J. Jerry, H. Zhang, and J. Q. Xiao, "Observation of the nonlocal spin-orbital effective field," *Nature communications*, vol. 4, p. 1799, 2013.

[128] L. Liu, O. Lee, T. Gudmundsen, D. Ralph, and R. Buhrman, "Current-induced switching of perpendicularly magnetized magnetic layers using spin torque from the spin hall effect," *Physical review letters*, vol. 109, no. 9, p. 096602, 2012.

[129] A. Brataas, A. D. Kent, and H. Ohno, "Current-induced torques in magnetic materials," *Nature materials*, vol. 11, no. 5, pp. 372–381, 2012.

[130] H. Li, H. Gao, L. P. Zârbo, K. Vỳbornỳ, X. Wang, I. Garate, F. Doan, A. Čejchan, J. Sinova, T. Jungwirth *et al.*, "Intraband and interband spin-orbit torques in noncentrosymmetric ferromagnets," *Physical Review B*, vol. 91, no. 13, p. 134402, 2015.

[131] X. Wang and A. Manchon, "Diffusive spin dynamics in ferromagnetic thin films with a rashba interaction," *Physical review letters*, vol. 108, no. 11, p. 117201, 2012.

[132] K.-S. Lee, D. Go, A. Manchon, P. M. Haney, M. Stiles, H.-W. Lee, and K.-J. Lee, "Angular dependence of spin-orbit spin-transfer torques," *Physical Review B*, vol. 91, no. 14, p. 144401, 2015.

[133] H. Kurebayashi, J. Sinova, D. Fang, A. Irvine, T. Skinner, J. Wunderlich, V. Novák, R. Campion, B. Gallagher, E. Vehstedt *et al.*, "An antidamping

spin-orbit torque originating from the berry curvature," *Nature nanotechnology*, vol. 9, no. 3, pp. 211–217, 2014.

[134] K.-S. Lee, D. Go, A. Manchon, P. M. Haney, M. Stiles, H.-W. Lee, and K.-J. Lee, "Angular dependence of spin-orbit spin-transfer torques," *Physical Review B*, vol. 91, no. 14, p. 144401, 2015.

[135] A. Varykhalov, J. Sánchez-Barriga, A. Shikin, C. Biswas, E. Vescovo, A. Rybkin, D. Marchenko, and O. Rader, "Electronic and magnetic properties of quasifreestanding graphene on ni," *Physical review letters*, vol. 101, no. 15, p. 157601, 2008.

[136] D. Marchenko, A. Varykhalov, M. Scholz, G. Bihlmayer, E. Rashba, A. Rybkin, A. Shikin, and O. Rader, "Giant rashba splitting in graphene due to hybridization with gold," *Nature communications*, vol. 3, p. 1232, 2012.

[137] A. G. Swartz, P. M. Odenthal, Y. Hao, R. S. Ruoff, and R. K. Kawakami, "Integration of the ferromagnetic insulator euo onto graphene," *ACS nano*, vol. 6, no. 11, pp. 10 063–10 069, 2012.

[138] J. Klinkhammer, M. Schlipf, F. Craes, S. Runte, T. Michely, and C. Busse, "Spin-polarized surface state in euo (100)," *Physical review letters*, vol. 112, no. 1, p. 016803, 2014.

[139] J. Klinkhammer, D. F. Förster, S. Schumacher, H. P. Oepen, T. Michely, and C. Busse, "Structure and magnetic properties of ultra thin textured euo films on graphene," *Applied Physics Letters*, vol. 103, no. 13, p. 131601, 2013.

[140] A. Fleurence, R. Friedlein, T. Ozaki, H. Kawai, Y. Wang, and Y. Yamada-Takamura, "Experimental evidence for epitaxial silicene on diboride thin films," *Physical review letters*, vol. 108, no. 24, p. 245501, 2012.

[141] P. Vogt, P. De Padova, C. Quaresima, J. Avila, E. Frantzeskakis, M. C. Asensio, A. Resta, B. Ealet, and G. Le Lay, "Silicene: compelling experimental evidence for graphenelike two-dimensional silicon," *Physical review letters*, vol. 108, no. 15, p. 155501, 2012.

[142] L. Li, S.-z. Lu, J. Pan, Z. Qin, Y.-q. Wang, Y. Wang, G.-y. Cao, S. Du, and H.-J. Gao, "Buckled germanene formation on pt (111)," *Advanced Materials*, vol. 26, no. 28, pp. 4820–4824, 2014.

[143] Y. Xu, B. Yan, H.-J. Zhang, J. Wang, G. Xu, P. Tang, W. Duan, and S.-C. Zhang, "Large-gap quantum spin hall insulators in tin films," *Physical review letters*, vol. 111, no. 13, p. 136804, 2013.

[144] W. Han, R. K. Kawakami, M. Gmitra, and J. Fabian, "Graphene spintronics," *Nature nanotechnology*, vol. 9, no. 10, pp. 794–807, 2014.

[145] A. G. Swartz, P. M. Odenthal, Y. Hao, R. S. Ruoff, and R. K. Kawakami, "Integration of the ferromagnetic insulator euo onto graphene," *ACS nano*, vol. 6, no. 11, pp. 10 063–10 069, 2012.

[146] Z. Wang, C. Tang, R. Sachs, Y. Barlas, and J. Shi, "Proximity-induced ferromagnetism in graphene revealed by the anomalous hall effect," *Physical review letters*, vol. 114, no. 1, p. 016603, 2015.

[147] D. Marchenko, A. Varykhalov, M. Scholz, G. Bihlmayer, E. Rashba, A. Rybkin, A. Shikin, and O. Rader, "Giant rashba splitting in graphene due to hybridization with gold," *Nature communications*, vol. 3, p. 1232, 2012.

[148] P. Leicht, J. Tesch, S. Bouvron, F. Blumenschein, P. Erler, L. Gragnaniello, and M. Fonin, "Rashba splitting of graphene-covered au (111) revealed by quasiparticle interference mapping," *Physical Review B*, vol. 90, no. 24, p. 241406, 2014.

[149] K.-H. Jin and S.-H. Jhi, "Proximity-induced giant spin-orbit interaction in epitaxial graphene on a topological insulator," *Physical Review B*, vol. 87, no. 7, p. 075442, 2013.

[150] C.-Z. Chang, J. Zhang, X. Feng, J. Shen, Z. Zhang, M. Guo, K. Li, Y. Ou, P. Wei, L.-L. Wang *et al.*, "Experimental observation of the quantum anomalous hall effect in a magnetic topological insulator," *Science*, vol. 340, no. 6129, pp. 167–170, 2013.

[151] Y. Zou and Y. Wang, "Nio nanosheets grown on graphene nanosheets as superior anode materials for li-ion batteries," *Nanoscale*, vol. 3, no. 6, pp. 2615–2620, 2011.

[152] Z. Qiao, W. Ren, H. Chen, L. Bellaiche, Z. Zhang, A. MacDonald, and Q. Niu, "Quantum anomalous hall effect in graphene proximity coupled to an antiferromagnetic insulator," *Physical review letters*, vol. 112, no. 11, p. 116404, 2014.

[153] I. M. Miron, K. Garello, G. Gaudin, P.-J. Zermatten, M. V. Costache, S. Auffret, S. Bandiera, B. Rodmacq, A. Schuhl, and P. Gambardella, "Perpendicular switching of a single ferromagnetic layer induced by in-plane current injection," *Nature*, vol. 476, no. 7359, pp. 189–193, 2011.

[154] Z. Qiao, S. A. Yang, W. Feng, W.-K. Tse, J. Ding, Y. Yao, J. Wang, and Q. Niu, "Quantum anomalous hall effect in graphene from rashba and exchange effects," *Physical Review B*, vol. 82, no. 16, p. 161414, 2010.

[155] M. Ezawa, "Valley-polarized metals and quantum anomalous hall effect in silicene," *Physical review letters*, vol. 109, no. 5, p. 055502, 2012.

[156] C. L. Kane and E. J. Mele, "Quantum spin hall effect in graphene," *Physical review letters*, vol. 95, no. 22, p. 226801, 2005.

[157] S. Zhou, G.-H. Gweon, A. Fedorov, P. First, W. De Heer, D.-H. Lee, F. Guinea, A. C. Neto, and A. Lanzara, "Substrate-induced bandgap opening in epitaxial graphene," *Nature materials*, vol. 6, no. 10, pp. 770–775, 2007.

[158] Y. Murayama, "Junctions," *Mesoscopic Systems: Fundamentals and Applications*, pp. 39–49, 2001.

[159] D. Pesin and A. H. MacDonald, "Spintronics and pseudospintronics in graphene and topological insulators," *Nature materials*, vol. 11, no. 5, pp. 409–416, 2012.

[160] H. Haugen, D. Huertas-Hernando, and A. Brataas, "Spin transport in proximity-induced ferromagnetic graphene," *Physical Review B*, vol. 77, no. 11, p. 115406, 2008.

[161] H.-X. Yang, A. Hallal, D. Terrade, X. Waintal, S. Roche, and M. Chshiev, "Proximity effects induced in graphene by magnetic insulators: First-principles calculations on spin filtering and exchange-splitting gaps," *Physical review letters*, vol. 110, no. 4, p. 046603, 2013.

[162] V. M. Edelstein, "Spin polarization of conduction electrons induced by electric current in two-dimensional asymmetric electron systems," *Solid State Communications*, vol. 73, no. 3, pp. 233–235, 1990.

[163] A. Dyrdał, J. Barnaś, and V. Dugaev, "Current-induced spin polarization in graphene due to rashba spin-orbit interaction," *Physical Review B*, vol. 89, no. 7, p. 075422, 2014.

[164] C.-C. Liu, H. Jiang, and Y. Yao, "Low-energy effective hamiltonian involving spin-orbit coupling in silicene and two-dimensional germanium and tin," *Physical Review B*, vol. 84, no. 19, p. 195430, 2011.

[165] Z. Qiao, H. Jiang, X. Li, Y. Yao, and Q. Niu, "Microscopic theory of quantum anomalous hall effect in graphene," *Physical Review B*, vol. 85, no. 11, p. 115439, 2012.

[166] V. E. Demidov, S. Urazhdin, H. Ulrichs, V. Tiberkevich, A. Slavin, D. Baither, G. Schmitz, and S. O. Demokritov, "Magnetic nano-oscillator driven by pure spin current," *Nature materials*, vol. 11, no. 12, pp. 1028–1031, 2012.

[167] A. Rycerz, J. Tworzydło, and C. Beenakker, "Valley filter and valley valve in graphene," *Nature Physics*, vol. 3, no. 3, pp. 172–175, 2007.

[168] H. Pan, Z. Li, C.-C. Liu, G. Zhu, Z. Qiao, and Y. Yao, "Valley-polarized quantum anomalous hall effect in silicene," *Physical review letters*, vol. 112, no. 10, p. 106802, 2014.

[169] R. Gorbachev, J. Song, G. Yu, A. Kretinin, F. Withers, Y. Cao, A. Mishchenko, I. Grigorieva, K. Novoselov, L. Levitov *et al.*, "Detecting topological currents in graphene superlattices," *Science*, vol. 346, no. 6208, pp. 448–451, 2014.

[170] D. Abanin, R. Gorbachev, K. Novoselov, A. Geim, and L. Levitov, "Giant spin-hall effect induced by the zeeman interaction in graphene," *Physical review letters*, vol. 107, no. 9, p. 096601, 2011.

[171] H. Min, G. Borghi, M. Polini, and A. H. MacDonald, "Pseudospin magnetism in graphene," *Physical Review B*, vol. 77, no. 4, p. 041407, 2008.

[172] B. Hunt, J. Sanchez-Yamagishi, A. Young, M. Yankowitz, B. J. LeRoy, K. Watanabe, T. Taniguchi, P. Moon, M. Koshino, P. Jarillo-Herrero *et al.*, "Massive dirac fermions and hofstadter butterfly in a van der waals heterostructure," *Science*, vol. 340, no. 6139, pp. 1427–1430, 2013.

[173] D. Xiao, W. Yao, and Q. Niu, "Valley-contrasting physics in graphene: magnetic moment and topological transport," *Physical Review Letters*, vol. 99, no. 23, p. 236809, 2007.

[174] A. Sakai and H. Kohno, "Spin torques and charge transport on the surface of topological insulator," *Physical Review B*, vol. 89, no. 16, p. 165307, 2014.

[175] Y. Fan, P. Upadhyaya, X. Kou, M. Lang, S. Takei, Z. Wang, J. Tang, L. He, L.-T. Chang, M. Montazeri *et al.*, "Magnetization switching through giant spin–orbit torque in a magnetically doped topological insulator heterostructure," *Nature materials*, vol. 13, no. 7, pp. 699–704, 2014.

[176] G. Giovannetti, P. A. Khomyakov, G. Brocks, P. J. Kelly, and J. van den Brink, "Substrate-induced band gap in graphene on hexagonal boron nitride: Ab initio density functional calculations," *Physical Review B*, vol. 76, no. 7, p. 073103, 2007.

[177] F. Ortmann, S. Roche, and S. O. Valenzuela, *Topological insulators: Fundamentals and perspectives*. John Wiley & Sons, 2015.

[178] Y. Chen, J. Analytis, J.-H. Chu, Z. Liu, S.-K. Mo, X.-L. Qi, H. Zhang, D. Lu, X. Dai, Z. Fang *et al.*, "Experimental realization of a three-dimensional topological insulator, bi2te3," *Science*, vol. 325, no. 5937, pp. 178–181, 2009.

[179] S.-Y. Xu, Y. Xia, L. Wray, S. Jia, F. Meier, J. Dil, J. Osterwalder, B. Slomski, A. Bansil, H. Lin *et al.*, "Topological phase transition and texture inversion in a tunable topological insulator," *Science*, vol. 332, no. 6029, pp. 560–564, 2011.

[180] T. Hirahara, N. Fukui, T. Shirasawa, M. Yamada, M. Aitani, H. Miyazaki, M. Matsunami, S. Kimura, T. Takahashi, S. Hasegawa *et al.*, "Atomic and electronic structure of ultrathin bi (111) films grown on bi 2 te 3 (111) substrates: evidence for a strain-induced topological phase transition," *Physical review letters*, vol. 109, no. 22, p. 227401, 2012.

[181] X. Xi, X.-G. He, F. Guan, Z. Liu, R. Zhong, J. Schneeloch, T. Liu, G. Gu, X. Du, Z. Chen *et al.*, "Bulk signatures of pressure-induced band inversion and topological phase transitions in pb 1- x sn x se," *Physical review letters*, vol. 113, no. 9, p. 096401, 2014.

[182] J. Kim, J. Kim, K.-S. Kim, and S.-H. Jhi, "Topological phase transition in the interaction of surface dirac fermions in heterostructures," *Physical review letters*, vol. 109, no. 14, p. 146601, 2012.

[183] M. Ezawa, "Valley-polarized metals and quantum anomalous hall effect in silicene," *Physical review letters*, vol. 109, no. 5, p. 055502, 2012.

[184] B. A. Bernevig, T. L. Hughes, and S.-C. Zhang, "Quantum spin hall effect and topological phase transition in hgte quantum wells," *Science*, vol. 314, no. 5806, pp. 1757–1761, 2006.

[185] X.-L. Qi, T. L. Hughes, and S.-C. Zhang, "Topological field theory of time-reversal invariant insulators," *Physical Review B*, vol. 78, no. 19, p. 195424, 2008.

[186] T. Yokoyama and Y. Tserkovnyak, "Spin diffusion and magnetoresistance in ferromagnet/topological-insulator junctions," *Physical Review B*, vol. 89, no. 3, p. 035408, 2014.

[187] M. H. Fischer, A. Vaezi, A. Manchon, and E.-A. Kim, "Spin-torque generation in topological insulator based heterostructures," *Physical Review B*, vol. 93, no. 12, p. 125303, 2016.

[188] Y. Wang, P. Deorani, K. Banerjee, N. Koirala, M. Brahlek, S. Oh, and H. Yang, "Topological surface states originated spin-orbit torques in bi 2 se 3," *Physical review letters*, vol. 114, no. 25, p. 257202, 2015.

[189] S. Maekawa, S. O. Valenzuela, E. Saitoh, and T. Kimura, *Spin Current*. OUP Oxford, 2012.

[190] F. Freimuth, S. Blügel, and Y. Mokrousov, "Direct and inverse spin-orbit torques," *Physical Review B*, vol. 92, no. 6, p. 064415, 2015.

[191] E. Saitoh, M. Ueda, H. Miyajima, and G. Tatara, "Conversion of spin current into charge current at room temperature: Inverse spin-hall effect," *Applied Physics Letters*, vol. 88, no. 18, p. 182509, 2006.

[192] Z. Tang, E. Shikoh, H. Ago, K. Kawahara, Y. Ando, T. Shinjo, and M. Shiraishi, "Dynamically generated pure spin current in single-layer graphene," *Physical Review B*, vol. 87, no. 14, p. 140401, 2013.

[193] J.-C. Rojas-Sánchez, S. Oyarzún, Y. Fu, A. Marty, C. Vergnaud, S. Gambarelli, L. Vila, M. Jamet, Y. Ohtsubo, A. Taleb-Ibrahimi *et al.*, "Spin to charge conversion at room temperature by spin pumping into a new type of topological insulator: α-sn films," *Physical Review Letters*, vol. 116, no. 9, p. 096602, 2016.

[194] Y. Shiomi, K. Nomura, Y. Kajiwara, K. Eto, M. Novak, K. Segawa, Y. Ando, and E. Saitoh, "Spin-electricity conversion induced by spin injection into topological insulators," *Physical review letters*, vol. 113, no. 19, p. 196601, 2014.

[195] M. Jamali, J. S. Lee, J. S. Jeong, F. Mahfouzi, Y. Lv, Z. Zhao, B. K. Nikolic, K. A. Mkhoyan, N. Samarth, and J.-P. Wang, "Giant spin pumping and inverse spin hall effect in the presence of surface and bulk spin- orbit coupling of topological insulator bi2se3," *Nano Letters*, vol. 15, no. 10, pp. 7126–7132, 2015.

[196] L. Onsager, "Reciprocal relations in irreversible processes. i." *Physical Review*, vol. 37, no. 4, p. 405, 1931.

[197] H. Jiao and G. E. Bauer, "Spin backflow and ac voltage generation by spin pumping and the inverse spin hall effect," *Physical review letters*, vol. 110, no. 21, p. 217602, 2013.

[198] M. Naguib, M. Kurtoglu, V. Presser, J. Lu, J. Niu, M. Heon, L. Hultman, Y. Gogotsi, and M. W. Barsoum, "Two-dimensional nanocrystals produced by exfoliation of ti3alc2," *Advanced Materials*, vol. 23, no. 37, pp. 4248–4253, 2011.

[199] M. Naguib, V. N. Mochalin, M. W. Barsoum, and Y. Gogotsi, "25th anniversary article: Mxenes: A new family of two-dimensional materials," *Advanced Materials*, vol. 26, no. 7, pp. 992–1005, 2014.

[200] L. Li, Y. Yu, G. J. Ye, Q. Ge, X. Ou, H. Wu, D. Feng, X. H. Chen, and Y. Zhang, "Black phosphorus field-effect transistors," *Nature nanotechnology*, vol. 9, no. 5, pp. 372–377, 2014.

[201] B. Radisavljevic, A. Radenovic, J. Brivio, V. Giacometti, and A. Kis, "Single-layer mos2 transistors," *Nature nanotechnology*, vol. 6, no. 3, pp. 147–150, 2011.

[202] G. Fiori, F. Bonaccorso, G. Iannaccone, T. Palacios, D. Neumaier, A. Seabaugh, S. K. Banerjee, and L. Colombo, "Electronics based on two-dimensional materials," *Nature nanotechnology*, vol. 9, no. 10, pp. 768–779, 2014.

[203] C. Cheng, J.-C. R. Sánchez, M. Collet, V. Ivanovskaya, B. Dlubak, P. Seneor, A. Fert, H. Kim, G. H. Han, Y. H. Lee *et al.*, "Direct observation of spin-to-charge conversion in mos2 monolayer with spin pumping," *arXiv preprint arXiv:1510.03451*, 2015.

[204] Z. Zhu, Y. Cheng, and U. Schwingenschlögl, "Giant spin-orbit-induced spin splitting in two-dimensional transition-metal dichalcogenide semiconductors," *Physical Review B*, vol. 84, no. 15, p. 153402, 2011.

[205] K. F. Mak, K. He, J. Shan, and T. F. Heinz, "Control of valley polarization in monolayer mos2 by optical helicity," *Nature nanotechnology*, vol. 7, no. 8, pp. 494–498, 2012.

[206] A. V. Stier, K. M. McCreary, B. T. Jonker, J. Kono, and S. A. Crooker, "Magneto-reflection spectroscopy of monolayer transition-metal dichalcogenide semiconductors in pulsed magnetic fields," *arXiv preprint arXiv:1603.07004*, 2016.

[207] G. Mahan, "Many body physics," *Reviewed in Plenum, New York*, 1981.

8 Papers Submitted and Under Preparation

• Hang Li, Xuhui Wang, Fatih Doğan and Aurélien Manchon, "Tailoring spin-orbit torque in diluted magnetic semiconductors", *Applied Physics Letters*, **1**02, 192411 (2013).

• Hang Li, H. Gao, Liviu P. Zârbo, K. Výborný, Xuhui Wang, Ion Garate, Fatih Doğan, Antonín Čejchan, Jairo Sinova, T. Jungwirth, and Aurélien Manchon, "Intraband and interband spin-orbit torques in noncentrosymmetric ferromagnets", *Physical Review B*, **9**1, 134402 (2015).

• Hang Li, Xuhui Wang and Aurélien Manchon, "Valley-dependent spin-orbit torques in two dimensional hexagonal crystals", *Physical Review B*, **9**3, 035417 (2016)

• Hang Li and Aurélien Manchon, "Tunable spin-charge conversion through topological phase transitions in zigzag nanoribbons", *arXiv:1604.08782*(Submitted to Physical Review B, in minor revision).

• Hang Li and Aurélien Manchon, "Theoretical model of spin torque in Permalloy on monolayered MoS_2", *In preparation.*